MAGNETIC NEUTRAL POINTS AND NONUNIFORM RECONNECTION

N. R. Strachan

A Thesis Submitted for the Degree of PhD
at the
University of St Andrews

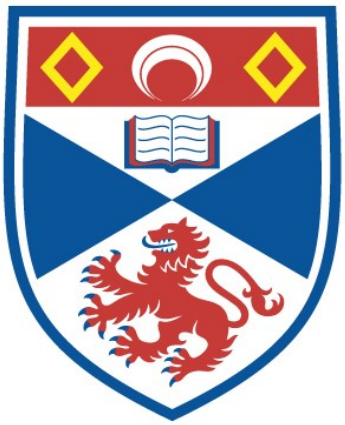

1994

MAGNETIC NEUTRAL POINTS AND NONUNIFORM RECONNECTION

N R STRACHAN

Submitted for the Degree of Doctor of Philosophy at the University of St. Andrews.

ProQuest LLC.
789 East Eisenhower Parkway
P.O. Box 1346
Ann Arbor, MI 48106 – 1346

COPYRIGHT

POSTGRADUATE CAREER

I was admitted to the Faculty of Science of the University of St. Andrews under Ordinance General No. 12 on 1/10/89 and as a candidate for the degree of Ph.D. on 1/10/90.

Signed .....

Date 5.5.93

DECLARATION

I, Neil Robert Strachan, hereby certify that this thesis has been composed by myself, that it is a record of my own work and that it has not been accepted in partial or complete fulfilment of any other degree or professional qualification.

Signe

Date 5.5.93

CERTIFICATE

I hereby certify that the candidate has fulfilled the conditions of the Resolution and Regulations appropriate to the Degree of Ph.D.

Signed .... Date 5.5.93

Contents

Abstract

Ever since the first recorded observation of a solar flare in September 1859, it has been a key question — for physics as a whole and for astrophsics in particular — to ask what mechanism lies behind the sudden, violent release of energy from the sun. It has become increasingly apparent that the complex structure of the solar magnetic field lies at the heart of the answer. The process of magnetic reconnection has, over the years, become the accepted explanation by which magnetic energy can be released on both large and small scales in astrophysical and laboratory plasmas. The results of reconnection can be seen, for instance, in star formation, solar flares and the earth's aurorae; indeed the 1859 flare was followed by exceptional auroral activity.

The mechanism of magnetic reconnection was first postulated by Giovanelli (1947) as a way of releasing the magnetic energy stored in the Sun. He, and later Dungey (1953), realised that the behaviour of the plasma in the vicinity of a magnetic neutral or null point, where the field disappears, is quite different from other regions of space. In this thesis the nature of magnetic neutral points and their rôle in the process of reconnection is investigated.

Firstly, a general classification of magnetic neutral points is presented. The chapter includes equilibrium and steady-state solutions for two-dimensional magnetic neutral points. The differences in the field behaviour close to each type of neutral point are explained and criteria for the existence of steady-state solutions and equilibria involving pressure balance are presented. In the last section, a self-similar solution for a collapsed X-point is explored. The X-point necessarily becomes cusp-like in nature if shearing is applied in the ignorable direction.

Two reconnection models are considered. The first is an extension of the Priest-Lee model (1990). It incorporates large pressure gradients in the inflow corresponding to the Forbes-Priest *Almost-Uniform Model*. The investigation includes both analytical and numerical solutions and a study of the separatrix jet. In the numerical study, current spikes are found at the end of the current sheets and a much increased reconnection rate is found analytically in the extreme flux file-up limit.

The second reconnection model presented is also based on the Priest-Lee configuration. A uniform field is imposed on the basic structure producing a cusp-point with a non-zero field strength as the neutral point is approached from above. This results in the removal of the singularity in the flow above the separatrix. A non-singular solution is found analytically for a double-cusp. A much larger reconnection rate is found and a numerical solution is presented.

Acknowledgements

The people who have helped me during my time as a postgraduate are too numerous to mention here. I am grateful to the Solar Theory Group in St. Andrews, both past and present. However, I would like to thank certain people without whom I could not have done this work. Firstly to Eric Priest, my supervisor, whose diligence and guidance throughout my postgraduate career have been invaluable, and whose encouragement in the last few months of my thesis work has been essential. To all those who helped with the considerable amount of computational work involved, most notably Craig Anderson. To those visitors with whom I have had the pleasure of collaborating. To the SERC for the finance which made this project possible. To my parents for unstinting financial and moral support.

Finally, I would like to thank Judith for her care and love. At the start of our life together, I dedicate this thesis to her.

Chapter 1

Introduction

1.1 Basic Equations

In studying the solar atmosphere and its associated magnetic field, assumptions about the behaviour of the plasma must be made in order for a sensible mathematical model to be constructed. By looking at effects happening on scales larger than the mean free paths of the particles in the Sun's atmosphere, we may assume that the plasma is a continuous fluid. The general set of equations describing phenomena on this scale is the set of magnetohydrodynamical equations (hereafter abbreviated to MHD). The set comprises Maxwell's equations of (slow) electromagnetism coupled with Ohm's Law for an electrically neutral plasma and the equations of hydrodynamical motion (including the magnetic force, continuity and energy).

1.1.1 Maxwell's Equations and Ohm's Law

Maxwell's equations are

$$\nabla \times \mathbf{B} = \mu \mathbf{j} + \frac{1}{c^2}\frac{\partial \mathbf{E}}{\partial t}, \tag{1.1}$$

$$\nabla \cdot \mathbf{B} = 0, \tag{1.2}$$

$$\nabla \times \mathbf{E} = -\frac{\partial \mathbf{B}}{\partial t} \tag{1.3}$$

and

$$\nabla \cdot \mathbf{E} = \frac{\rho_c}{\epsilon}, \tag{1.4}$$

where $\mathbf{B}$ is the magnetic induction (usually called the magnetic field), $\mathbf{E}$ is the electric field and $\mathbf{j}$ is the current density. The quantities μ, ϵ, c and ρ_c are the magnetic permeability, the permittivity,

the speed of light in a vacuum and the electric charge density, respectively. The values for μ and ϵ are usually approximated by their values in a vacuum, μ_o and ϵ_o, with $c = (\mu_o \epsilon_o)^{-1/2}$.

For processes where the velocity is typically less than $0.1c$ we may disregard the second term on the right-hand side of (1.1), which becomes negligible by comparison with (1.3). This is certainly true for many phenomena in the solar atmosphere, so (1.1) becomes

$$\nabla \times \mathbf{B} = \mu \mathbf{j}. \tag{1.5}$$

To this set of equations we may add Ohm's Law for a neutral plasma which states that the current density is proportional to the total electric field. A charged particle moving with velocity $\mathbf{v}$ in a magnetic field $\mathbf{B}$ experiences a total electric field $\mathbf{E} + \mathbf{v} \times \mathbf{B}$. Hence Ohm's Law becomes

$$\mathbf{j} = \sigma(\mathbf{E} + \mathbf{v} \times \mathbf{B}), \tag{1.6}$$

where σ is the electrical conductivity. Substituting $\mathbf{E}$ from (1.6) into (1.3) and using constraint (1.2) we find

$$\frac{\partial \mathbf{B}}{\partial t} = \nabla \times (\mathbf{v} \times \mathbf{B}) + \eta \nabla^2 \mathbf{B}, \tag{1.7}$$

where $\eta = 1/(\mu\sigma)$ is the magnetic diffusivity and is presumed to be uniform. Equation (1.7) is known as the diffusion equation and will fully describe the magnetic field for any given velocity profile, $\mathbf{v}$. Comparing terms on the right-hand side of (1.7) will tell us which term will dominate in different circumstances. The ratio of the terms is lv/η, where l and v are a typical length scale and speed. This ratio is called the magnetic Reynolds number (R_m) and is very important in the study of reconnection, as we shall see later.

A typical global coronal value of R_m is about $10^6 - 10^{12}$, so for most of the solar atmosphere (1.7) becomes

$$\frac{\partial \mathbf{B}}{\partial t} = \nabla \times (\mathbf{v} \times \mathbf{B}), \tag{1.8}$$

The limit of $R_m \gg 1$ is known as the perfectly conducting limit, though this does not mean that there is no current, rather that the diffusive term in (1.7) is negligible. MHD governed by this equation (and neglecting dissipation in the equation of motion) is often called "ideal" MHD. There is a very important consequence in this limit:

Consider a closed circuit, C, bounding a surface, S, which is moving with the plasma, so that the flux, F, through S is given by

$$F = \int_S \int \mathbf{B} \cdot \mathbf{dS}. \tag{1.9}$$

The rate of change of flux through C as it moves is given by

$$\frac{DF}{Dt} = \int_S \int \frac{\partial \mathbf{B}}{\partial t} \cdot \mathbf{dS} - \oint_C (\mathbf{v} \times \mathbf{B}) \cdot \mathbf{ds}, \tag{1.10}$$

where ds is an element of circuit C and the operator $D/Dt = \mathbf{v} \cdot \nabla + \partial/\partial t$ produces the convective derivative. After invoking Stokes' theorem, the contour integral can be written as a surface integral and the two integrals in (1.10) combined to give a single integral, namely

$$\frac{DF}{Dt} = \int_S \int \left(\frac{\partial \mathbf{B}}{\partial t} - \nabla \times (\mathbf{v} \times \mathbf{B}) \right) \cdot \mathbf{dS}, \tag{1.11}$$

which is identically zero when (1.8) holds. Physically, this implies that the flux associated with a moving element of plasma remains "frozen" to it. Because the approximation is valid for most solar MHD situations this is an important result. In the solar corona, magnetic forces dominate so plasma is pulled along with the field, whereas in the photosphere, for instance, the inertia of the plasma dominates and the field is dragged by the plasma. Plasma may still move *along* field lines, but once plasma is on a particular field line it must stay on that field line.

Magnetic field lines form distinct topological regions which are separated by limiting field lines or flux surfaces. In two dimensions, the limiting lines are called separatrices, and in three dimensions the surfaces are known as separatrix surfaces. In two-dimensions the intersection of two or more separatrices is a magnetic neutral point. The only way in which plasma may cross separatrices is for "ideal" MHD to be violated by the field lines breaking and reconnecting — in other words diffusing through the plasma — hence the term magnetic reconnection. It is only in the vicinity of magnetic neutral points that length scales exist which are short enough for diffusion to be important in (1.7) and for reconnection to take place.

1.1.2 Plasma Equations

To complete the description of MHD, hydrodynamical equations are required. The normal momentum equation in a system with a pressure gradient, gravitational force and Lorentz force is

$$\rho \frac{D\mathbf{v}}{Dt} = -\nabla p + \mathbf{j} \times \mathbf{B} + \rho \mathbf{g}, \tag{1.12}$$

with D/Dt as above. We also require the continuity equation,

$$\frac{D\rho}{Dt} = -\rho(\nabla \cdot \mathbf{v}); \tag{1.13}$$

the ideal gas law,

$$p = \frac{R}{\mu_a} \rho T \tag{1.14}$$

and an energy equation,

$$\frac{\rho^\gamma}{\gamma - 1} \frac{D}{Dt} \left(\frac{p}{\rho^\gamma} \right) = -\nabla \cdot \mathbf{q} - L_r + \frac{j^2}{\sigma}. \tag{1.15}$$

In (1.12)–(1.14), $\mathbf{g} = -g\hat{\mathbf{z}}$ is the acceleration due to gravity, R is the gas constant, T is the absolute temperature and μ_a is mean atomic weight ($\mu_a = 0.5$ corresponds to an atmosphere consisting solely of ionised hydrogen). In the energy equation, γ is the ratio of the specific heat at constant pressure (c_p) to the specific heat at constant volume (c_v), $\mathbf{q}$ is the heat flux due to particle conduction, L_r is the radiative loss and j^2/σ is ohmic dissipation. The sound speed, $c_s^2 = \gamma p/\rho$, is derived from these equations for an ideal gas.

The physical description of phenomena in the solar atmosphere can be built up from equations (1.2)–(1.15). However, in order to study steady-state reconnection and solutions around magnetic neutral points — the aim here — further approximations and restrictions have to be made.

1.2 Steady-State Reconnection MHD Approximations

In the reconnection models studied here two major assumptions are made. First, that the models are purely two-dimensional and second that the magnetic field is in a steady state. The second of these means that the field does not evolve in a time-dependent manner over many typical time-steps associated with the system, usually the Alfvénic time, τ_A. Consequently

$$\frac{\partial \mathbf{B}}{\partial t} = 0, \tag{1.16}$$

which in turn implies that the electric field, $\mathbf{E}$, is uniform, by (1.3), so Ohm's Law in the perfectly conducting limit becomes

$$\mathbf{v} \times \mathbf{B} = -\mathbf{E} = constant. \tag{1.17}$$

Hence, for a prescribed steady-state magnetic field, a corresponding flow can be established which is also in a steady state. (In the particular case $E \equiv 0$, the flow becomes everywhere aligned with the field.) Consequently (1.12) reduces to

$$\rho(\mathbf{v} \cdot \nabla)\mathbf{v} = -\nabla p + \mathbf{j} \times \mathbf{B}. \tag{1.18}$$

Gravity is neglected because it is small compared with the pressure gradient if the scale-lengths involved are much less than the pressure scale height, $H = RT/\mu_a g$, which is the case here.

Another important assumption is that of incompressibility, in other words the plasma density, ρ, is uniform and (1.13) reduces to

$$\nabla \cdot \mathbf{v} = 0. \tag{1.19}$$

This approximation is valid whenever the macro properties are such that $v \ll c_s \ll v_A$, which is usually the case in the solar atmosphere. It is also valid when there is a very large plasma pressure present. Together, incompressibility and the steady state assumption mean that the system can

be fully described, so that with the energy equation determines the temperature in an independent way.

The flow can now be recast by writing $\mathbf{v} = curl\, \Psi$, so that (1.19) is satisfied identically. For a two-dimensional flow, we simply have $\Psi = \Psi(x, y)\hat{\mathbf{z}}$ yielding

$$v_x = \frac{\partial \Psi}{\partial y}, \quad v_y = -\frac{\partial \Psi}{\partial x}. \tag{1.20}$$

If we assume that the fluid term in (1.18) is much smaller than the magnetic term, in other words $v \ll v_A$, we have

$$\mathbf{j} \times \mathbf{B} = \nabla p. \tag{1.21}$$

By using (1.5) and (1.2), the Lorentz force may be split into two terms, namely

$$\frac{1}{\mu}(\nabla \times \mathbf{B}) \times \mathbf{B} = \frac{1}{\mu}(\mathbf{B} \cdot \nabla)\mathbf{B} - \nabla\left(\frac{B^2}{2\mu}\right). \tag{1.22}$$

The first term represents a magnetic tension and the second term is a magnetic pressure gradient. We may now introduce an important ratio, that of the plasma pressure to the magnetic pressure, called the plasma β, where

$$\beta = \frac{2\mu p}{B^2}. \tag{1.23}$$

A typical coronal value of β is 0.01, reducing (1.21) still further to

$$\mathbf{j} \times \mathbf{B} = 0. \tag{1.24}$$

This approximation is used for many reconnection models. In two dimensions the only solution is $\mathbf{j}$=$\mathbf{0}$. We can rewrite $\mathbf{B}$ as

$$\mathbf{B} = \nabla \times \mathbf{A}, \tag{1.25}$$

where $\mathbf{A} = A(x, y)\hat{\mathbf{z}}$ is the flux function, so (1.2) is satisfied identically, whilst (1.5) becomes

$$\nabla^2 A = 0. \tag{1.26}$$

Consequently, many reconnection problems involve solving for a current-free or potential field, which is simply a matter of solving Laplace's equation subject to relevant boundary conditions. Some models, however, do not assume that the plasma β is small and so (1.21) applies. The importance of including significant pressure gradients is explored in Chapter 3.

1.3 Reconnection Models

The idea of the breakdown of ideal MHD allowing localised diffusion near a neutral point was first put forward by Dungey (1953). Thereafter, Sweet (1957) and Parker (1958) independently came up

with a steady annihilation model where advection of flux from two sides is balanced by diffusion in a thin sheet. In their model they consider a diffusion region of width ℓ and length L. There is a uniform flow, v_i, bringing a uniform field, B_i, towards the diffusion region. At the sheet, the inflow of magnetic flux is balanced by diffusion, so

$$v_i = \frac{\eta}{\ell}, \tag{1.27}$$

where η is the (uniform) diffusivity. Also, by assuming uniform plasma density, continuity of mass into and out of the diffusion region yields

$$v_i L = v_o \ell, \tag{1.28}$$

where v_o is the speed of the plasma coming out of the current sheet. By a simple pressure balance and Bernoulli law in the diffusion region, we see that $\rho v_o^2/2 = B_i^2/2\mu$ showing us that the diffusion region outflow speed is given by

$$v_o = v_{Ai}, \tag{1.29}$$

where $v_{Ai} = B_i/(\mu\rho)^{1/2}$ is the Alfvén speed. Eliminating ℓ between (1.27) and (1.28), the reconnection rate, $M_i = v_i/v_{Ai}$ is given by

$$M_i = R_{mi}^{-\frac{1}{2}}, \tag{1.30}$$

where $R_{mi} = Lv_{Ai}/\eta$ is the Lundquist number. (This is often referred to as the magnetic Reynolds number, but is distinct from the ratio of terms in the induction equation (1.7).) If L is of the same order as some external distance, L_e, this rate is very small and cannot explain the high rate of reconnection in a solar flare, for instance.

Petschek (1964) overcame this difficulty by proposing a mechanism with a small Sweet-Parker region in a converging flow which has two pairs of standing slow-mode shocks propagating from each end. Because the region is very small compared with the overall length-scales of the system, the inflow Lundquist number, R_{mi}, is very small. In fact Petschek found an external reconnection rate, $M_e = v_e/v_{Ae}$, only weakly dependent on the external Lundquist number, $R_{me} = L_e v_{Ae}/\eta$, namely

$$M_e = \frac{\pi}{8 \log R_{me}}. \tag{1.31}$$

This rate is much higher than the Sweet-Parker rate for the same Lundquist number ($\gg 1$) and is referred to as a fast reconnection rate.

Subsequently, steady-state models have usually incorporated shocks coming off a central diffusion region. Sonnerup (1970) finds a fast rate by having an extra pair of shocks coming off each end of the diffusion region, but Vasyliunas (1975) demonstrated that this is unphysical. Priest and Forbes (1986) have generalised the Petschek analysis by including pressure gradients in their inflow

region. In their model they have expansive and compressive regimes and both fast- and slow-mode reconnection. The classification of steady reconnection is due to Vasyliunas and states that if the magnetic field strength and plasma pressure are both increasing or decreasing as the diffusion region is approached then the reconnection is fast-mode, but if one is increasing and the other decreasing then the reconnection is slow-mode.

All the above models involve the analysis of perturbations about uniform fields. However this need not always be the case. Often, the effects of reconnection near a potential X-point have been considered and numerical simulations (e.g. Biskamp, 1986; Lee and Fu, 1986; Scholer, 1989; Forbes, 1990) have also been used to explore reconnection and find new features, such as nonuniform fields, as well as different reconnection rates. Some studies (e.g. Scholer, 1989) find Petschek-like reconnection by considering the effect of spatially varying resistivity, however this avenue will not be explored here. It is clear that the type and rate of steady reconnection that one finds in all these models is highly dependent on the boundary conditions imposed. The latest models incorporate nonuniform field analysis and numerical simulations (e.g. Priest and Lee, 1990) and consider the effects of different boundary conditions. The analysis in this thesis seeks to extend the understanding of the way in which different boundary conditions affect magnetic reconnection. Also, the changes brought about by considering different types of neutral point in the reconnection model are examined.

Chapter 2

Two-Dimensional Magnetic Neutral Points and a Self-Similar Model for a Cusp-Point

2.1 Chapter Summary

Many different two-dimensional magnetic neutral points have been investigated over the years, but a general classification has not previously been presented. In this chapter, we seek to classify and categorise such neutral points. Section 1 presents the four main types of neutral point and explores conditions around magnetic neutral points which might lead to magnetic equilibria or steady states. In Section 2 the potential X-point is generalised, producing non-potential X-points and symmetric star-points. The generalisation of the potential Y-point is examined in Section 3, with non-potential models and asymmetric star-points described. Section 4 classifies T-points and cusp-points, highlighting the difference in field behaviour in their vicinity. A three-dimensional equilibrium cusp-point model caused by an X-point collapse is studied in Section 5, following on from the work presented by Vekstein and Priest (1991). Section 6 contains the conclusions.

2.2 Introduction

In a two-dimensional magnetic configuration, hyperbolic neutral points, where the magnetic field vanishes and the neighbouring field lines are not closed or spiral, are of special significance since they represent locations where the magnetic field lines may be broken and reconnected [Dungey, 1953;

Sweet, 1958; Parker, 1957; Furth *et al.* , 1963; Vasyliunas, 1975; Sonnerup, 1979; Priest, 1985; Priest and Forbes, 1986]. Recently attention has begun to focus on three-dimensional neutral or null points as possible sites for reconnection (e.g. Lau and Finn, 1990; Priest and Forbes, 1991) but here we shall limit ourselves to the two-dimensional problem. The effects of reconnection are felt far beyond the immediate neighbourhood of the neutral point and include: changes in magnetic topology and pathways for propagation of fast particles, heat and plasma; conversion of magnetic energy into heat and bulk kinetic energy; the creation of shock waves, filamentary currents, turbulence and strong electric fields which may accelerate fast particles. Strangely, however, a comprehensive account of the possible structure of two-dimensional neutral points has not yet been given. Attention has focussed on the simple X-type neutral point with a potential or current-free field

$$B_x = y, \quad B_y = x. \tag{2.1}$$

The field lines are rectangular hyperbolae given by

$$A = \frac{1}{2}(y^2 - x^2), \tag{2.2}$$

where A is the flux function, related to the magnetic field by

$$B_x = \frac{\partial A}{\partial y}, \quad B_y = -\frac{\partial A}{\partial x}. \tag{2.3}$$

In general the magnetic field is related to the flux function by

$$\mathbf{B} = \nabla \times \mathbf{A},$$

where $\mathbf{A} = A(x, y)\hat{\mathbf{z}}$, and so we recover (2.3).

Y-points, T-points and cusp-points have also been referred to in passing in studies of reconnection of partially open magnetic fields to produce two-ribbon solar flares (Pneuman and Kopp, 1970), although solutions for their structure have not been presented (Figure 2.1). Extending previous ideas of Sturrock and Smith (1968), Pneuman and Kopp (1970) suggested that the physical difference between these points is as follows. For a Y-point, the magnetic field tends to zero from all three principal directions as one approaches it. For a cusp-point, the field tends to zero from only one direction, and for a T-point the field tends to zero from only two directions. In fact, these definitions need some clarification, as we will see later.

The most fundamental constraint on the magnetic field structure is

$$\nabla \cdot \mathbf{B} = 0, \tag{2.4}$$

so that there can be no monopoles contained inside a space and flux is conserved along a flux tube. We shall simply aim here to find flux functions, A, for which $\partial A/\partial y$ and $\partial A/\partial x$ approach zero from at least one direction as we approach a neutral point at the origin.

Near each neutral point it is of interest to determine the distribution of the electric current

$$\mathbf{j} = \frac{1}{\mu}\nabla \times \mathbf{B}, \tag{2.5}$$

which, for our two-dimensional configurations, has only a z-component and may be written

$$j = -\frac{1}{\mu}\nabla^2 A = -\frac{1}{\mu}\left[\frac{\partial^2 A}{\partial y^2} + \frac{\partial^2 A}{\partial x^2}\right]. \tag{2.6}$$

Some neutral point structures are in equilibrium under a balance between a magnetic field and a pressure gradient.

$$\mathbf{j} \times \mathbf{B} = \nabla \mathrm{p}. \tag{2.7}$$

and so the condition that it is possible to find an appropriate pressure distribution is

$$\nabla \times (\mathbf{j} \times \mathbf{B}) = \mathbf{0}. \tag{2.8}$$

For our two-dimensional field (2.8) becomes

$$\frac{\partial}{\partial x}\left[\nabla^2 A \frac{\partial A}{\partial y}\right] - \frac{\partial}{\partial y}\left[\nabla^2 A \frac{\partial A}{\partial x}\right] = 0, \quad \text{or} \quad \left[\frac{\partial A}{\partial y}\frac{\partial}{\partial x} - \frac{\partial A}{\partial x}\frac{\partial}{\partial y}\right]\nabla^2 A = 0. \tag{2.9}$$

Equation (2.9) implies that $\nabla^2 A = f(A)$ or we can recognise it as $(\mathbf{B}\cdot\nabla)\mathrm{j} = 0$, so that the current is constant along the field lines. In general the resulting pressure, from (2.7), is

$$p(A) = \int j(A)\, dA. \tag{2.10}$$

More generally, for a force balance between magnetic, plasma pressure and gravitational forces

$$\mathbf{j} \times \mathbf{B} = \nabla \mathrm{p} - \rho \mathbf{g}. \tag{2.11}$$

For example, in an isothermal plasma with $p = R\rho T$ and a uniform gravitational acceleration $\mathbf{g} = -g\hat{\mathbf{y}}$ this may be recast as

$$\mathbf{j} \times \mathbf{B} \;=\; \nabla p - \frac{pg}{RT}\hat{\mathbf{y}} \;=\; e^{-y/H}\nabla(pe^{y/H}),$$

where $H = RT/g$ is the pressure scale height. Thus the condition for being able to find an equilibrium pressure distribution becomes

$$\nabla \times \left[e^{y/H}(\mathbf{j} \times \mathbf{B})\right] = 0.$$

or for a two-dimensional field $\mathbf{B}(x, y)$

$$\mathbf{B} \cdot \nabla(\mathrm{j}e^{y/H}) = \mathbf{0}$$

Some current sheets are reconnecting, in which case for a kinematic treatment of the surrounding ideal region one needs to solve

$$\mathbf{E} + \mathbf{v} \times \mathbf{B} = 0, \tag{2.12}$$

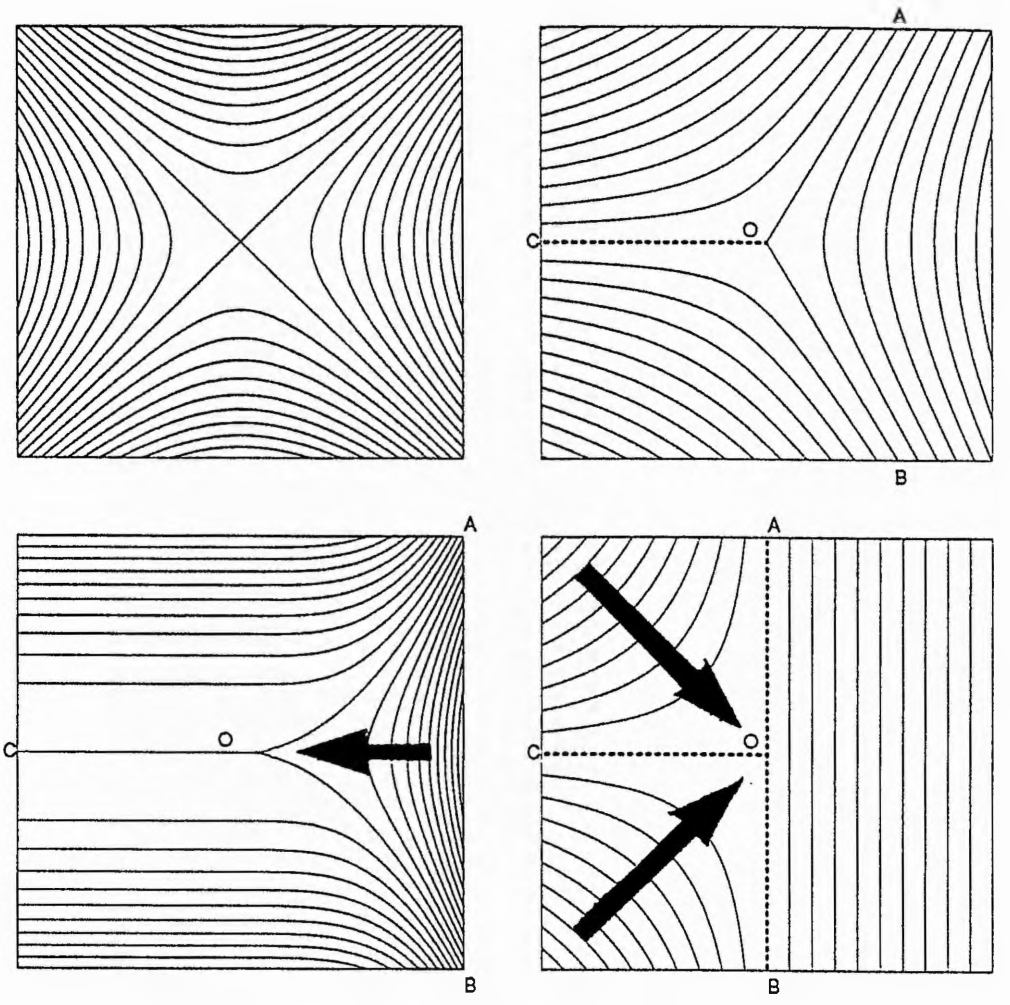

Figure 2.1: Magnetic field lines for the simple neutral points: (a) X-point, (b) Y-point, (c) cusp-point and (d) T-point. Heavy arrows indicate directions along which the field approaches zero most quickly for the cusp- and T-points.

In the particular case of steady reconnection the equation $\nabla \times \mathbf{E} = 0$ implies for our two-dimensional configuration that $\mathbf{E} = E\hat{\mathbf{z}}$ is constant, and so (2.12) determines the flow speed $v_\perp$ normal to the magnetic field to be

$$v_\perp = -\frac{E}{B}.$$

The flow $v_\parallel$ parallel to the field can be determined by other considerations, such as, for instance, the continuity equation for an incompressible medium

$$\nabla \cdot \mathbf{v} = 0, \tag{2.13}$$

together with boundary conditions on $v_\parallel$.

If a configuration is *not* in a magnetostatic equilibrium satisfying (2.9), but is in a steady state,

then the inertial term needs to be added to (2.7) to give

$$\mathbf{j} \times \mathbf{B} = \rho(\mathbf{v} \cdot \nabla)\mathbf{v} + \nabla \mathrm{p}. \tag{2.14}$$

Under condition (2.13) this leads, after taking the curl of (2.14), to

$$\left[\frac{\partial A}{\partial y}\frac{\partial}{\partial x} - \frac{\partial A}{\partial x}\frac{\partial}{\partial y}\right]\nabla^2 A = \mu\rho\left[\frac{\partial \Psi}{\partial y}\frac{\partial}{\partial x} - \frac{\partial \Psi}{\partial x}\frac{\partial}{\partial y}\right]\nabla^2 \Psi,$$

or (2.15)

$$\left[\frac{1}{r}\frac{\partial A}{\partial \theta}\frac{\partial}{\partial r} - \frac{\partial A}{\partial r}\frac{\partial}{\partial \theta}\right]\nabla^2 A = \mu\rho\left[\frac{1}{r}\frac{\partial \Psi}{\partial \theta}\frac{\partial}{\partial r} - \frac{\partial \Psi}{\partial r}\frac{\partial}{\partial \theta}\right]\nabla^2 \Psi,$$

in cylindrical polar coordinates. Here A is the flux function and Ψ is the stream function, related to the flow by

$$v_x = \frac{\partial \Psi}{\partial y}, \; v_y = -\frac{\partial \Psi}{\partial x}, \tag{2.16}$$

so that (2.13) is automatically satisfied. However, these solutions also need to satisfy (2.12) for ideal MHD, which further restricts solutions to (2.15).

For a more difficult fully dynamical analysis one needs to solved the coupled, time dependent MHD equations of induction, motion, continuity and energy, which invariably demand a numerical approach, even when simplifying assumptions such as isothermality are adopted.

2.3 X-Points and Symmetric Star-Points

2.3.1 Generalisations of Potential X-Point

The *potential X-point* (2.2) has a vanishing current and so is in equilibrium in a uniform-pressure plasma. In this section we seek to generalise it systematically in several ways. Its simplest generalisation is given by the flux function

$$A = \frac{1}{2}(y^2 - c^2 x^2), \tag{2.17}$$

and the field components are

$$B_x = y, \quad B_y = c^2 x.$$

The separatrices $y = \pm cx$ are now inclined to the x-axis at an angle smaller ($c < 1$) or larger ($c > 1$) than $\pi/4$. From (2.6), the electric current is

$$j = \frac{1}{\mu}(c^2 - 1),$$

which is uniform and correspondingly positive or negative. Equation (2.17) satisfies (2.9) so an equilibrium exists with a pressure given by (2.10) which is

$$p = jA.$$

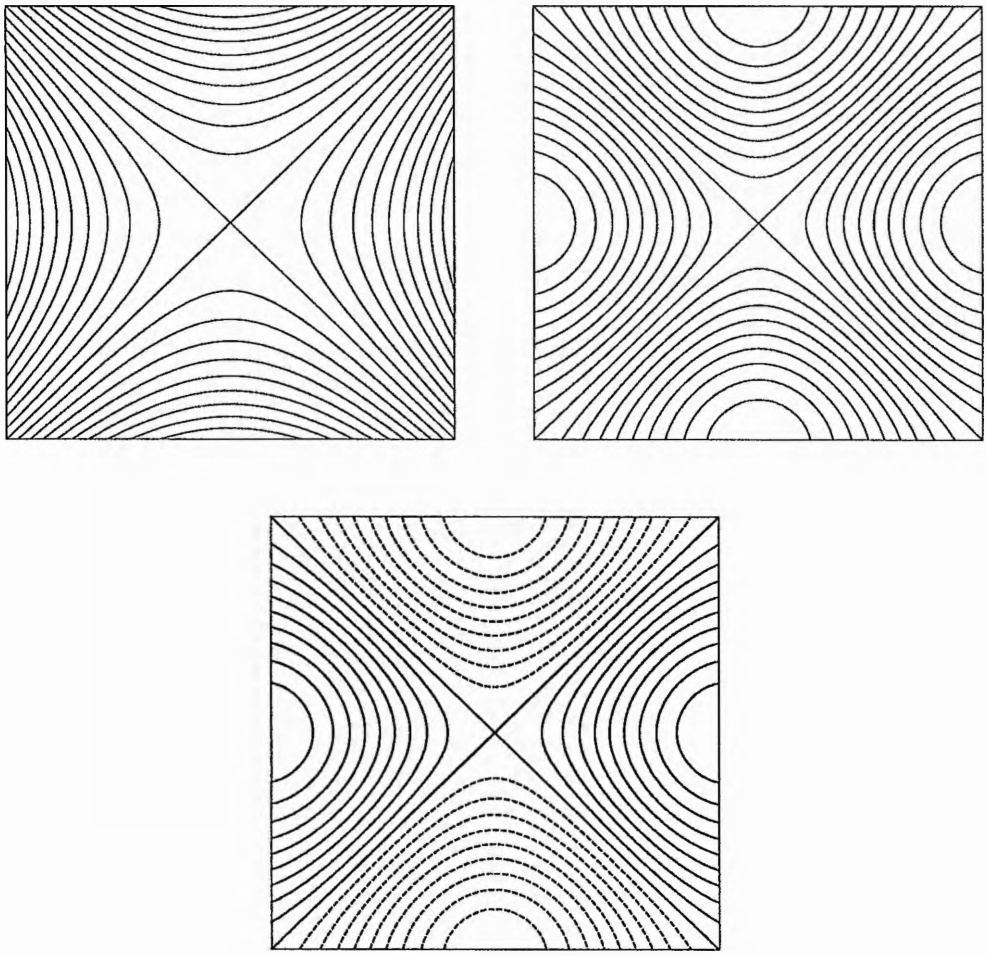

Figure 2.2: (a) The field lines of X-points with flux function $A = r^2 \cos 2\theta$ and $A = J_2(\alpha r) \cos 2\theta$ and (b) the current density contours of the Bessel function solution. Negative current is indicated by dashed curves.

A self-similar collapse of such a neutral point with uniform plasma pressure and c increasing in time on an Alfvénic time-scale has been studied by Imshennik and Syrovatsky (1967), Chapman and Kendall (1963) and Forbes and Speiser (1979). However an equilibrium is possible with a pressure gradient, which suggests that, although potential X-points tend to collapse or split to form a current sheet, in the presence of pressure gradients such a collapse or splitting may not necessarily occur.

In order to generalise this *uniform-current X-point* further it is helpful to write (2.17) in polar coordinates as

$$A = \frac{1}{2} r^2 \left[(1 - c^2) - (1 + c^2) \cos 2\theta \right] ,$$

or, after absorbing $\frac{1}{2}(1+c^2)$ in A and replacing $(1-c^2)/(1+c^2)$ by K,

$$A = r^2\left[K - \cos 2\theta\right], \quad -1 \leq K \leq 1. \tag{2.18}$$

This is one generalisation of the potential field given by the flux function $A = r^2\cos 2\theta$, which can be generalised in a different way to give the potential potential field described by the flux function

$$A = r^n \cos n\theta, \quad n > 1, \tag{2.19}$$

with field strength

$$|B| = nr^{n-1}.$$

This field will be investigated in more detail later.

2.3.2 General Symmetric Neutral Points

One may note that (2.18) satisfies the conditions

(*i*) $j = -\dfrac{1}{\mu}\left[\dfrac{1}{r}\dfrac{\partial}{\partial r}\left(r\dfrac{\partial A}{\partial r}\right) + \dfrac{1}{r^2}\dfrac{\partial^2 A}{\partial \theta^2}\right]$ is finite at $r = 0$

(*ii*) $B_r = \dfrac{1}{r}\dfrac{\partial A}{\partial \theta} = 0$ at $\theta = 0$ and $\theta = \dfrac{\pi}{2}$.

Another more general flux function that also satisfies these two conditions is

$$A = r^n\left[K - \cos 2m\theta\right], \tag{2.20}$$

where $n \geq 2$ and $m = 1, 2, 3, \ldots$. This has field components

$$B_r = 2mr^{n-1}\sin 2m\theta, \quad B_\theta = nr^{n-1}(\cos 2m\theta - K).$$

It has a magnetic field structure that is similar in each quadrant. The resulting electric current is

$$j = -r^{n-2}\left[n^2K + (4m^2 - n^2)\cos 2m\theta\right]/\mu. \tag{2.21}$$

Let us first consider the special case of (2.20) with $K = 0$, for which the separatrices $A = 0$ occur at angles given by

$$\cos 2m\theta = 0,$$

namely

$$\theta = (2M+1)\pi/4m, \quad M = 0, 1, 2, \ldots, 4m-1.$$

When $m = 1$ we have an X-point with

$$A = r^n \cos 2\theta, \tag{2.22}$$

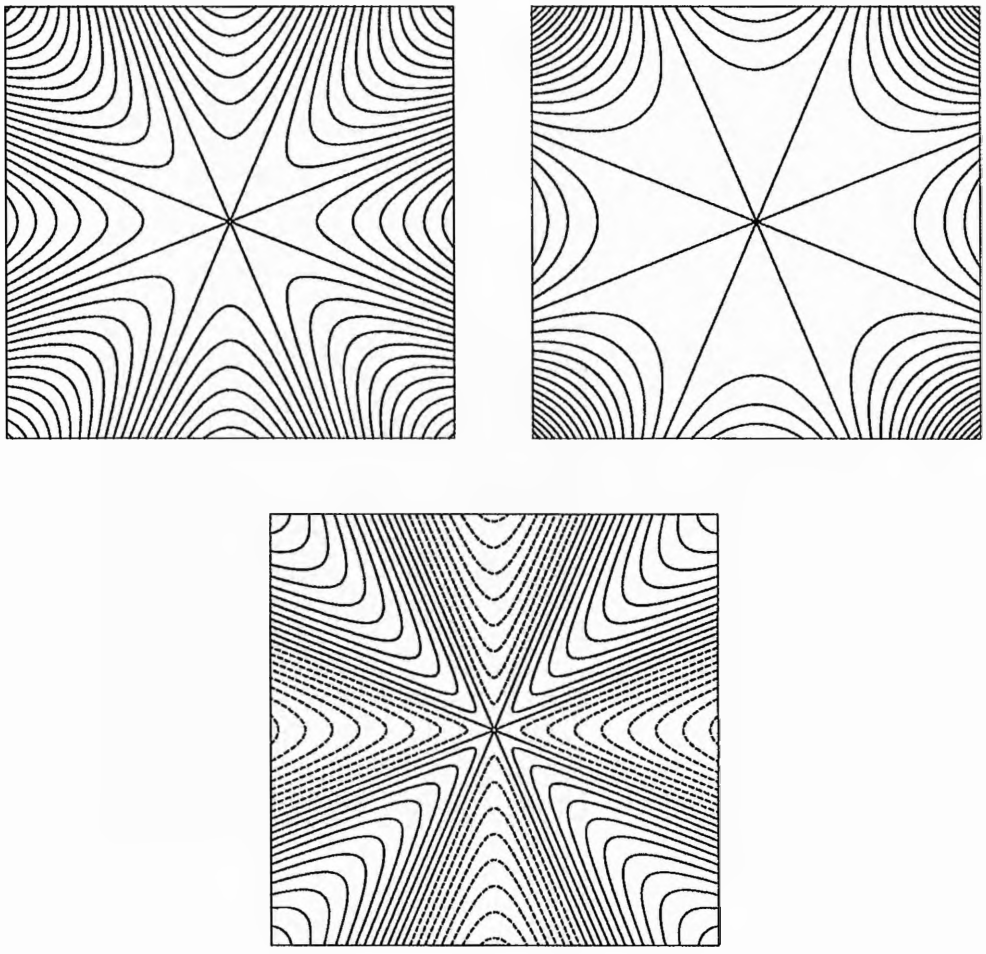

Figure 2.3: (a) The field lines and (b) the current density contours for symmetric star-points with $A = r^n \cos 4\theta$. Negative current is indicated by dashed curves. When $n = 4$ the current vanishes everywhere

having separatrices at $\theta = \pm\pi/4, \pm 3\pi/4$ and a current density of

$$j = r^{n-2}(n^2 - 4)\cos 2\theta/\mu. \tag{2.23}$$

This does not satisfy (2.9) when $n \neq 2$ and so there is no pressure field which can keep the configuration given by (2.22) in equilibrium. However, a steady state solution satisfying (2.12) and (2.15) can be found when the flow is not parallel to the magnetic field. For a field given by $A = r\cos 2m\theta$ the flow will be given by the stream function

$$\Psi = \frac{1}{\sqrt{\mu\rho}} r \sin 2\theta,$$

Although this leads to a singular current density at $r = 0$, the solution may be valid for reconnection models as ideal MHD breaks down near the null point.

When $m = 2$, the flux function reduces to

$$A = r^n \cos 4\theta, \tag{2.24}$$

which has separatrices at $\theta = \pi/8$ and $\theta = 3\pi/8$ in the first quadrant. The field structure may be called a *star-point* , and the corresponding current density is

$$j = -r^{n-2}(n^2 - 16)\cos 4\theta/\mu.$$

This process can be generalised for $m > 2$ giving further symmetric star-points with m separatrices in each quadrant. Potential star-points, which can be generated using the real part of the complex flux function $A = re(-z^{2n})$, have been discussed by Syrovatsky (1971) in relation to current sheet formation.

Alternatively, solutions of the form $A = r^n \cos 2m\theta$ can be added in a power series starting with the potential solution $r^{2m} \cos 2m\theta$ to obtain the Bessel function solution

$$A = J_{2m}(\alpha r)\cos 2m\theta, \tag{2.25}$$

which yields $\mu j = \alpha^2 A$, so (2.25) represents a static equilibrium when there is a pressure $p = \alpha^2 A^2/2\mu$ given by (2.10). The field lines are shown in Figure 2.2 for the potential X-point and the Bessel function case when $m = 1$. Star point structures are shown in Figure 2.3 for the case $m = 2$.

Consider next the general case of (2.20) when $K \neq 0$ for which the separatrices occur when $\cos 2m\theta = K$, namely

$$\theta = (2M + 1)\pi/4m \pm \gamma, \quad M = 0, 1, 2, \ldots, 4m - 1 \text{ with } \sin 2m\gamma = K.$$

When $m = 1$ we have a generalised X-point with

$$A = r^n \left[K - \cos 2\theta\right], \tag{2.26}$$

which has separatrices at $\theta = \pm(\pi/4 - \gamma), \pm(3\pi/4 + \gamma)$ where $\sin 2\gamma = K$, so that the separatrices previously at $\pi/4$ and $3\pi/4$ when $K = 0$ are rotated through an angle γ anti-clockwise and clockwise, respectively. The case $n = 2$ reduces to (2.18).

The field lines together with the current density contours given by

$$j = -\frac{r^{n-2}}{\mu}\left[n^2 K + (n^2 - 4)\cos 2\theta\right],$$

are shown in Figure 2.4. By comparison with the case $K = 0$, the symmetry about the $x-$ and $y-$axes remains, but the symmetry about $y = \pm x$ is lost.

When $m = 2$ we have a star-point with

$$A = r^n \left[K - \cos 4\theta\right], \tag{2.27}$$

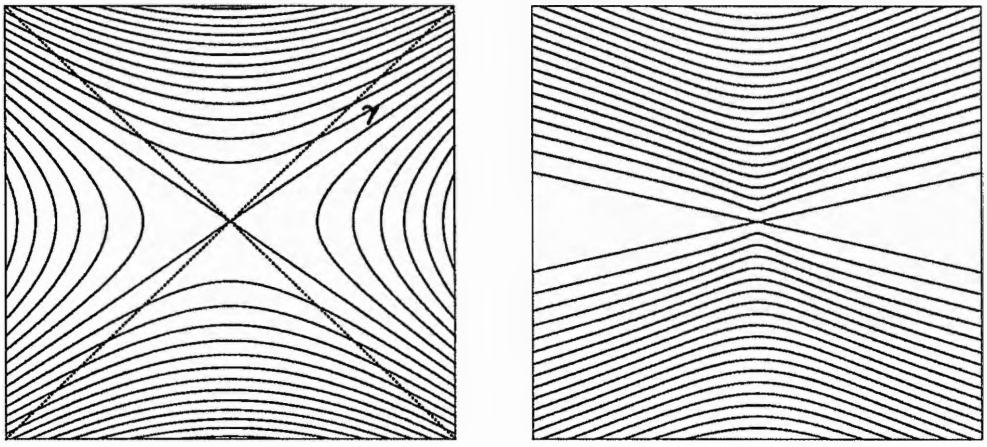

Figure 2.4: (a) The field lines and (b) the current density contours for an asymmetric X-point with $A = r^3(\cos 2\theta - K)$ when $\gamma = \pi/12$.

and separatrices at angles

$$\theta = \pm(\pi/8 - \gamma), \quad \theta = \pm(3\pi/8 + \gamma), \quad \theta = \pm(5\pi/8 - \gamma), \quad \theta = \pm(7\pi/8 + \gamma),$$

where $\sin 4\gamma = K$. The field lines and current density contours are shown in Figure 2.5.

For the case $K = \pm 1$, this star-point collapses to an X-point with neutral sheets along

$$\theta = 0, \pm\pi/2, \pi, \qquad (K = 1),$$

$$\theta = \pm\pi/4, \pm 3\pi/4 \quad (K = -1),$$

These differ from the previous X-points (Figure 2.2) where there were no reversal lines and the separatrices were flux surfaces (field lines in a two-dimensional section) rather than the neutral sheets that occur here.

Other symmetric star-points of the flux function of the form $A = r^n \cos 2m\theta$, $(m > 2)$ collapse in the same way producing $2m$ field reversal lines. The reader may easily construct these higher-order star-points in a similar fashion, though these flux functions do not satisfy (2.9) and the field will tend to evolve in a time-dependent manner.

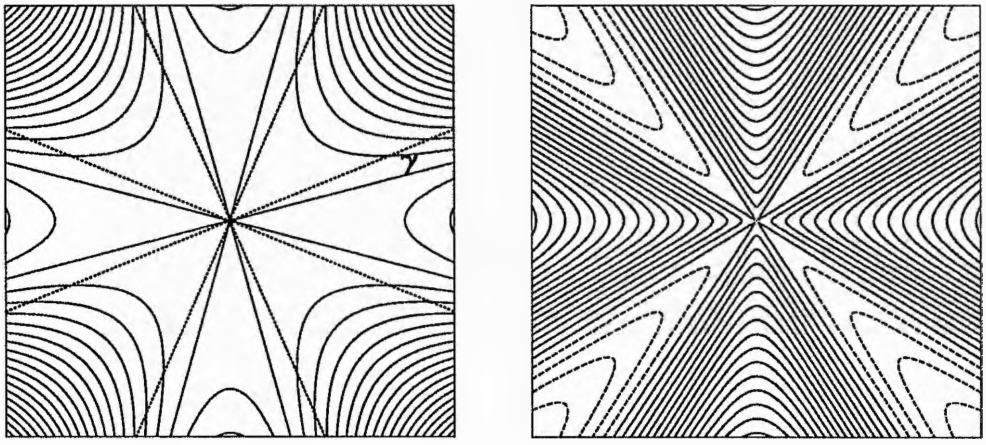

Figure 2.5: (a) The field lines and (b) the current density contours for a star-point with $A = r^3(\cos 4\theta - K)$ when $\gamma = \pi/16$.

2.4 Y-Points and Asymmetric Star-Points

2.4.1 Generalisations of the Potential Y-Point

In order to model a Y-point with the orientation shown in Figure 2.1(b), we may adopt a flux function of the form

$$A = r^n \cos\frac{3\theta}{2}, \tag{2.28}$$

where either $n = 3/2$, which gives a potential field (Figure 2.6(i)), or $n \geq 2$. This satisfies the conditions that

(*i*) j is finite at $r = 0$,

(*ii*) $B_\theta = -\dfrac{\partial A}{\partial r} = 0$ at $\theta = \pi$,

(*iii*) $B_r = \dfrac{1}{r}\dfrac{\partial A}{\partial \theta} = 0$ at $\theta = 0$.

The current density is

$$j = -\frac{1}{\mu}\left(n^2 - \frac{9}{4}\right) r^{n-2} \cos\frac{3\theta}{2},$$

and the field components are

$$B_r = -\frac{3}{2} r^{n-1} \sin\frac{3\theta}{2}, \quad B_\theta = -n r^{n-1} \cos\frac{3\theta}{2}.$$

The separatrices lie along the directions $\theta = \pm\pi/3$ and the field strength grows with distance like r^{n-1}. There is a current sheet where B_r changes from $(3/2)r^{n-1}$ at $\theta = \pi$ to $-(3/2)r^{n-1}$ at $\theta = -\pi$.

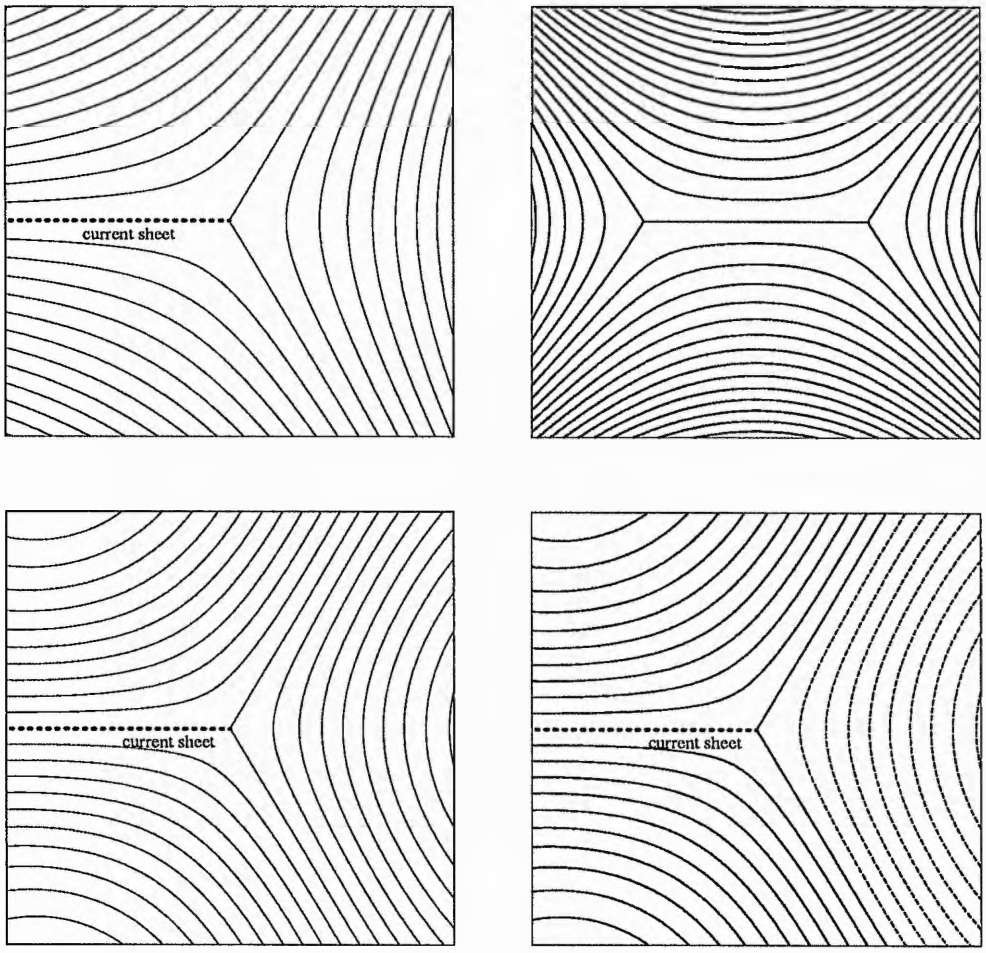

Figure 2.6: The field lines of a single potential Y-point with flux function $A = r^{3/2}\cos(3\theta/2)$ and a double Y-point given by a complex function. The Bessel function solution given by $A = J_{3/2}(\alpha r)\cos(3\theta/2)$ with the current density contours. Negative current is indicated by dashed curves.

The current in the sheet at a distance r from the origin is therefore

$$I = \frac{3}{\mu} r^{n-1},$$

and approaches zero at the origin. The potential solution (2.28) with $n = 3/2$ is in equilibrium with a uniform pressure, but none of the other solutions with $n > 2$ satisfy (2.9). However a steady state solution to (2.15) and (2.12) that has non-parallel flow and a singular current density at the null point exists when $A = -r\cos(3\theta/2)$ and $\Psi = -(\mu\rho)^{-1/2} r \sin(3\theta/2)$.

Again the Bessel function solution

$$A = J_{3/2}(\alpha r)\cos\frac{3\theta}{2}, \tag{2.29}$$

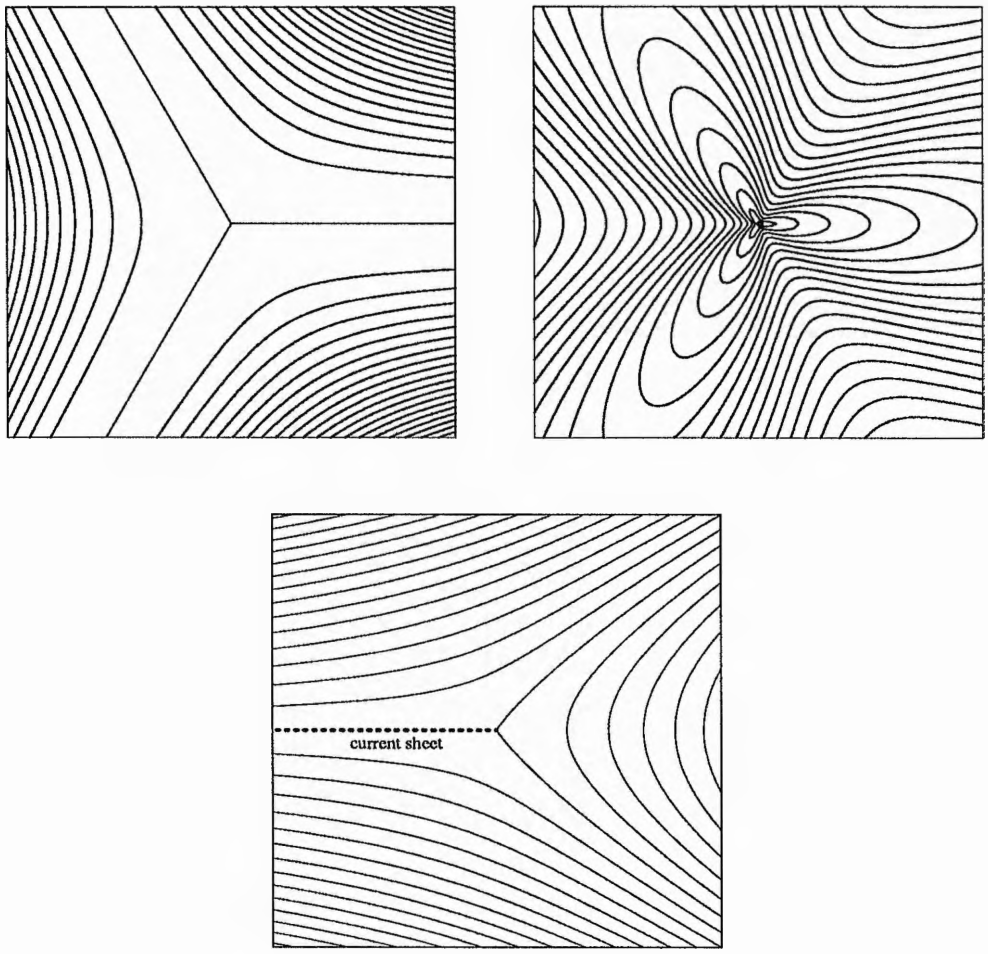

Figure 2.7: The field lines and current density contours for a Y-point with neutral sheets with $A = r^{5/2}(\cos 3\theta - 1)$ and the field lines for a Y-point having curved separatrices with $A = r^{3/2}\cos(3\theta/2) - r^2 \sin^2\theta$.

which has field components

$$B_r = -\frac{3\alpha}{2}\frac{J_{3/2}(\alpha r)}{(\alpha r)}\sin\frac{3\theta}{2},$$

$$B_\theta = \alpha\left[\frac{3}{2}\frac{J_{3/2}(\alpha r)}{(\alpha r)} - J_{1/2}(\alpha r)\right]\cos\frac{3\theta}{2},$$

can be generated, with $J_{1/2}(\zeta) = \sqrt{2/\pi\zeta}\,\sin\zeta$ and $J_{3/2}(\zeta) = \sqrt{2/\pi\zeta}\,(\sin\zeta/\zeta - \cos\zeta)$.

The current density is $\mu j = \alpha^2 A$ which satisfies (2.9). This will be in static equilibrium with a pressure $p = \alpha^2 A^2/2\mu$ given by (2.10). The Y-point is shown in Figure 2.6 along with the current density.

In the particular case $n = 3/2$, the volume currents vanish in the surrounding region and we

have a *potential Y-point* which has cartesian components

$$B_x = \frac{3}{2\sqrt{2}}\left[(x^2+y^2)^{1/2}+x\right]^{\frac{1}{2}},$$

$$B_y = \frac{3}{2\sqrt{2}}\left[(x^2+y^2)^{1/2}-x\right]^{\frac{1}{2}},$$

for $y > 0$, the negative square root being used for $y < 0$. Since j vanishes for this field, it is in equilibrium in the presence of a uniform pressure. An example of a field configuration that involves two such potential Y-points (at $x = \pm a, y = 0$) connected by a current sheet is, in terms of the complex variable $z = x + iy$, given by

$$B_y + iB_x = \left(z^2 - a^2\right)^{\frac{1}{2}}.$$

This configuration is shown in Figure 2.6. Other potential configurations with current sheets ended by Y-points have been discussed by Priest and Raadu (1975), Tur and Priest (1976) and Malherbe and Priest (1983) in connection with solar flares and solar prominences.

Another example of a Y-point is a collapsed six-pointed star-point described by the flux function

$$A = r^n\left[K - \cos 3\theta\right], \quad \text{when } K = \pm 1 \tag{2.30}$$

It differs from the previous Y-point in that it has three neutral sheets and no current sheet. This configuration is shown in Figure 2.7.

The separatrices of Y-points need not necessarily be straight. A constant current field with the properties

$$\frac{\partial A}{\partial r} = 0 \text{ at } \theta = \pi \text{ and } \frac{\partial A}{\partial \theta} = 0 \text{ at } \theta = 0,$$

can be added to produce curved separatrices. This will not affect the current sheet or the mathematical behaviour of the Y-point, i.e. the potential Y-point will not be reduced to a cusp-point or a T-point by the addition of a constant current. Equation (2.9) can also be satisfied for the constant current field. An example of this is shown in Figure 2.7.

2.4.2 General Asymmetric Neutral Points

The flux function (2.28) may be generalised to the form

$$A = r^n \cos(m+\frac{1}{2})\theta, \tag{2.31}$$

where $m = 1, 2, 3...$ and $n = (m + \frac{1}{2})$ or $n \geq 2$. It also satisfies the conditions (i)-(iii) above and describes *asymmetric star-points* . The field components are

$$B_r = -(m+\frac{1}{2})r^{n-1}\sin(m+\frac{1}{2})\theta, \quad B_\theta = nr^{n-1}\cos(m+\frac{1}{2})\theta,$$

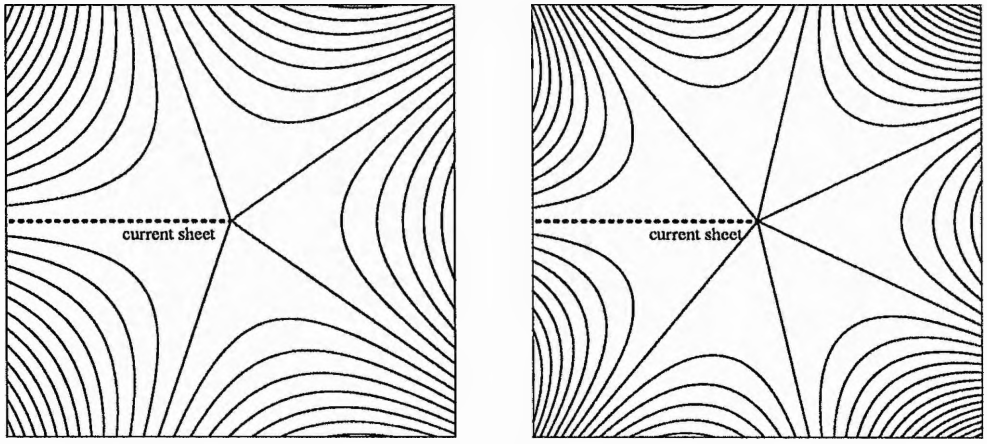

Figure 2.8: Field lines for asymmetric star-points with $A = r^n \cos(m + 1/2)\theta$ when (a) $m = 2$ and (b) $m = 3$.

and the current density is

$$j = -\frac{r^{n-2}}{\mu}\left(n^2 - (m+\frac{1}{2})^2\right)\cos(m+\frac{1}{2})\theta.$$

It can be seen that there is a current sheet at $\theta = \pi$ with current density of magnitude

$$I = (m+\frac{1}{2})\frac{r^{n-1}}{\mu},$$

which vanishes at the origin. Separatrices occur at

$$\theta = (2M+1)\pi/(2m+1), \quad M = 0, 1, 2, \ldots, 2m.$$

Field lines for the cases $m = 2$ and $m = 3$ are shown in Figure 2.8, for which the separatrices occur at $\theta = \pm\pi/5, \pm 3\pi/5$ and $\theta = \pm\pi/7, \pm 3\pi/7, \pm 5\pi/7$ respectively. For these these neutral points the only line of symmetry is the x-axis. The particular case $n = m + \frac{1}{2}$ gives a potential field outside the current sheet and so is in equilibrium in the presence of a uniform plasma pressure. Bessel function solutions representing equilibrium fields satisfying (2.9) also exist with a pressure given by $p = \alpha^2 A^2/2\mu$.

Other asymmetric star-points can be created using the flux function

$$A = r^n\left[K - \cos(2m+1)\theta\right], \tag{2.32}$$

Here there are, as in the case of the collapsed six- and eight-pointed star-points, only neutral sheets dividing the $2m + 1$ regions.

2.5 Cusp-Points and T-Points

2.5.1 Two Dimensional Cusp-Point Models

A *double cusp-point* may be modelled by a flux function

$$A = y^2 - c^2x^4, \tag{2.33}$$

for which the separatrices are

$$y = \pm cx^2,$$

and so are tangential to the x-axis at the origin. The field components and current density are

$$B_x = 2y, \quad B_y = 4c^2x^3,$$

and

$$j = -\frac{1}{\mu}(2 - 12c^2x^2),$$

which is positive for $|x| > 1/(\sqrt{6}c)$.

A more general field with a similar double-cusp form is given by

$$A = y^{2m} - c^{2m}x^{2n}, \tag{2.34}$$

with $m < n$ and $m = 1, 2, \ldots$.

The field components and current density are

$$B_x = 2my^{2m-1}, \quad B_y = 2nc^{2m}x^{2n-1},$$

and

$$j = -\frac{1}{\mu}(2m(2m-1)y^{2m-2} - 2n(2n-1)c^{2m}x^{2n-2}),$$

with separatrices given by

$$y = \pm cx^{n/m}.$$

Examples for $m = 1$ and $m = 2$ with $c = 1$ are shown in Figure 2.9.

A double-cusp has been suggested by Priest and Cowley (1975) to exist in the interior of the Sweet-Parker diffusion region which is at the centre of most reconnection models. Priest and Cowley consider a steady balance between the Lorentz force, a pressure gradient and an inertial term and investigate continuous solutions using a power series expansion. A similar approach is adopted by Yeh (1976) where the power series expansion about the neutral point is more general as it includes logarithmic terms. Our purpose here is to consider even more general solutions, including some containing discontinuities (current sheets). In all cusp-point solutions presented here there is no

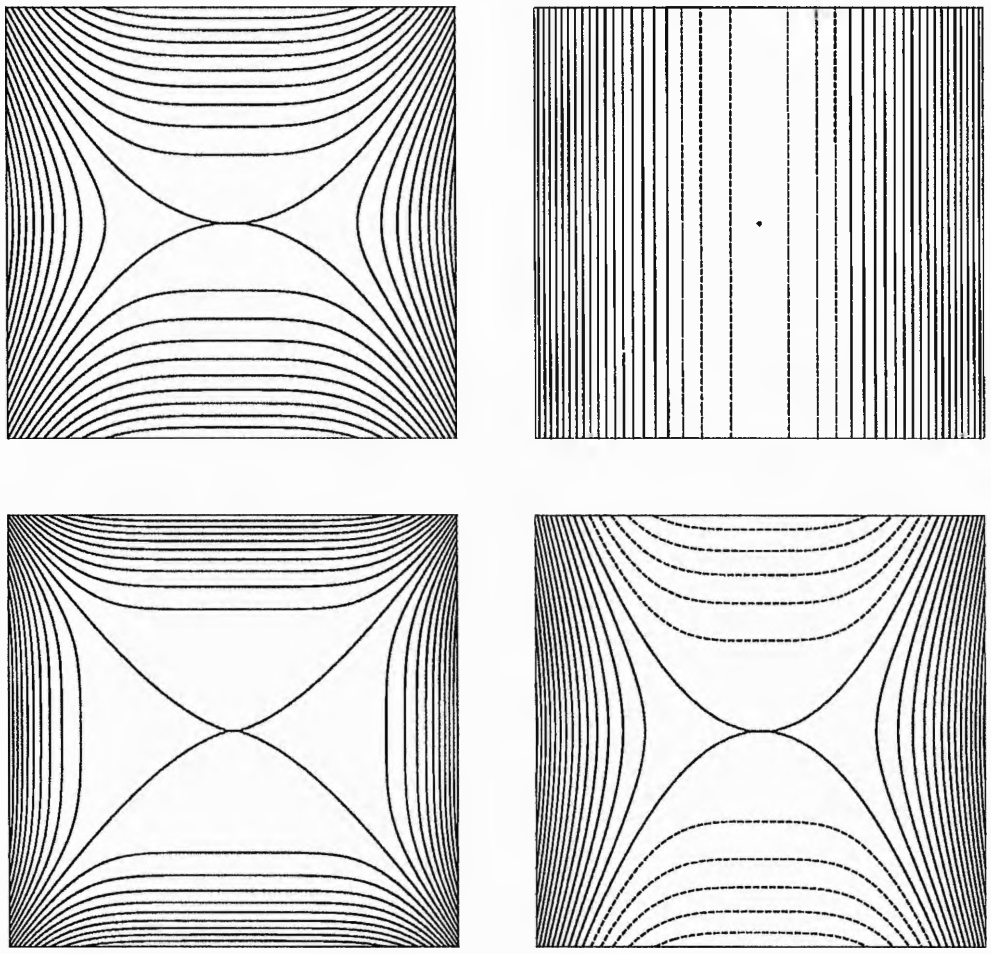

Figure 2.9: The field lines and current density for double cusp-points with $A = y^{2m} - x^{2n}$ when (a) $m = 1$, $n = 2$ and (b) $m = 2$, $n = 3$. Negative current is indicated by dashed curves.

equilibrium since flows are driven by unbalanced magnetic tension and pressure forces and solutions of the form (2.33) cannot satisfy (2.9). Also steady state solutions are not possible and the fields will evolve in a time-dependent manner.

A *single cusp-point* has the same field as above for $x > 0$, but straight field lines for $x < 0$ (Figure 2.10). Corresponding to (2.33), therefore we have

$$A = \begin{cases} y^2 - c^2 x^4, & x \geq 0, \\ y^2, & x < 0. \end{cases} \tag{2.35}$$

The field components and current density are

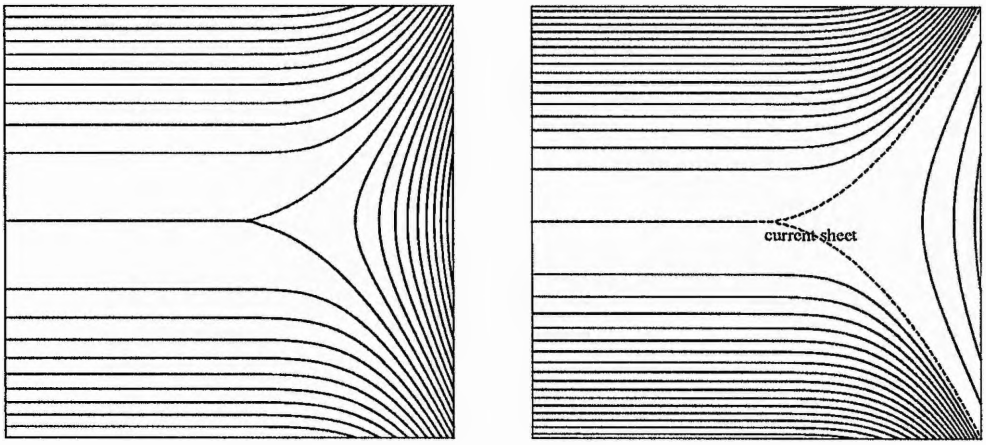

Figure 2.10: The field lines of a single cusp-point and a single cusp-point with current sheets along the separatrices..

$$B_x = 2y, \quad B_y = \begin{cases} 4c^2x^3, & x \geq 0, \\ 0, & x < 0, \end{cases}$$

and

$$j = \begin{cases} 2 - 12c^2x^2, & x \geq 0, \\ 2, & x < 0. \end{cases}$$

Corresponding to (2.34) a single cusp-point would have

$$A = \begin{cases} y^{2m} - c^{2m}x^{4n}, & x \geq 0, \\ y^{2m}, & x < 0. \end{cases} \tag{2.36}$$

A single cusp-point has been suggested by Pneuman and Kopp to exist at the summit of a helmet streamer. (Further details are in Priest, 1982 and Pneuman and Kopp, 1970.) They have current sheets dividing open and closed field regions of the corona in order to account for the pressure jumps between these regions. This may be modelled by, for instance,

$$A = \begin{cases} a(y^2 - c^2x^4), & y^2 > c^2x^4, \quad x \geq 0 \\ b(y^2 - c^2x^4), & y^2 \leq c^2x^4, \quad x \geq 0 \\ ay^2, & x < 0. \end{cases} \tag{2.37}$$

with $a > b$ to be consistent with the pressure jump from closed to open field regions (Figure 2.10).

2.5.2 Generalised T-Points

T-points were first investigated by Chapman and Ferraro (1931) in their magnetospheric models and are often referred to as Chapman-Ferraro neutral points. A *potential T-point* (Figure 2.11) may be constructed with a flux function

$$A = \begin{cases} -x, & x \geq 0, \\ -xy, & x < 0, \quad y \geq 0, \\ xy, & x < 0, \quad y < 0. \end{cases} \tag{2.38}$$

for which the field components are

$$B_x = \begin{cases} 0 \\ -x \\ x \end{cases} \qquad B_y = \begin{cases} 1, & x \geq 0, \\ y, & x < 0, \quad y \geq 0, \\ -y, & x < 0, \quad y < 0. \end{cases}$$

The volume current vanishes everywhere and so within each region there is an equilibrium in the presence of a uniform plasma pressure, but there is a current sheet along the y-axis with a current

$$I = \frac{1}{\mu}(1 - |y|),$$

which peaks at the origin and reverses at $|y| = 1$; this current sheet is not in equilibrium because the magnetic pressure is not equal on either side of it. There is also a current sheet located along the negative x-axis with a current

$$J = \frac{2x}{\mu},$$

which vanishes at the origin. Magnetic pressure is continuous across this.

The above T-point flux function may be written in cylindrical polar coordinates as

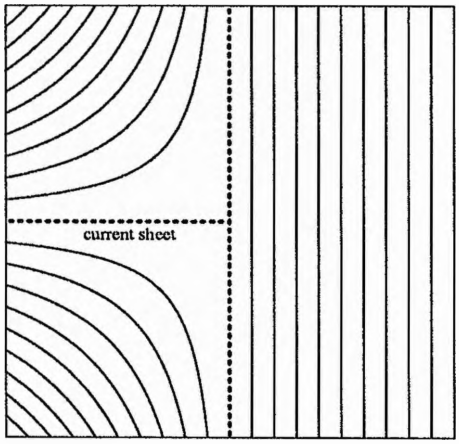

Figure 2.11: A potential T-point with current sheets along the y-axis and negative x-axis.

$$A = \begin{cases} -r\cos\theta, & |\theta| \leq \pi/2, \\ |r^2 \sin\theta\cos\theta|, & |\theta| > \pi/2, \end{cases} \tag{2.39}$$

and it satisfies the conditions

(i) j is finite at r=0

(ii) $A = 0$ on $\theta = \pi/2, \pi$ and $3\pi/2$.

A more general T-point, also satisfying these conditions and having current sheets in the same places may be modelled by

$$A = \begin{cases} -r\cos\theta, & |\theta| \leq \pi/2, \\ |r^n \sin\theta\cos^{m_1}\theta|, & |\theta| > \pi/2, \end{cases} \tag{2.40}$$

where $n > 2, m_1 = 1, 2, 3 \ldots$. The field components for $\pi/2 < \theta < \pi$ are

$$B_r = (-1)^{m_1} \left[r^{n-1}\cos^{m_1-1}\theta(\cos^2 - m_1 \sin^2)\right],$$

$$B_\theta = (-1)^{m_1+1} \left[nr^{n-1}\sin\theta\cos^{m_1}\theta\right],$$

and for $\pi < \theta < 3\pi/2$ are

$$B_r = (-1)^{m_1+1} \left[r^{n-1}\cos^{m_1-1}\theta(\cos^2 - m_1 \sin^2)\right],$$

$$B_\theta = (-1)^{m_1} \left[nr^{n-1}\sin\theta\cos^{m_1}\theta\right],$$

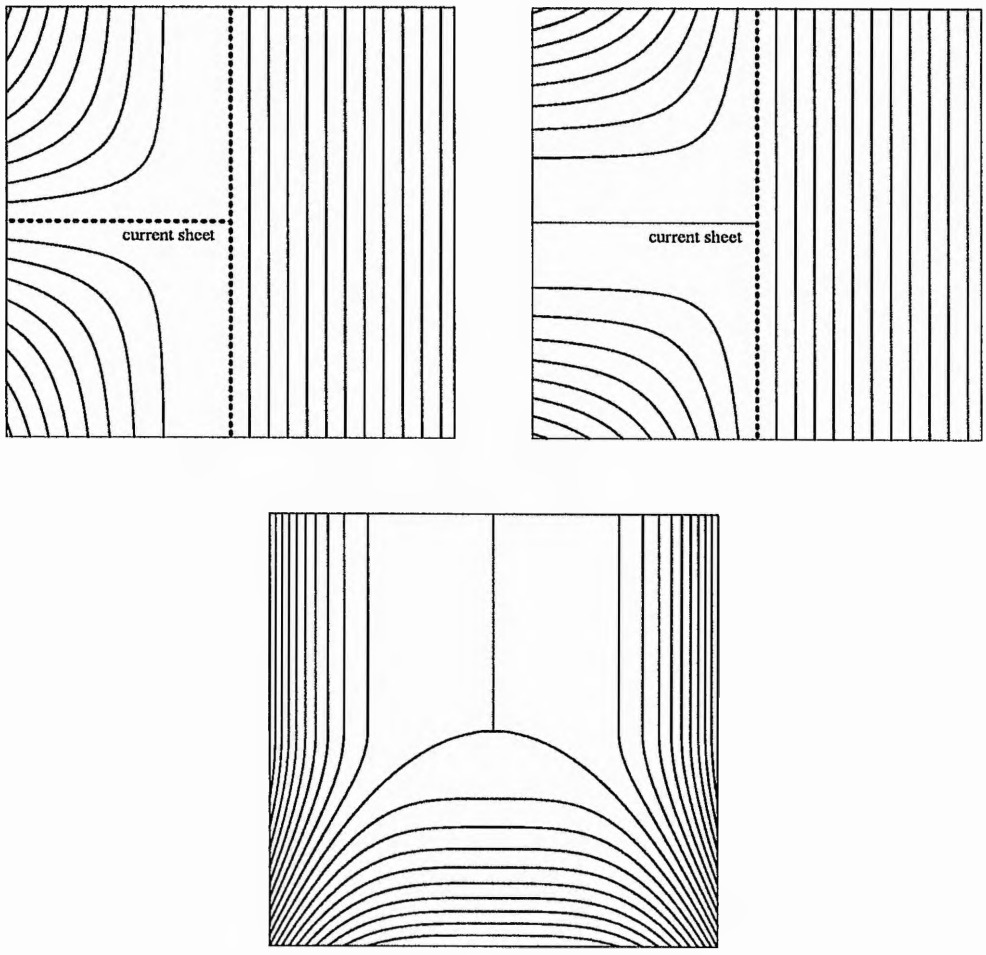

Figure 2.12: T-points with $A = |r^2 \sin^{m_1}\theta \cos^{m_2}\theta|$ for $\pi/2 < \theta < 3\pi/2$ when (a) $m_1 = 1$, $m_2 = 2$ and (b) $m_1 = 2$, $m_2 = 1$. Also, a T-point with curved separatrices.

with current density

$$j = -\frac{1}{\mu} r^{n-2} \sin\theta \cos^{m_1-2}\theta \left[(n^2 - 3m_1 - 1)\cos^2\theta + m_1(m_1-1)\sin^2\theta\right].$$

A T-point satisfying the above conditions but with a neutral sheet at $\theta = \pi$ may be modelled by

$$A = \begin{cases} -r\cos\theta, & |\theta| \le \pi/2, \\ |r^n \sin^{m_2}\theta \cos^{m_1}\theta|, & |\theta| > \pi/2, \end{cases} \tag{2.41}$$

where $n > 2, m_1 = 1, 2, m_2 = 2, 3 \ldots$. The field components for $\pi/2 < \theta < \pi$ are

$$B_r = (-1)^{m_1}\left[r^{n-1}\sin^{m_2-1}\theta\cos^{m_1-1}\theta(m_2\cos^2 - m_1\sin^2)\right],$$

$$B_\theta = (-1)^{m_1+1}\left[nr^{n-1}\sin^{m_2}\theta\cos^{m_1}\theta\right],$$

and for $\pi < \theta < 3\pi/2$ are

$$B_r = (-1)^{m_1+m_2+1}\left[r^{n-1}\sin^{m_2-1}\theta\cos^{m_1-1}\theta(m_2\cos^2 - m_1\sin^2)\right],$$

$$B_\theta = (-1)^{m_1+m_2}\left[nr^{n-1}\sin^{m_2}\theta\cos^{m_1}\theta\right],$$

with current density

$$j = -\frac{1}{\mu}\kappa\left[(n^2-(m_1+m_2)^2)\sin^2\theta\cos^2\theta + m_1(m_1-1)\sin^2\theta + m_2(m_2-1)\cos^2\theta\right],$$

where $\kappa = r^{n-2}\sin^{m_2-2}\theta\cos^{m_1-2}\theta$. Some examples are shown in Figure 2.12.

More generally, the separatrices need not be straight, whilst preserving the mathematical properties of the field near the T-point. For instance a non-potential T-point (Figure 2.12) with no current sheets, but having curved separatrices may be modelled by

$$A = \begin{cases} y^2 - c^2x^4, & y \le 0, \\ -c^2x^4, & y > 0. \end{cases} \tag{2.42}$$

with field components

$$B_x = \begin{cases} 2y, & y \le 0, \\ 0, & y > 0, \end{cases} \qquad B_y = 4c^2x^3.$$

The curved separatrices may be reduced to current sheets in a similar way as before. Configurations given by (4.10) do not satisfy (2.9) or (2.15) so time-dependent flows are driven by unbalanced forces.

From these models, it is observed that the classification for the difference between Y-, T- and cusp-points given by Pneuman and Kopp does not necessarily hold. Here, fields for the cusp-points presented can tend to zero from all principal directions, as can the non-potential T-point field with curved separatrices. What is always true, however, is that the magnetic field tends to zero *more* quickly along the principal directions indicated by the arrows in Figure 2.1. That is to say, the flux function A is of a higher order as one approaches the various neutral points along the arrowed paths.

2.6 A Self-Similar Cusp-Point Model

The final neutral point to be considered is a special solution to a cusp-point which arises from a magnetic equilibrium about a collapsed potential X-point. The collapse is due to a shearing motion solely into or out of the plane in which the initial X-point lies. The shear may be due to photospheric motions, for instance. Consequently, a third field component is introduced into the structure and so

it is unlike all the other neutral points described in this chapter. The third component is, however, only introduced to one quadrant of the initial X-point configuration causing a jump in the field across the separatrices between the regions with and without shear. This results in excess magnetic pressure in regions of shear over regions without shear, so a new magnetic equilibrium must be established.

If we consider a magnetic field in the $x-y$ plane and introduce a third component of field in the z-direction, which is dependent only on x and y, then

$$\mathbf{B} = \mathbf{B}(x,y) = \nabla \times A(x,y)\hat{\mathbf{z}} + B_z(x,y)\hat{\mathbf{z}}, \tag{2.43}$$

where $A(x,y)$ is the flux function. Also, if we assume that the magnetic field is force-free ($\mathbf{j}\times\mathbf{B} = \mathbf{0}$), which is a good approximation for most of the corona, then by substitution from (2.43) we obtain

$$B_z(x,y) \equiv B_z(A); \qquad \nabla^2 A + \frac{d}{dA}\left(\frac{B_z^2(A)}{2}\right) = 0, \tag{2.44}$$

the Grad-Shrafanov equation. Solutions satisfying this will therefore take the form

$$\nabla^2 A = F(A), \tag{2.45}$$

where F is some function of A alone.

B_z, however, is also dependent on the shear. The shear, $d = d(z)$, is simply the net displacement between one footpoint of a field line and the other, so $d(z) = d(A)$. By considering the ratio of field components in the $x-y$ plane to the z-component, we see that

$$\frac{dz}{ds} = \frac{B_z}{B_p}, \tag{2.46}$$

where ds is measured along the poloidal field and B_p is the poloidal field strength. Integrating (2.46) from one end of a field line to the other we find

$$B_z(A) = \frac{d(A)}{V(A)}, \tag{2.47}$$

where

$$V(A) = \int_1^2 \frac{ds}{B_p},$$

and 1 and 2 denote the footpoints of a particular field line.

2.6.1 Vekstein-Priest Self-Similar Solution

To satisfy a magnetic equilibrium we must therefore satisfy both (2.44) and (2.47). Vekstein and Priest (1991) realised that this is not possible in an X-type configuration where the separatrices

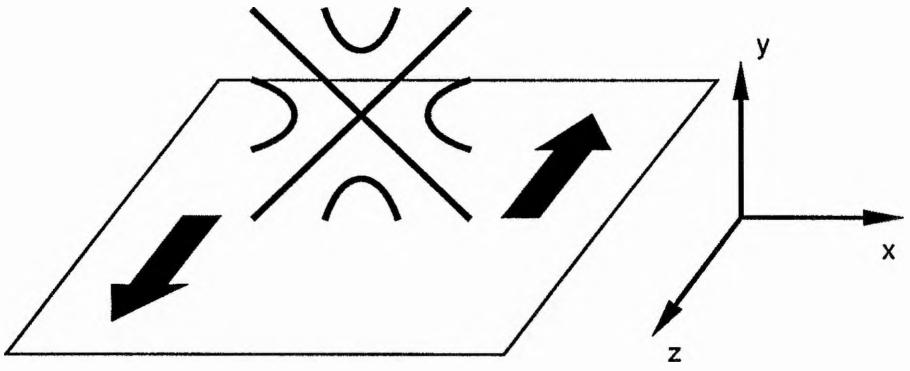

Figure 2.13: A potential X-point subject to footpoint motions into and out of the plane in which it lies.

meet at an angle. Instead they proposed a self-similar solution with the separatrices touching at the neutral point, which will be a cusp. The flux function is of the form

$$A(r,\theta) = r^{\alpha} f(\xi), \tag{2.48}$$

where $\xi = \theta/(kr^{\beta})$ is the similarity variable and $\alpha, \beta > 0$ with the separatrices given by $r = (\theta/k)^{1/\beta}$. This means that $\xi = \pm 1$ define the separatrices, so $f(\pm 1) = 0$. The poloidal magnetic field components derived from (2.48) are

$$B_r = \frac{1}{r}\frac{\partial A}{\partial \theta} = \frac{1}{k} r^{\alpha-1-\beta} f'(\xi), \tag{2.49}$$

$$B_r = -\frac{\partial A}{\partial r} = r^{\alpha-1}\left[\beta\xi f'(\xi) - \alpha f(\xi)\right],$$

with $B_r = 0$ when $\xi = \theta = 0$. By the restriction of both B_r and $V(A)$ being finite as $r \rightarrow 0$, the inequality

$$1 + \beta < \alpha < 2 + \beta, \tag{2.50}$$

is obtained.

To satisfy (2.45) we have

$$\nabla^2 A = \frac{1}{r}\frac{\partial}{\partial r}\left(r\frac{\partial A}{\partial r}\right) + \frac{1}{r^2}\frac{\partial^2 A}{\partial \theta^2} = -B_z(A)\frac{\partial B_z}{\partial A} \equiv F(A). \tag{2.51}$$

Vekstein and Priest neglect the first term in $\nabla^2 A$, as an expansion close to $r = 0$ is sought, so

$$\nabla^2 A \approx \frac{1}{r^2}\frac{\partial^2 A}{\partial \theta^2} = r^{\alpha-2-2\beta}\frac{f''(\xi)}{k^2} = F(A). \tag{2.52}$$

This yields a necessary power law behaviour for $F(A)$, namely

$$F(A) = -\epsilon A^{-n}, \tag{2.53}$$

where, from (2.48) and (2.52),

$$n = (2\beta + 2 - \alpha)/\alpha, \tag{2.54}$$

so, by (2.50), $n > 0$. The function $f(\xi)$ must therefore be a solution of

$$f''(\xi) = -\frac{\kappa}{2} f^{-n}, \tag{2.55}$$

where $\kappa = 2\epsilon k^2$ subject to the conditions $f(\pm 1) = 0$, $f'(0) = 0$. As $\xi \to 1$, we note that f'' becomes singular. From (2.44) we also have

$$\epsilon A^{-n} = \frac{1}{2}\frac{d}{dA}\left(B_z^2(A)\right), \tag{2.56}$$

which must lead to finite B_z as $A \to 0$ so $n < 1$. Also by considering (2.47), we see that the behaviour of $V(A)$ must lead to finite B_z as $A \to 0$. Investigation of $V(A)$ about $A = 0$ yields

$$\frac{dV}{dA} \sim A^{((2+\beta-\alpha)/\alpha)-1}, \tag{2.57}$$

so matching powers between (2.56) and (2.47) we find

$$\frac{2+\beta-\alpha}{\alpha} - 1 = -n. \tag{2.58}$$

Equating (2.58) and (2.54) it is found that $\alpha = 2/(3(1-n))$ and $\beta = \alpha - 4/3$ with $1/2 < n < 1$. Subsequently, by considering a pressure balance across the separatrices with the non-sheared region, Vekstein and Priest (1993) have found that $\alpha = 1 + 3/2\beta$, so that

$$0 < \beta < \frac{1}{2}. \tag{2.59}$$

Also, the constant, κ, is dependent on n. It is found by setting $f'(1) = -1$ that

$$\kappa(n) = (1-n)I(n)^{1-n}, \tag{2.60}$$

where

$$I(n) = \int_0^1 \frac{dx}{\sqrt{1-x^{1-n}}}.$$

A plot of the field lines for a solution found by Vekstein and Priest is shown in Figure 2.14.

2.6.2 Next Order Solution

The above analysis is to lowest order. The relations for n, α and β will always hold. To find a solution to next order, we consider the full expression for (2.51), noting that

$$\frac{1}{r}\frac{\partial}{\partial r}\left(r\frac{\partial A}{\partial r}\right) \sim r^{\alpha-2}. \tag{2.61}$$

Consequently, a second power law for this term arises and (2.53) becomes

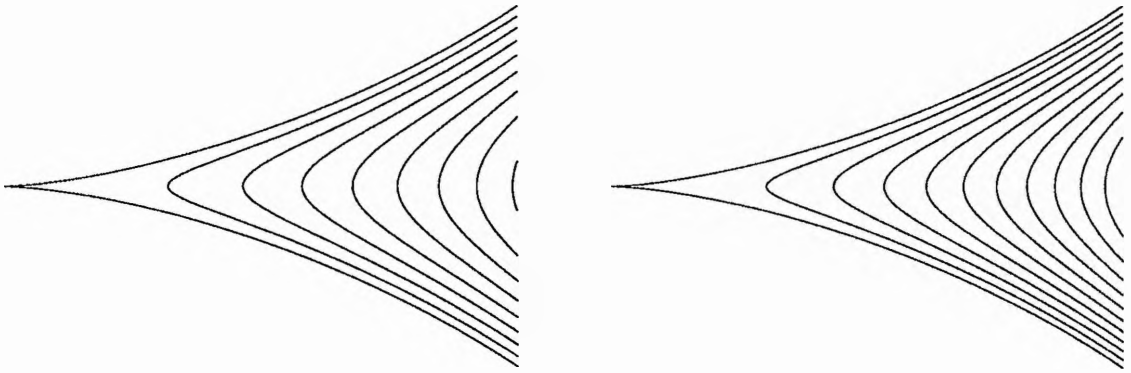

Figure 2.14: Self-similar cusp solutions when $n = 7/11$, $\alpha = 11/6$ and $\beta = 1/2$ showing the ordinary Vekstein-Priest solution on the left and the series solution on the right. The same contours are plotted in both.

$$\nabla^2 A = -\epsilon A^{-n} - \varphi A^{-m} = F(A), \tag{2.62}$$

where, from (2.48) and (2.60), $m = (2-\alpha)/\alpha$ with φ a constant.

Taking the full expression for (2.50), we see the function f must also satisfy

$$\alpha^2 f + (\beta - 2\alpha)\beta\xi f' + \beta^2\xi^2 f'' = -\varphi f^{-m} \tag{2.63}$$

Equations (2.54) and (2.63) provide two relationships for f which must both be satisfied subject to the same conditions as before. Substituting from (2.55) into (2.63), we see that

$$\alpha^2 \frac{f}{f''} + (\beta - 2\alpha)\beta\xi \frac{f'}{f''} + \beta^2\xi^2 = \frac{2\varphi}{\kappa} f^{n-m} \tag{2.64}$$

Observing that $n - m = 2\beta/\alpha > 0$, taking limits of both sides of (2.64) as $\xi \to 1$ yields

$$f''(1) = \frac{(2\alpha - \beta)}{\beta} f'(1). \tag{2.65}$$

The right-hand side of (2.65) is finite in this limit, so (2.65) contradicts (2.55). This means that, to next order, the flux function given by (2.48) is too restrictive.

We consider instead a power series of the form

$$A(r,\xi) = r^\alpha \sum_{j=0}^{\infty} C_j r^j f_j(\xi). \tag{2.66}$$

This yields field components

$$B_r = \frac{1}{k} r^{\alpha-1-\beta} \sum_{j=0}^{\infty} C_j r^j f_j'(\xi), \tag{2.67}$$

$$B_r = r^{\alpha-1} \sum_{j=0}^{\infty} C_j r^j \left[\beta\xi f_j'(\xi) - (\alpha+j) f_j(\xi)\right].$$

The separatrices are still defined as before, so $A(r,1) = 0$, which means

$$f_j(\pm 1) = 0, \quad \forall\, j.$$

Also, $B_r = 0$ when $\xi = 0$ so that

$$f_j'(0) = 0, \quad \forall\, j.$$

Expanding the Laplacian of A as before, we obtain

$$\nabla^2 A = \frac{1}{k^2} r^{\alpha-2-2\beta} \sum_{j=0}^{\infty} C_j r^j f_j'' + r^{\alpha-2} \sum_{j=0}^{\infty} C_j r^j \left[\alpha_j^2 f_j + (\beta - 2\alpha_j)\beta\xi f_j' + \beta^2 \xi^2 f_j''\right], \tag{2.68}$$

with $\alpha_j = \alpha + j$.

If $\beta \neq s/2$, where s is a positive integer, then (2.68) results in two separate power series between which the powers cannot match, hence

$$\nabla^2 A = -\epsilon A^{-n} - \varphi A^{-m} = F(A)$$

as before. By matching the leading terms in A^{-n} and A^{-m} we see that the same contradiction arises for f_0'' as $\xi \to 1$. Setting $\beta = s/2$, however, results in a single power series, so (2.68) becomes

$$\nabla^2 A = -\epsilon A^{-n}. \tag{2.69}$$

For instance, if $\beta = 1/2$, then $\alpha = 11/6$ and $n = 7/11$, so the first two terms in (2.69) give

$$-\epsilon A^{-\frac{7}{11}} \approx C_0 \frac{r^{-\frac{7}{6}}}{k^2} f_0'' + r^{-\frac{1}{6}} \left(\frac{C_0}{4} \left[\frac{121}{9} f_0 - \frac{19}{3} \xi f_0' + \xi^2 f_0'' \right] + C_1 \frac{f_1''}{k^2} \right). \tag{2.70}$$

Equating powers term by term, these differential equations can be solved for f_j numerically. Solutions for the sum of the first two terms in the expansion are shown along side the previous solutions found by Vekstein and Priest also for $\beta = 1/2$.

However, by (2.59), we see that $\beta = s/2$ is not allowed, so (2.66) cannot be used for the next order solution. This is not surprising because we expect to lose the self-similar form as r increases. In future it will be of interest to see what form can be used in place of (2.66) in order to match with both the unsheared potential region outside the cusp and an external solution.

2.7 Conclusions

Presented here is a classification and a set of models for the different types of hyperbolic neutral points in two dimensions. Such neutral points are important for the topology of magnetic equilibria since they represent sources or sinks of separatrices which separate topologically distinct areas of magnetic flux. They are also locations where current sheets tend to form and where field lines may break and reconnect.

X-type neutral points have been considered frequently in the past, particularly with regard to reconnection and current sheet formation. Here, however, we have generalised the usual potential and uniform-current models. Furthermore, when the separatrix pairs touch rather than cross at a non-zero angle, a double cusp-point is formed. Also, higher order (symmetric) neutral points, which are referred to as star-points, have an even number of separatrices, except when some collapse to an asymmetric star-point configuration with separatrices which are field reversal surfaces.

Y-points appear in some magnetic equilibria, especially at the ends of current sheets surrounded by potential fields. However, it has been shown here how more general Y-points with non-potential fields can exist and have also presented solutions for higher-order asymmetric star-points. Neutral sheets can also be ended by T-points or, for instance at the summit of a helmet streamer, by cusp-points and again a variety of solutions for the field close to such a neutral point have been presented along with a clarification of the definitions of field behaviour in the vicinity of these points.

The equilibrium solution presented in the last section demonstrates how the definitions derived in two-dimensions can be used in a specific two-and-a-half-dimensional model. The restrictions placed on the field by the footpoint displacement result in a cusp-point in order for there to be a magnetic equilibrium.

Chapter 3

A General Family of Nonuniform Reconnection Models with Separatrix Jets

3.1 Chapter Summary

In this chapter we explore a family of *Nonuniform Reconnection* models by introducing non-potential magnetic fields into the model presented by Priest and Lee (1990). This creates significant pressure gradients resulting in compressive and expansive regimes. As in the Priest and Lee analysis, the presence of a strong plasma jet at the separatrix and numerical solutions in the outflow are explored. In Section 1, previous reconnection models are reviewed. Section 2 gives a physical description of the effects of plasma pressure gradients in a magnetic field. Section 3 examines the shockless model and the diffusion region. In Section 4 a shock is incorporated in the downstream region and a new steady-state solution is found by numerically solving the MHD equations in the outflow region subject to new boundary conditions on the outflow boundary. Section 5 discusses the actual reconnection rate produced by these models and draws conclusions.

3.2 Introduction

For most astrophysical plasmas the global magnetic Reynolds number is extremely large so most of the magnetic field does not diffuse and is "frozen" to the plasma. However, if the length-scales

are sufficiently small, the field may diffuse, be broken and reconnected, releasing magnetic energy in the process. Such conditions exist in a diffusion region or current sheet. Originally Sweet (1957) and Parker (1958) conceived a model for this phenomenon in which diffusion alone is present, but the process is very slow. Petschek (1964) devised a much speedier energy release system that has a small Sweet-Parker diffusion region in the centre of the flow with two pairs of standing shock waves emanating from its ends. It is this basic configuration which has spawned subsequent steady-state models and will be studied here.

The configuration of the magnetic field that has two Y-points at the ends of a current sheet has long been recognised as a site for steady magnetic reconnection (e.g. Green, 1965; Syrovatsky, 1971; Priest and Raadu, 1975; Priest and Lee, 1990). We consider a current sheet of length $2L$ lying along the x-axis between $x = -L$ and $x = +L$, and the external magnetic field strength and flow speed at some point $(0,L_e)$, where $L_e \geq L$, are denoted by B_e and v_e, respectively. The corresponding field and flow just outside the current sheet are B_i and v_i and at a point $(L_e,0)$ on the outflow boundary are B_o and v_o. The aim of the analysis is to find the maximum reconnection rate in terms of the dimensionless Alfvén Mach number, M, where

$$M = \frac{v}{v_A}, \tag{3.1}$$

and $v_A = B/(\mu\rho)^{1/2}$ is the Alfvén speed. In particular we seek a relation between the current sheet half-length L, pressure distribution and the Alfvén Mach number. A shock stands in the flow near to the separatrix, though it is strictly speaking not a shock, but an Alfvénic discontinuity in the incompressible case studied here. The magnetic field may be either weakened or strengthened by the shock.

In the analysis carried out by Petschek (1964), he assumes that the inflow is a linear perturbation to a uniform field ($B_e\hat{\mathbf{x}}$), so it is potential and only slightly curved. The field he found has a value at the inflow to the diffusion region of

$$B_i = B_e - \frac{4v_e(\mu\rho)^{\frac{1}{2}}}{\pi} \log\frac{L_e}{L}. \tag{3.2}$$

The maximum reconnection rate, M_e^*, was found, by putting $B_i = \frac{1}{2}B_e$, to be

$$M_e^* = \frac{\pi}{8\log Le/L}. \tag{3.3}$$

For steady-state reconnection, inwards advection of flux equals outward diffusion, so the inflow speed to the diffusion region is

$$v_i = \frac{\eta}{\ell}, \tag{3.4}$$

where ℓ is the diffusion region width and η is the magnetic diffusivity. If plasma leaves the end of the diffusion region at v_{Ai}, the local Alfvén speed, then continuity of mass implies that

$$Lv_i = \ell v_{Ai}. \tag{3.5}$$

In the inflow region Ohm's law reduces to

$$\mathbf{E} + \mathbf{v} \times \mathbf{B} = 0, \tag{3.6}$$

where $\mathbf{E}=E\hat{\mathbf{z}}$ is the electric field, which is uniform and equal in magnitude to $Bv_\perp$ ($v_\perp$ being the component of the flow perpendicular to the field), which, when evaluated at the inflow to the diffusion region and at the external point $(0,L_e)$, leads to

$$E = v_i B_i = v_e B_e. \tag{3.7}$$

After eliminating ℓ and v_i between (3.4), (3.5) and (3.7), (3.3) becomes

$$M_e^* = \frac{\pi}{8\log(8R_{me}M_e^{*2})} \approx \frac{\pi}{8\log(R_{me})}, \tag{3.8}$$

where $R_{me} = L_e v_{Ae}/\eta$ is the magnetic Reynolds number based on the Alfvén speed (i.e the Lundquist number). This may be compared with the Sweet-Parker magnetic annihilation model, which considers only a balance between diffusion and inflow and has a reconnection rate of

$$M_i = R_{mi}^{-\frac{1}{2}}. \tag{3.9}$$

Equation (3.8) gives a value for the reconnection rate M of typically 0.1 against a much lower value for M_i from (3.9) when $R_m \gg 100$.

Following on from Petschek, Sonnerup (1970) proposed a model in which the maximum reconnection rate is of order unity and the inflow region is of slow-mode expansion nature; whereas Petschek had found a fast-mode expansion. By introducing pressure gradients into the inflow, Priest and Forbes (1986) created a *Unified Almost-Uniform* theory which includes as special cases the hitherto separate Petschek- and Sonnerup-like models and the stagnation-point flow model (Sonnerup and Priest, 1975) in which there is an infinitely long diffusion region. The Petschek-like solution is still potential, and hence has no significant pressure gradients, but, depending on the pressure distribution, the unified theory encompasses the one extreme of a slow-mode expansion (flux-pile-up) regime to the other of a slow-mode compression.

Further numerical models (Biskamp 1982, 1984, 1986; Forbes and Priest 1982a,b, 1983a,b,c, 1984a,b; Forbes 1986, 1988, 1990; Forbes and Malherbe 1986; Scholer 1989; Forbes *et al.* 1989) have found new and interesting features. Biskamp (1986) finds in his numerical experiments for a particular set of boundary conditions that Petschek reconnection is impossible for large values of the magnetic Reynolds number. Scholer (1989), however, does find Petschek reconnection for

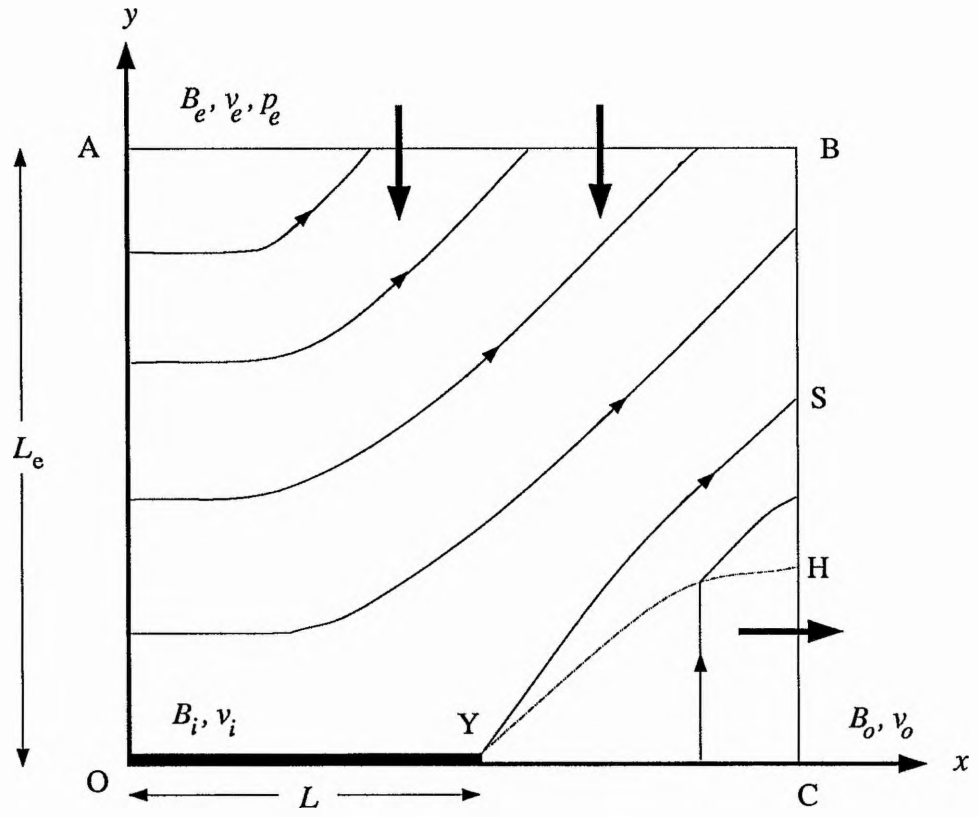

Figure 3.1: Schematic magnetic field lines in one quadrant showing a current sheet OY, separatrix YS and Alfvénic discontinuity YH. Bold arrows indicate the flow of plasma into and out of the region.

a spatially dependent resistivity that restricts the current sheet length. He also confirmed that boundary conditions, as stressed by Priest and Forbes (1986), are of crucial importance to the type of reconnection that results. Priest and Forbes (1992) show that the *Nonuniform Reconnection* models give the same scaling as Biskamp when his boundary conditions are adopted and so conclude that fast reconnection is highly likely with suitable boundary conditions.

Forbes and Priest (1987) clarified the whole range of regimes in relation to the inflow and outflow boundary conditions; Petschek reconnection is most likely to occur when the boundary conditions are free, for instance. The variation in boundary conditions coupled with more detailed investigations of the diffusion region (including some time-dependence and spatially varying diffusivity and resistivity) has highlighted four important features not present in the classical models:

a) the inflow can be compressive slow-mode with the magnetic field strengthening as one approaches the diffusion region, as well as expansive fast mode with a weakening field strength;

b) the inflow magnetic field can be highly curved;

c) strong plasma jets can exist along the separatrices (see also Soward and Priest, 1986);

d) reversed current spikes can be present at the ends of the diffusion region.

Features (b), (c), and (d) were all incorporated in the Priest-Lee *Nonuniform Model.* Here, by introducing significant inflow pressure gradients, we aim to include feature (a) as well. This will generalise both the Priest-Lee *Nonuniform Reconnection* model by adding pressure gradients and the Priest-Forbes *Almost-Uniform* model by allowing for strong inflow magnetic curvature and it will produce analytical solutions involving the whole, highly curved magnetic field.

3.3 The Inclusion of Inflow Pressure Gradients

In the Priest and Lee (1990) paper it is emphasised that the boundary conditions imposed on the numerical box bounding the whole reconnection region are crucial to the physical nature of the inflow and hence the regime of reconnection one expects to find. The number of independent boundary conditions one can impose in a two-dimensional ideal magnetohydrodynamic incompressible system, in which the inflow is slower than the normal Alfvén speed, is three (Forbes and Priest, 1987). This is the same as the number of characteristics propagating information into the region.

In the system we consider the following equations:

$$\nabla \cdot \mathbf{B} = 0, \tag{3.10}$$

the fundamental constraint on the magnetic field;

$$\mathbf{E} + \mathbf{v} \times \mathbf{B} = \mathbf{0}, \tag{3.11}$$

the electric field equation, where $\mathbf{E}$ is uniform for the two-dimensional analysis;

$$\rho(\mathbf{v} \cdot \nabla)\mathbf{v} = -\nabla \mathrm{p} + \mathbf{j} \times \mathbf{B}, \tag{3.12}$$

the equation of motion for a steady state, where $\mathbf{j}=\nabla \times \mathbf{B}/\mu$ is the current density, and

$$\nabla \cdot \mathbf{v} = 0, \tag{3.13}$$

the continuity equation for an incompressible plasma with uniform density, ρ.

It is the characteristics which result from (3.10) - (3.13) which determine the position of the Alfvénic discontinuity and there is also a mismatch between the characteristics above and below the separatrix (Soward and Priest, 1977). The slow magnetoacoustic speed is zero across the field so a shock can exist because the inflow is necessarily super-slow-magnetosonic. Streamlines will, in practice approach the separatrix at small angles if there is no pressure gradient. If there is a strong

pressure gradient acting to create an expansion as the flow comes in, however, the streamlines can approach the separatrix at steep angles, only being deflected toward the neutral point and out again in the vicinity of the separatrix (Figure 3.5 (a)).

We consider the case when the flow speed is much less than the Alfvén speed in the inflow, but, unlike the Priest-Lee model, the plasma β (the ratio of plasma to magnetic pressure) is not necessarily small so that there may be significant pressure gradients in the inflow region. Hence (3.12) reduces to

$$\mathbf{j} \times \mathbf{B} = \nabla \mathrm{p}. \tag{3.14}$$

If we take the curl of (3.14), we see that for the two-dimensional field

$$(\mathbf{B} \cdot \nabla)\mathbf{j} = \mathbf{0}, \tag{3.15}$$

which means the current is constant along the field lines. From (3.10) the field can be expressed as

$$\mathbf{B} = \nabla \times \mathbf{A}, \tag{3.16}$$

where $\mathbf{A} = A(x, y)\hat{\mathbf{z}}$ is the flux function, the contours of which are field lines in the x, y-plane, so the current density, j, is a function of A. Recasting j in terms of the flux function, we find

$$j = -\frac{1}{\mu}\nabla^2 A = f(A), \tag{3.17}$$

where ∇^2 is the Laplacian operator in two dimensions.

Consider the potential flux function $A_0(x, y)$ with $\nabla^2 A_0 = 0$ given by Priest and Lee, so that (3.17) is satisfied trivially. Now introduce an additional non-potential flux function $A_1(x, y)$ to produce a non-potential field from $A = A_0 + A_1$, for which (3.17) becomes

$$\nabla^2 A_1 = f(A_0 + A_1). \tag{3.18}$$

This is clearly a severe restriction on possible functions, A_1, which we overcome in the simplest way by seeking solutions to

$$\nabla^2 A_1 = constant. \tag{3.19}$$

Different solutions can be found for other flux functions (e.g. Chapter 2; Linardatos, 1992).

To find the pressure distribution, we rewrite (3.14) in terms of the flux function:

$$-\frac{1}{\mu}\nabla^2 A_1 \nabla A = \nabla p. \tag{3.20}$$

and note now that

$$\nabla p = \nabla A \frac{dp}{dA}$$

so (3.20) and (3.17) lead to

$$p = \int -\frac{1}{\mu}\nabla^2 A_1 \, dA = \int f(A) \, dA. \tag{3.21}$$

From (3.19) and (3.21), the pressure distribution is of the form

$$p(A) = p_0 + kA, \tag{3.22}$$

where k is a constant and p_0 is the background pressure.

The pressure distribution is of crucial importance for determining the nature of the reconnection taking place. If the pressure falls as one approaches the diffusion region the plasma undergoes an expansion and conversely if the pressure rises the plasma experiences a compression (Vasyliunas, 1975). Priest and Forbes (1986) in their unified model included a complete classification of the types of inflow:

> i) expansions (for which the pressure decreases) are of fast-mode type if the magnetic field decreases and slow-mode type if it increases as one approaches the diffusion region;
> ii) compressions (for which the pressure increases) are of slow-mode type if the magnetic field decreases and fast-mode type if it increases as one approaches the diffusion region.

For a fixed external Reynolds number R_{me} they found that reconnection rates much larger than the maximum Petschek rate are possible. The present model includes slow-mode compressions, fast-mode expansions and some slow-mode expansions, just as in the Priest-Forbes model. These are presented in the following section.

3.4 Reconnection Model

In this analysis we seek to extend the results of the Priest-Lee model to include significant pressure gradients in the inflow. Pressure gradients proved to be the link in the Priest-Forbes unified theory for *Almost-Uniform Reconnection,* bringing together the different regimes of reconnection, from Petschek to stagnation-point flow. The external inflow speed, v_e, magnetic field strength, B_e, and pressure, p_e, at a point $(0,L_e)$ and the outflow speed, v_o, at a point $(L_e,0)$, will all be prescribed (Figure 3.1). Then the upstream field and flow can be investigated to obtain the necessary information about the diffusion region, the shock relations and the downstream field and flow. There are three stages to the analysis: first, we consider the inflow region including the separatrix jets; then we investigate the behaviour of the diffusion region in relation to the inflow region; and finally the different reconnection regimes are explored by considering the downstream region with a given outflow speed, v_o.

3.4.1 Upstream Field, Flow and Pressure Distribution

For the steady-state two-dimensional model the basic equations are the electric field equation (3.11), the momentum equation with constant density, ρ, the divergence-free nature of the magnetic field (3.10) and mass continuity (3.13). We assume that the inflow is highly sub-Alfvénic, so the momentum equation reduces to (3.14).

The field outside the current sheet in the Priest-Lee model is a potential one which may be generated using complex variable theory. It is of the form

$$\frac{dA_0}{dZ} = B_y + iB_x = B_i \left(\frac{Z^2}{L^2} - 1 \right)^{\frac{1}{2}}, \tag{3.23}$$

where $Z = x + iy$ and there is a cut in the complex plane along the real axis between $Z = \pm L$. B_i is the value of the field just above the current sheet. By integrating and taking the real part, (3.23) yields a flux function

$$A_0 = -\frac{B_i}{2L} \left[xr - ys - L^2 \log \frac{\{(x+r)^2 + (y+s)^2\}^{\frac{1}{2}}}{L} \right], \tag{3.24}$$

where $r = \left[\frac{1}{2} \left((X^2 + Y^2)^{\frac{1}{2}} + X \right) \right]^{\frac{1}{2}}$, $s = \left[\frac{1}{2} \left((X^2 + Y^2)^{\frac{1}{2}} - X \right) \right]^{\frac{1}{2}}$, $X = x^2 - y^2 - L^2$ and $Y = 2xy$.

To obtain a constant-current field we can now add a flux function, A_1, satisfying (3.20). As the boundary conditions are the same with the new constant-current field, namely that $B_y = 0$ on the left-hand boundary and also on the lower boundary for $x \leq L$, and that $B_x = 0$ on the lower boundary for $x \geq L$, A_1 must produce only a B_x component which disappears on the x-axis. Hence

$$A_1 = -\frac{B_e}{2L_e} cy^2, \tag{3.25}$$

where c is a dimensionless parameter which is proportional to the magnitude of the current density. Thus, overall,

$$A = A_0 + A_1, \tag{3.26}$$

which leads to field components

$$B_x = B_i \frac{s}{L} - B_e \frac{cy}{L_e}, \quad B_y = B_i \frac{r}{L}, \tag{3.27}$$

with r and s as above.

By evaluating (3.27) at a point $(0, L_e)$, an expression for the internal field, B_i, in terms of the external field, B_e, is obtained:

$$B_i = \frac{B_e(1+c)}{(L_e^2/L^2 + 1)^{\frac{1}{2}}}. \tag{3.28}$$

The internal field B_i must be of the same sign as B_e, otherwise there would be an unwanted neutral point on the left-hand boundary. So, from (3.28), there is a restriction on the size of c to ensure that a field reversal does not occur, namely

$$c > -1 \,. \tag{3.29}$$

The pressure distribution is then determined from (3.14) and (3.25) using (3.21) and (3.22) to be

$$p(A) = p_e - \frac{B_e c}{\mu L_e}(A_e - A), \tag{3.30}$$

where p_e and A_e are the external pressure and flux function at the point (L_e,0). The pressure will therefore fall (an expansion) as one approaches the diffusion region for $c > 0$ and rise (a compression) for $c < 0$. This behaviour is similar to that in the Priest-Forbes models, which contain a parameter b such that along the inflow axis there is an expansion when $b > 0$ and a compression when $b < 0$. Clearly, we must ensure that the pressure remains positive throughout the region. This is not a problem in the compressive regime, where the pressure is always increasing, but is in the expansive regime when $c > 0$. By observing that $A_e \approx B_e L_e/2$ and noting that the flux function, A, is never less than $-A_e$ (at $(L_e, 0)$ when $L = 0$), the pressure remains positive provided $c < \beta_e/2$, where $\beta_e = p_e/(B_e^2/2\mu)$ is the plasma β externally. The effects that these pressure changes have on the reconnection rate will be explored later.

To evaluate the velocity field associated with the flow, we must consider the relationship between the field, which is known, and the flow, which has to be deduced. In the inflow region the electric field equation

$$\mathbf{E} + \mathbf{v} \times \mathbf{B} = 0, \tag{3.31}$$

implies that $E = -v_e B_e = -v_i B_i = -v_o B_o$. The velocity field, $\mathbf{v}$, can be written in terms of a stream function Ψ such that

$$v_x = \frac{\partial \Psi}{\partial y}, \; v_y = -\frac{\partial \Psi}{\partial x}, \tag{3.32}$$

which ensures that (3.13) is satisfied automatically. Equation (3.31) can then be expressed as

$$\mathbf{B} \cdot \nabla \Psi = v_e B_e, \tag{3.33}$$

which can be integrated along field lines (contours of the flux function, A), to give

$$\Psi = v_e B_e \int \frac{ds}{B}. \tag{3.34}$$

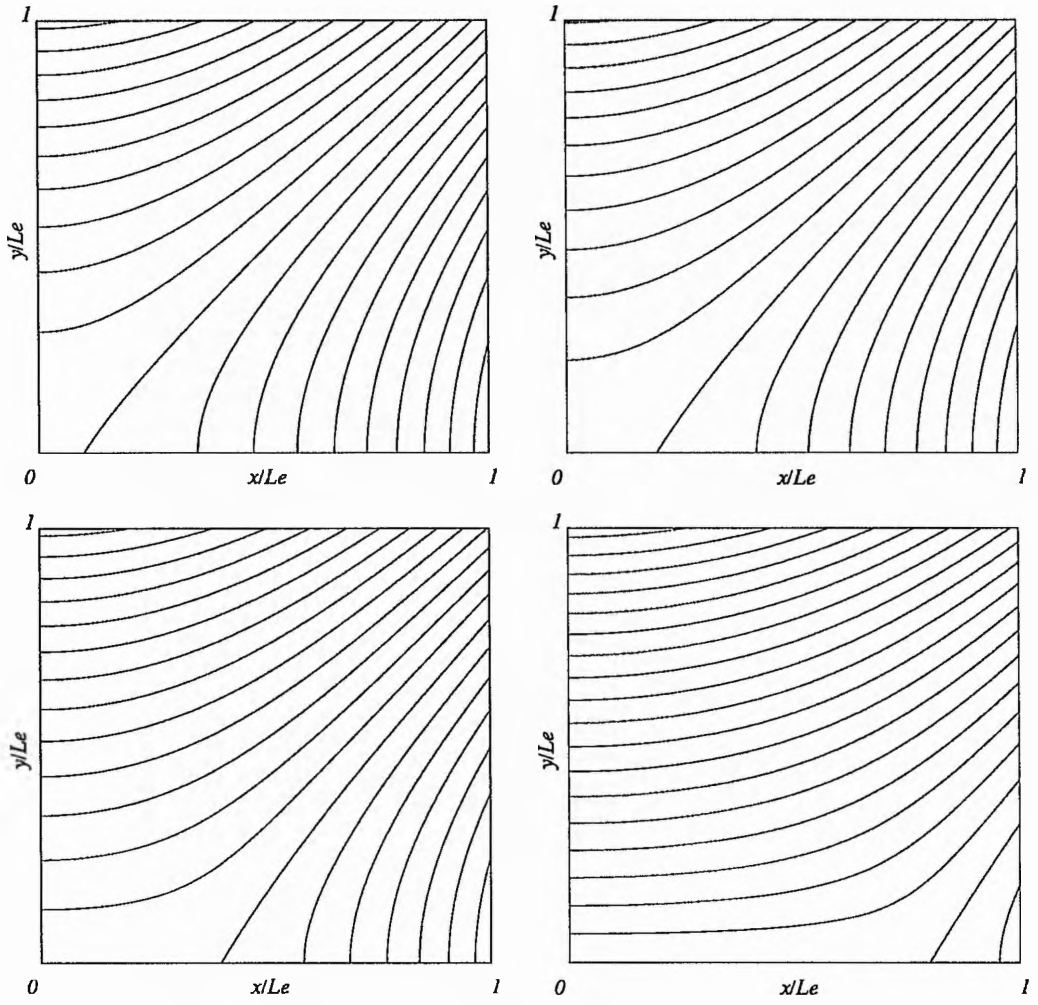

Figure 3.2: Magnetic field lines for shockless reconnection in the potential case $c = 0$ for different current sheet lengths, L ($0.1L_e, 0.2L_e, 0.4L_e$ and $0.8L_e$).

At the end, (L,0), of the current sheet the field vanishes, so (3.34) leads to a singularity. Also the value obtained for Ψ immediately above the separatrix differs from that obtained at a corresponding point immediately below. Integration above the separatrix is carried out from the y-axis, OA, where Ψ=0, whereas below the separatrix it is carried out from the x-axis, OC, where Ψ=0 also. The current sheet represents a site where the flow is deflected suddenly away from the neutral point along the x-axis, which will in reality occur over a finite width due to physical smoothing by non-ideal effects of viscosity and diffusivity.

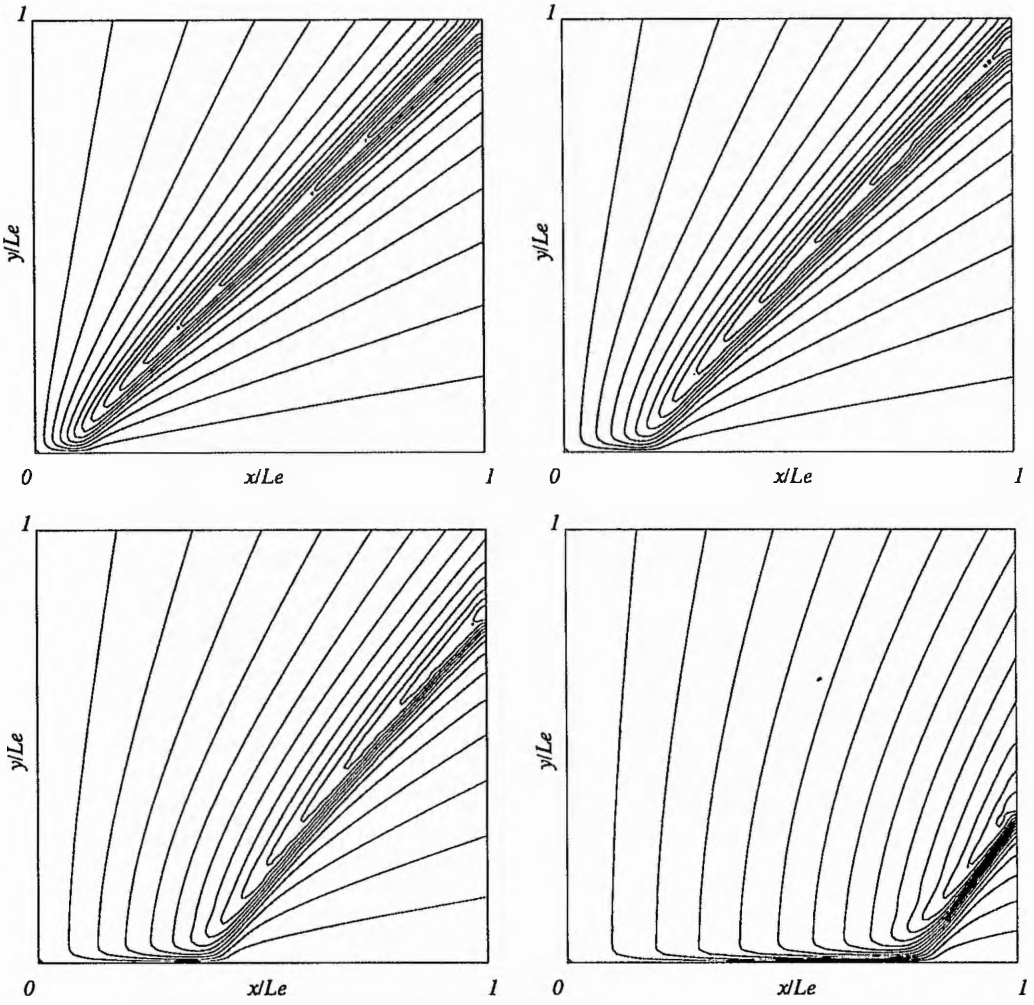

Figure 3.3: Streamlines for shockless reconnection in the potential case $c = 0$ for different current sheet lengths, L ($0.1L_e, 0.2L_e, 0.4L_e$ and $0.8L_e$).

3.4.2 Analysis of the Diffusion Region

Priest and Lee found the mass flux into the diffusion region to be

$$\int_0^L \rho v_y \, dx = \frac{1}{2}\pi\rho L v_i, \tag{3.35}$$

where $v_i = v_e B_e / B_i$. This still holds in the present analysis, though now (3.28) implies that B_i and therefore v_i changes with different values of the parameter c.

By assuming steady diffusion with inflow speed

$$v_i = \frac{\eta}{\ell}, \tag{3.36}$$

the diffusion region width is given by

$$\ell(x) = \frac{\eta}{v_y} = \frac{\eta}{v_i} \frac{(L^2 - x^2)^{\frac{1}{2}}}{L},$$

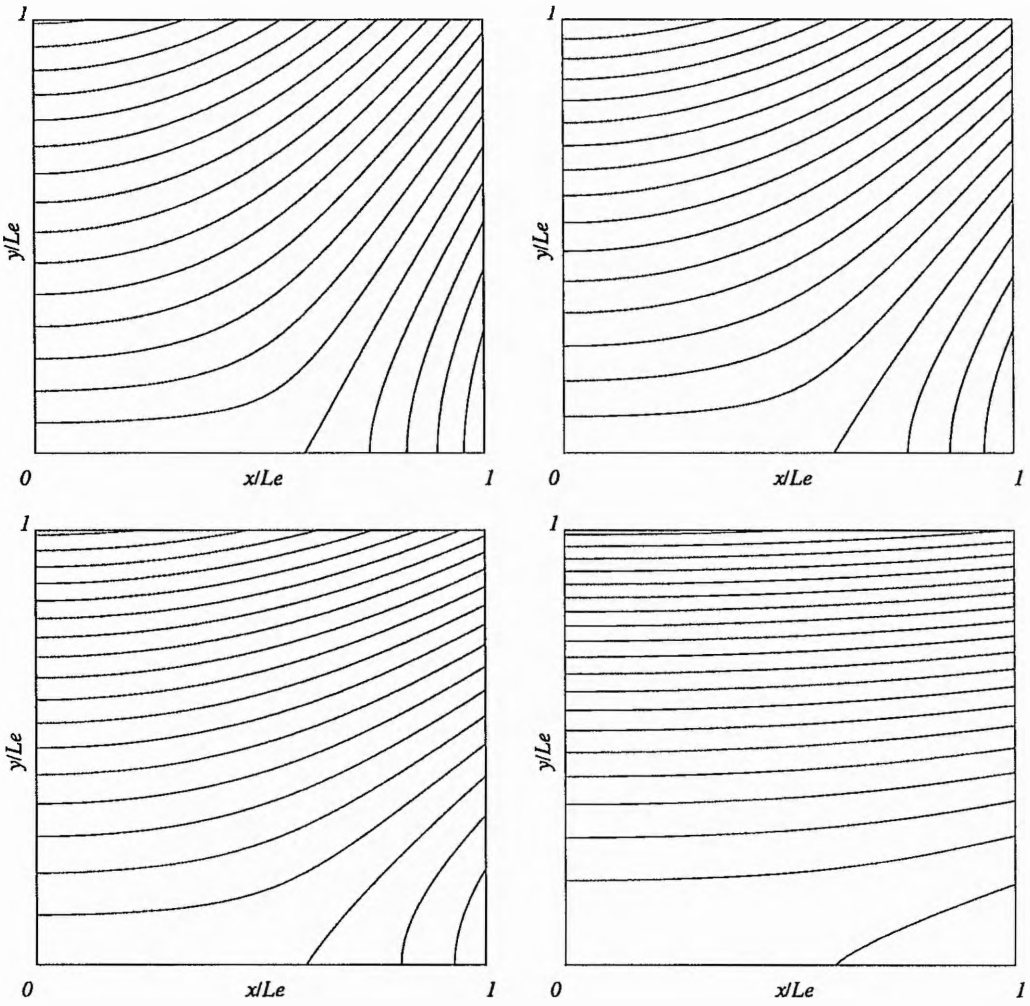

Figure 3.4: Magnetic field lines for shockless reconnection in the case $L = 0.6L_e$ for different constant currents, c (0.45, 0.0, -0.45, -0.31).

so that the diffusion region narrows as x increases towards L and the flow speed increases. Now also we see that its overall thickness decreases as v_i increases, i.e. as c decreases, and vice versa. Similarly, by considering mass continuity, Priest and Lee found the flow in the diffusion region to be

$$v_x = \frac{2v_{Ai}L}{\pi(L^2 - x^2)^{\frac{1}{2}}} sin^{-1}\frac{x}{L},$$

where $v_{Ai} = v_{Ae}B_i/B_e$ is the inflow Alfvén speed. Hence the flow slows as the overall diffusion width narrows (c decreases), but *increases* with x.

To investigate the nature of the separatrix jets, Priest and Lee proposed an order of magnitude model in which only a proportion (f) of the inflow exits the diffusion region into the outflow region with a speed v_{Ai}. The remaining $(1 - f)$ proportion forms the plasma jet. Using mass continuity they found

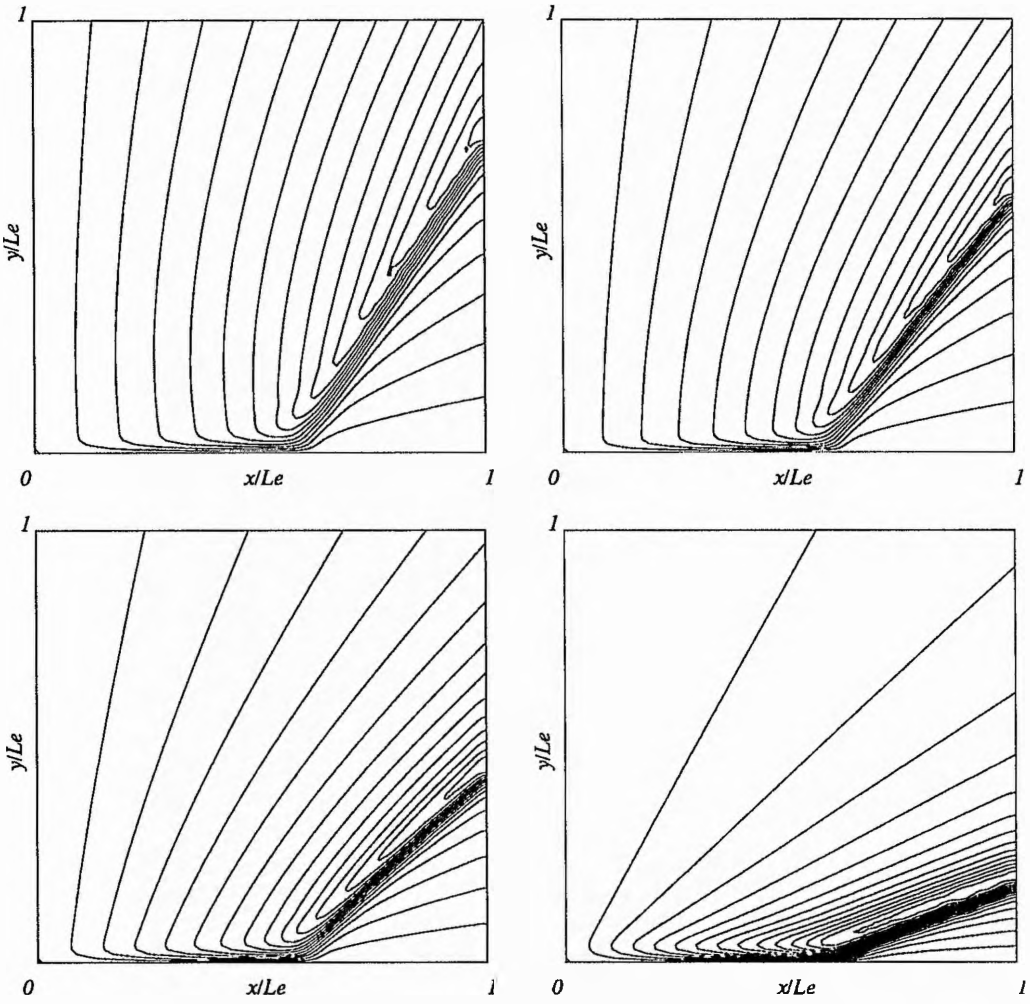

Figure 3.5: Streamlines for shockless reconnection in the case $L = 0.6L_e$ for different constant currents, c (0.45, 0.0, -0.45, -0.9).

$$f\frac{L}{L_e} = \frac{2}{\pi R_{me} M_e^2 (B_e/B_i)^3}. \tag{3.37}$$

Again in this model the effect of c on the ratio B_e/B_i changes the way this ratio and hence the Mach number, M_e, behaves. This will be considered in the following analysis.

3.4.3 Reconnection without Shocks

In the Priest-Lee model two cases were considered, firstly reconnection without including the effect of shocks and with a completely determined downflow region, and secondly reconnection in which outflow boundary conditions were altered in order to change the reconnection rate and the shock position as well as the outflow magnetic field and streamlines. The second approach produced

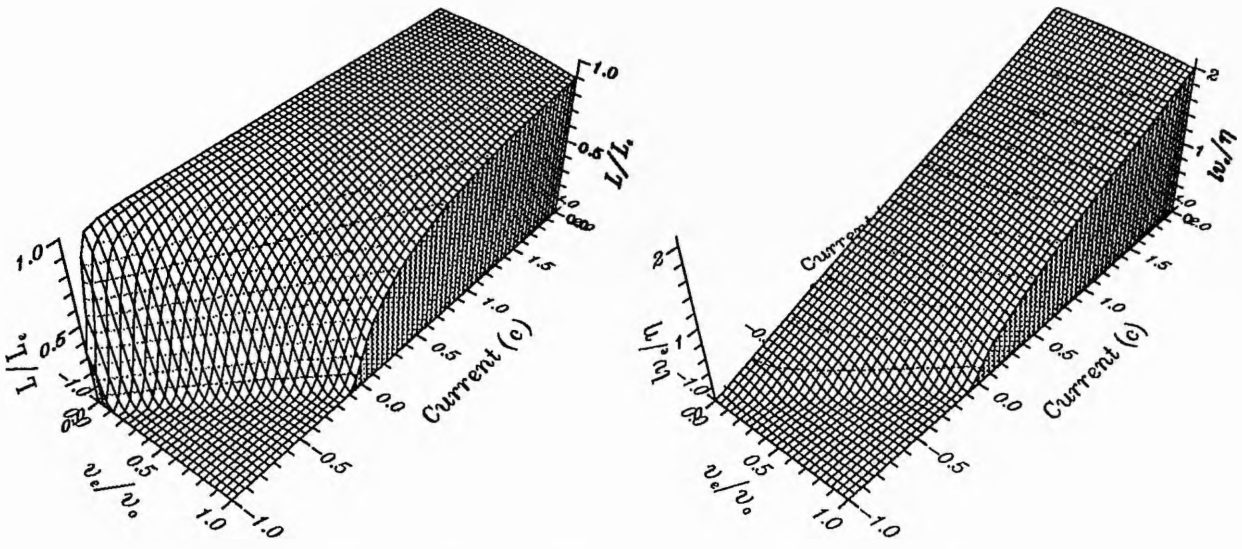

Figure 3.6: For shockless reconnection with constant outflow speed v_o, the variation of (a) current sheet length and (b) current sheet width with changes in current and inflow speed, v_e.

only weak shocks, which are a consequence of the original field configuration, and so it is a good approximation first of all to investigate the shockless model again. (Also it is important to see whether the introduction of pressure gradients has the effect of weakening or strengthening the shocks as the outflow boundary conditions are changed, which will be carried out in the next section.) Plots of the field and flow are shown for different values of L and c in Figures 3.2 - 3.5.

Numerically, the integration to find the stream function Ψ is carried out along field lines, starting with a field line at the top left-hand corner (A) of the box in Figure 3.1 and evaluating (3.34) using a trapezoidal method. Each field line is followed until it leaves the numerical box at the top boundary, AB. Repeating this process, successively smaller, equally spaced values of A are chosen so that integration is carried out along field lines which start on the y-axis closer and closer to the origin, O. When O is reached, integration is carried out along field lines starting from the x-axis below the separatrix following each line beyond the right-hand boundary, BC. Again smaller and smaller values of A are chosen until the bottom right-hand corner (C) is reached where the flux function, A, has its minimum value. The data are then interpolated onto a regular 100 × 100 grid. The interpolation is only second-order accurate: hence the choice of the trapezoidal method rather than a more precise integration method.

To consider the downstream region the outflow conditions on field, B_o, and flow, v_o, are examined. The outflow field strength (B_o) is given in terms of the external field strength as

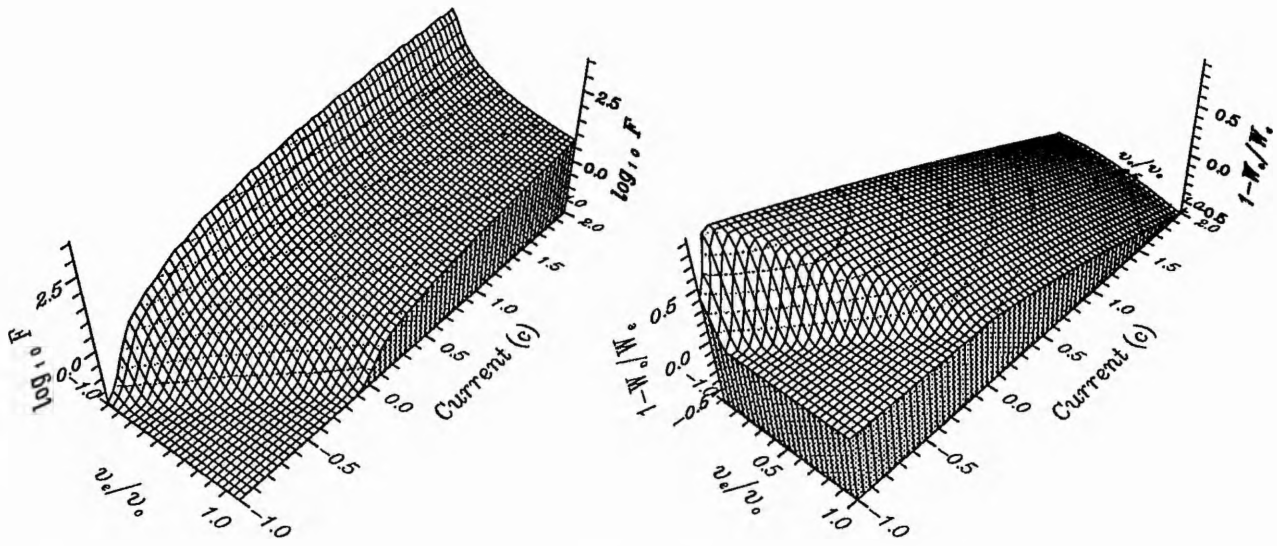

Figure 3.7: For shockless reconnection with constant outflow speed v_o, the variation of (a) the fraction f ($F = fR_{me}v_o^2/v_{Ae}^2$) of plasma not escaping along the separatrix jet and (b) the magnetic energy conversion rate with changes in current and inflow speed, v_e.

$$\frac{B_0}{B_e} = \frac{(L_e^2/L^2 - 1)^{\frac{1}{2}}(1+c)}{(L_e^2/L^2 + 1)^{\frac{1}{2}}}, \tag{3.38}$$

by evaluating (3.27) at C. Similarly, the outflow speed follows from $v_o B_o = v_e B_e$ as

$$\frac{v_0}{v_e} = \frac{(L_e^2/L^2 + 1)^{\frac{1}{2}}}{(L_e^2/L^2 - 1)^{\frac{1}{2}}(1+c)}, \tag{3.39}$$

The basic reconnection process should involve some of the incoming magnetic energy being converted into kinetic energy. To try and ensure this it is desirable for the outflow speed to be greater than the inflow speed. If this is so (3.39) implies that

$$c < (L_e^2/L^2 + 1)^{\frac{1}{2}}/(L_e^2/L^2 - 1)^{\frac{1}{2}} - 1, \tag{3.40}$$

so that, with (3.29), there is both an upper and lower bound on c. As $L \rightarrow 0$ the upper bound tends to 0, but as $L \rightarrow L_e$ it tends to ∞. By substituting for B_i/B_e equation (3.37) becomes

$$f\frac{L}{L_e} = \frac{2}{\pi R_{me} M_e^2} \frac{(1+c)^3}{(L_e^2/L^2 + 1)^{\frac{3}{2}}}. \tag{3.41}$$

In the potential case (c=0), Priest and Lee found for $f = 1$ (when all the plasma goes into the downstream region) that the maximum reconnection rate, M_e^*, is

$$M_e^{*2} = \frac{1}{\pi\sqrt{2}R_{me}}.$$

The question now is: *in general* how does the parameter c affect the type and rate of reconnection expected? Priest and Forbes (1986) found different regimes for their parameter b and these regimes are also evident in the present model. For $c < 0$, there is a slow compression, where the pressure always increases and the magnetic field decreases on approaching the current sheet. For $0 < c < (L_e^2/L^2+1)^{\frac{1}{2}} - 1$ the field weakens as one moves towards the diffusion region and there is a fast-mode expansion, but for $c > (L_e^2/L^2+1)^{\frac{1}{2}} - 1$ there is a slow-mode expansion with the field strengthening. (If the inequality (3.40) were adhered to, it would imply, however, that the slow expansion only occurs if $L/L_e > 1/\sqrt{2}$.) These classifications are used to investigate the reconnection rate.

If we have a fixed value for the outflow speed, v_0, and allow v_e to change, then we can see the way in which the current sheet length varies as the inflow speed and the current change. By rearranging (3.39) one obtains

$$\frac{L}{L_e} = \left(\frac{(1+c)^2 - V^2}{(1+c)^2 + V^2}\right)^{\frac{1}{2}}, \tag{3.42}$$

where $V = v_e/v_o$. Also the width of the current sheet follows from (3.36), (3.42) and (3.28), using $v_i B_i = v_e B_e$ as

$$\ell = \frac{\eta}{\sqrt{2}v_e}\left((1+c)^2 - V^2\right)^{\frac{1}{2}}. \tag{3.43}$$

These two relations are plotted in Figure 3.6. For $c > 0$ (the expansive regime) we see that both the length and width of the current sheet increase with c and that, as v_e goes from 0 to v_o, L goes from L_e to $L_e(1-2/((1+c)^2+1))^{1/2}$, whilst the current sheet width reduces from $\eta(1+c)/\sqrt{2}v_e$ to $\eta(c^2+2c)^{\frac{1}{2}}/\sqrt{2}v_o$. For the compressive regime, $c < 0$, both the length and width go to zero when v_e goes to $v_o(1+c)$, so the region where $v_e/v_o > (1+c)$ is invalid in this model (see also Figure 3.7).

From (3.41) we find

$$fR_{me}\frac{v_o^2}{v_{Ae}^2} = \frac{\left((1+c)^2 - V^2\right)\left((1+c)^2 + V^2\right)^{\frac{1}{2}}}{\sqrt{2}\pi V^2}. \tag{3.44}$$

It is of interest to see how much, if any, of the incoming magnetic energy is converted into kinetic energy in this model. To investigate this the incoming and outgoing magnetic energy fluxes are compared. The inflow of magnetic energy, W_e, into the region is given by integrating the Poynting flux along the boundary AB, namely

$$W_e = v_e B_e \int_0^{L_e} B_x(x, L_e)dx$$

and the outflow magnetic energy, W_o, is given by integrating along the boundary BC:

$$W_o = v_e B_e \int_0^{L_e} B_y(L_e, y) dy.$$

In both integrations B_x and B_y are given by (3.27) and L by (3.42). The rate of magnetic energy conversion is given by $(W_e - W_o)/W_e$. The relationships illustrating the fraction of plasma entering the downstream region and the magnetic energy conversion rate are plotted in Figure 3.7, with F in Figure 3.7(a) equal to $fR_{me}v_o^2/v_{Ae}^2$.

We see here that the higher the inflow speed the less the plasma goes into the downstream region and the more it is forced up the separatrix jet. This corresponds to a shortening of the current sheet. For $c > 0$ (the expansive regime) there is a minimum amount of plasma always entering the downstream region, as the current sheet length, L, is always greater than zero. As $R_{me} \gg 1$, we see from (3.24) that $f \ll 1$ except when $v_e \ll v_o$, though for $c < 0$ the current sheet length falls to zero when $v_e = v_o(1 + c)$ and all the plasma goes into the downstream region as a jet, so f is small for larger values of v_e/v_o.

In the compressive regime ($c < 0$) outflowing magnetic energy is much less than incoming energy when v_e is small, but the rate of conversion falls somewhat as the inflow increases and the current sheet shortens. Plasma is seen to be greatly accelerated as a result in most of this regime and internal reconnection rates are higher. Inflow and outflow of magnetic energy become equal in the potential case when the current sheet length is zero (the potential X-point). In the expansive regime ($c > 0$), however, the outgoing magnetic energy can actually be larger than the incoming and the plasma is seen to decelerate. Eventually, when c is greater than about 1.25, the outgoing magnetic energy is always greater than the incoming energy regardless of the inflow speed. This manifests itself in large external and internal reconnection rates and longer current sheet lengths as c increases.

3.5 Reconnection with Shocks

3.5.1 Shock Relations

In the classical Petschek reconnection model there are two pairs of slow-mode shocks, one pair coming from each end of the diffusion region. Most subsequent models have incorporated shocks in

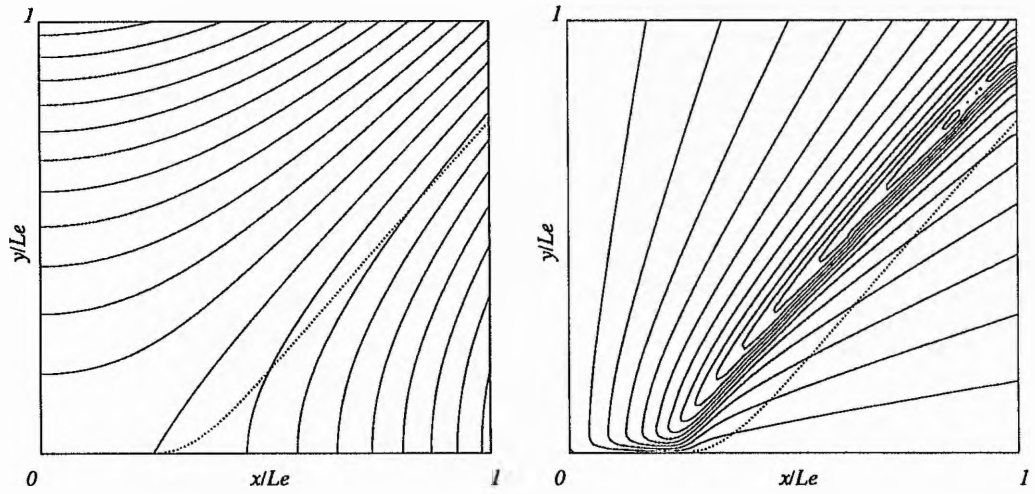

Figure 3.8: Magnetic field lines and streamlines (solid curves) with the Alfvénic discontinuity shown dotted, for the case when $L = 0.25L_e$, $c = 0$ and $v_e = 0.1v_{Ae}$.

the outflow, both of a slow- and fast-mode nature. Here the shocks are generated by disturbances at the end of the current sheet, Y, and propagate out along YH. The location of the discontinuity which supports the shock YH is given by the relation

$$v_n + v_{An} = 0, \tag{3.45}$$

where v_{An} is the normal Alfvén speed and v_n and the normal flow speed.

By non-dimensionalising the field, $\mathbf{B}$, the flow, $\mathbf{v}$ and distances with respect to the quantities B_e, the external field strength, v_{Ae}, the external Alfvén speed and L_e, the external distance, the dimensionless flux and stream functions may be written as $A' = A/L_eB_e$ and $\Psi' = \Psi/L_ev_{Ae}$. The location of the Alfvénic discontinuity is then given by the characteristic

$$\Psi' + A' = constant \tag{3.46}$$

which emanates from the end of the current sheet at $(0, L)$, the dotted line in Figure 3.8. This is exactly equivalent to (3.45). The position of this characteristic depends on the magnitude of the inflow speed, v_e, in relation to the inflow Alfvén speed, v_{Ae}, which is held fixed. The slower the flow, the closer YH is to the separatrix YS; the faster the flow, the more YH is inclined away from YS.

To investigate the effect the discontinuity might have on the downstream region, new outflow boundary conditions are applied along HC, which is downstream of the shock. Upstream, the field

and flow are still completely described by (3.6) and (3.14) so that the flux and stream functions are necessarily continuous across the shock to match the downstream with the upstream regions. Conservation of mass means that

$$v_{n1} = v_{n2}, \tag{3.47}$$

where v_{n1} and v_{n2} denote the flow speed normal to the shock downstream and upstream, respectively. Similarly, conservation of flux implies that

$$B_{n1} = B_{n2}, \tag{3.48}$$

with suffixes as before. Electric field is also conserved ($E = -v_e B_e$) and so

$$v_{x2}B_{y2} - v_{y2}B_{x2} = v_{x1}B_{y1} - v_{y1}B_{x1}. \tag{3.49}$$

The fourth condition is that the total pressure is conserved across the shock.

$$p_2 + \frac{B_2^2}{2\mu} = p_1 + \frac{B_1^2}{2\mu}, \tag{3.50}$$

so that the total pressure is equal at each point along the shock.

We now have four conditions on the five downstream variables $\mathbf{B_1}$, $\mathbf{v_1}$ and p_1, and therefore according to section 2 we are able to apply one boundary condition at the outflow boundary.

3.5.2 Numerical Solution of Downstream Region

In the downstream region (3.11) and (3.12) are solved subject to the shock relations and an outflow boundary condition on HC together with symmetry conditions on the $x-$axis. The electric field equation (3.11) may be written in terms of the flux function, A, as

$$E = -v_e B_e = (\mathbf{v}.\nabla)A. \tag{3.51}$$

Taking the curl of the momentum equation (3.12) results in

$$\rho(\mathbf{v}.\nabla)\omega = (\mathbf{B}.\nabla)j, \tag{3.52}$$

where $\omega = -\nabla^2\Psi$ is the vorticity and $j = -\nabla^2 A/\mu$ is the current density.

Here we consider a downstream region in which (3.51) and (3.52) are solved numerically by imposing a new boundary condition on HC and relaxing the old downstream quantities to find the new ones using a time-dependent code with small diffusion terms, namely

$$\frac{\partial A}{\partial t} = -\mathbf{v}.\nabla A - v_e B_e + \tilde{\eta}\nabla^2 A \tag{3.53}$$

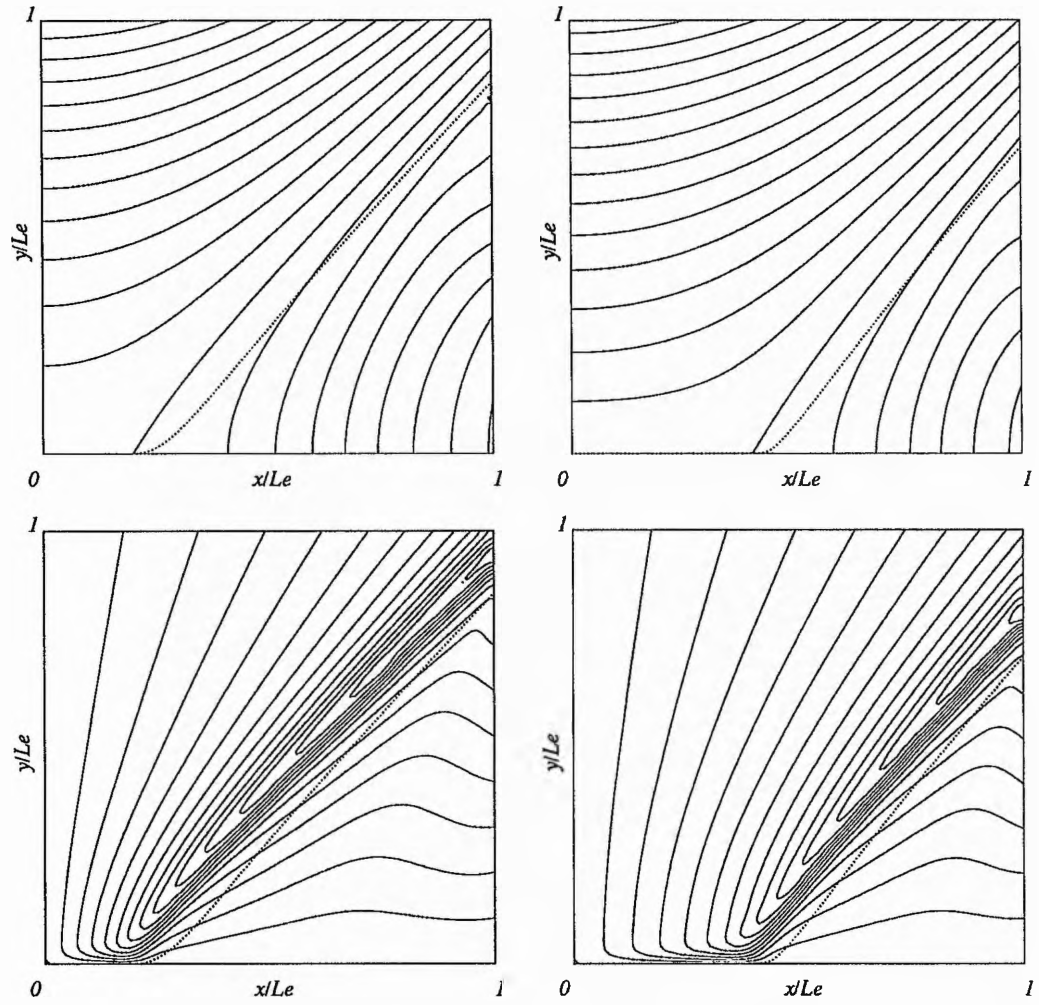

Figure 3.9: Magnetic field lines and streamlines when $M_e = 0.05$ for reconnection with shocks in the potential case $c = 0$ for $L = 0.2L_e, 0.4L_e$.

$$\rho\frac{\partial\omega}{\partial t} = -\rho\mathbf{v}.\nabla\omega + \mathbf{B}.\nabla j + \rho\tilde{\nu}\nabla^2\Psi, \tag{3.54}$$

where small values of the diffusivity, $\tilde{\eta}$, and viscosity, $\tilde{\nu}$, are included purely to try and establish a steady-state in as few Alfvén times as possible and not overshoot the required state. These values are included purely for numerical reasons and are distinct from the much smaller physical diffusivities which determine the dimensions of the current sheet. Equations (3.53) and (3.54) ensure that regions where flow dominates or there is a reversed current spike, for instance, are treated self-consistently.

The $-v_e B_e$ term on the right-hand side of (3.53) updates the flux function on the shock boundary as each successive field line passes through it. In the Priest and Lee paper there was an error in that the value of A was *not* updated at the shock boundary so that the downstream solution (e.g.

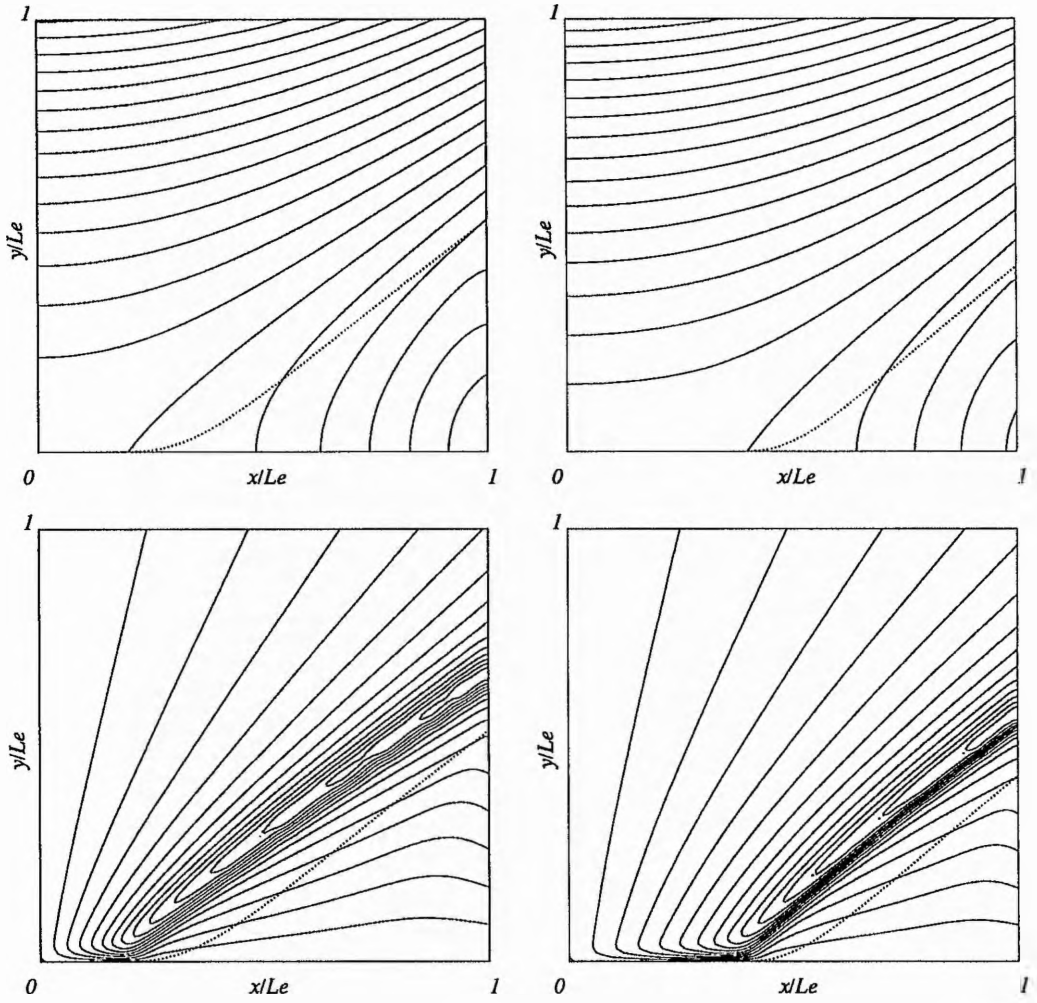

Figure 3.10: Magnetic field lines and streamlines when $M_e = 0.05$ for reconnection with shocks when $c = -0.5$ for $L = 0.2L_e, 0.4L_e$.

Figure 10 of Priest and Lee) is incorrect.

To implement the code, all equations are written in terms of the four quantities A', Ψ', j' and ω', which are the dimensionless versions of A, Ψ, j and ω. A' and Ψ' are given above and j' and ω' are similarly created by non-dimensionalising with respect to B_e, v_{Ae} and L_e. Time is also non-dimensionalised with respect to the external Alfvén time, $\tau_{Ae} = L_e/v_{Ae}$. The whole reconnection region becomes a 1×1 numerical box with the code solving downstream of the $\Psi' + A' = 0$ contour. For convenience, the prime superscript will be omitted in the remainder of this section and all quantities assumed to be dimensionless.

The boundary conditions imposed along the outflow boundary ($x = 1$) are that $\Psi(1, y)$ is a linear function of y to give a uniform outflow, whilst the derivatives $\partial\omega/\partial x$ and $\partial^2 A/\partial x^2$ are both zero. Along $y = 0$ symmetry conditions are imposed: $\Psi = 0$, $\omega = 0$ and $\partial A/\partial y = 0$. Along the shock

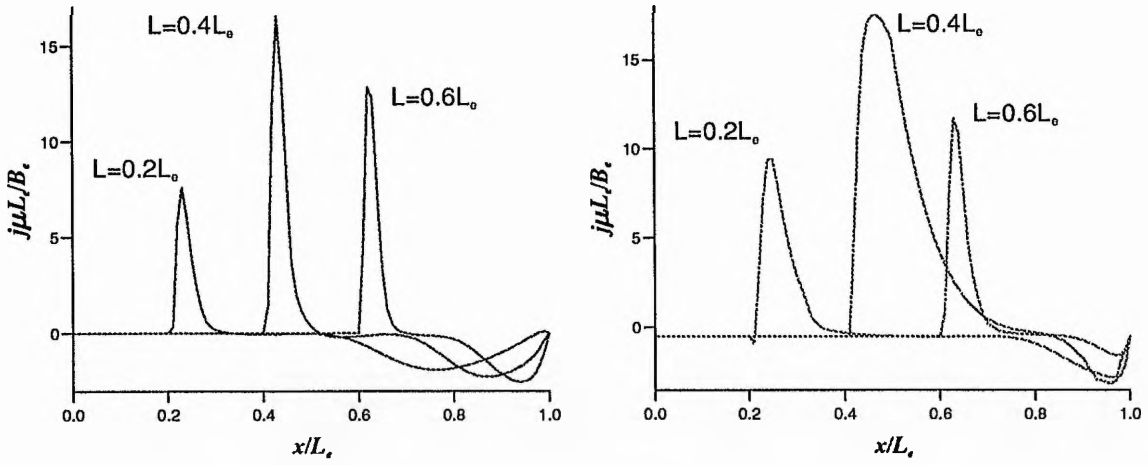

Figure 3.11: Current spikes on the x-axis for $c = 0$ and $c = -0.5$ for three different current sheet lengths

front YH, Ψ and A are given by continuity whilst at the $n+1$ time step the vorticity is given by the Laplacian of Ψ at the n^{th} time step: $\omega^{n+1} = -\nabla^2\Psi^n$. Initially the given quantities are those from the analytical shockless solution, whilst along the outflow Ψ is changed to the imposed value over 50 time steps. The code is run for several Alfvén times to allow information about the new boundary conditions to propagate throughout the whole of the downstream region. The usual CFL condition is applied to guarantee time stability of the code. Forward differencing is used for time derivatives and centred-differencing is used for spatial terms. The full set of dimensionless equations used in the code is

$$\frac{\partial A}{\partial t} = -\frac{\partial \Psi}{\partial y}\frac{\partial A}{\partial x} + \frac{\partial \Psi}{\partial x}\frac{\partial A}{\partial y} - M_e + R_{me}^{-1}\nabla^2 A \tag{3.55}$$

$$\frac{\partial \omega}{\partial t} = -\frac{\partial \Psi}{\partial y}\frac{\partial \omega}{\partial x} + \frac{\partial \Psi}{\partial x}\frac{\partial \omega}{\partial y} + \frac{\partial A}{\partial y}\frac{\partial j}{\partial x} - \frac{\partial A}{\partial x}\frac{\partial j}{\partial y} + \frac{M_e}{R_e}\nabla^2\omega \tag{3.56}$$

$$\nabla^2\Psi = -\omega \tag{3.57}$$

$$j = -\nabla^2 A \tag{3.58}$$

with the two-dimensional Laplacian operator $\nabla^2 = \partial^2/\partial x^2 + \partial^2/\partial y^2$. These equations form a closed system with (3.57) solving for Ψ away from the outflow boundary using a simple relaxation method. M_e is the external Alfvén Mach number, $R_{me} = v_{Ae}L_e/\tilde{\eta}$ the external magnetic Reynolds number and $R_e = v_e L_e/\tilde{\nu}$ the viscous Reynolds number. The constants μ and ρ are absorbed into the dimensionless variables. The code terminates once the time derivatives become smaller than a very small tolerance level. Finally, the quantities are re-dimensionalised so their relative sizes can be compared. The results of several simulations are shown in Figures 3.9 and 3.10.

The streamlines adjust quite significantly to match the new outflow boundary conditions, some

bending down sharply as the boundary is approached. The field responds accordingly near the outflow with the field in the vicinity of C weakening as the flow speed increases there and conversely strengthening close to H where the flow speed decreases. Nearer the end of the current sheet the field and flow are less affected. The most significant feature on the x-axis is the very sharp current spike at the end of the current sheet. This is thought to result from the need for the plasma exiting the current sheet at the local Alfvén speed to decelerate in order to match with the imposed outflow boundary speed (Jardine and Priest (1988c)). Also evident is a more diffuse current 'bump' in the opposite direction near the outflow boundary associated with a small acceleration of the plasma as the streamlines bend down. The current spike is characteristic of many numerical simulations of reconnection (e.g. Biskamp, 1986). Current spikes for different current sheet lengths and two constant current values are plotted in Figure 3.11.

3.6 Discussion

3.6.1 Reconnection Rate and Scaling

As reconnection is one of the fundamental processes of MHD, one aim behind new models is to try and obtain a reconnection rate which is in agreement with the observed values in astrophysical plasmas. The models presented here depend on a parameter, c, such that $c < 0$ gives a family of compressive regimes, $c = 0$ is the potential solution with uniform pressure and $c > 0$ corresponds to a family of expansive regimes. We can deduce the maximum reconnection rate associated with each regime, seeing how it varies with c and R_{me}, the external magnetic Reynolds number.

In general, flux conservation implies that the ratio of the field strength at the diffusion region inflow to the external value is

$$\frac{B_i}{B_e} = \left(\frac{M_e}{M_i}\right)^{\frac{1}{2}}, \tag{3.58}$$

where M_e and M_i are the external and inflow Alfvén Mach numbers. M_e is a measure of the reconnection rate. Furthermore, the Sweet-Parker relations for the central diffusion region imply that the length and width are

$$\frac{L}{L_e} = \frac{1}{R_{me} M_e^{\frac{1}{2}} M_i^{\frac{3}{2}}} \tag{3.59}$$

and

$$\frac{\ell}{L_e} = \frac{1}{R_{me} M_e^{\frac{1}{2}} M_i^{\frac{1}{2}}} \tag{3.60}$$

where L_e is the external scale length. These relations hold for all steady nonlinear reconnection models and the relation $M_i(M_e, R_{me})$ for the inflow Mach number follows from the details of the external region. In our case the external solution simply gives the additional relation

$$\frac{B_i}{B_e} = \frac{(1+c)}{(L_e^2/L^2+1)^{\frac{1}{2}}}. \tag{3.61}$$

When (3.58) and (3.59) are used to substitute for B_i and L, this reduces to

$$R_{me}^2 M_i^3 M_e^2 + M_e - (1+c)^2 M_i = 0. \tag{3.62}$$

After solving this for $M_i(M_e, R_{me})$, (3.59) and (3.60) determine the scaling laws for $\ell(M_e, R_{me})$ and $L(M_e, R_{me})$. The solution of (3.62) is

$$M_e = \frac{-1 + \left[1 + 4R_{me}^2 M_i^4 (1+c)^2\right]^{\frac{1}{2}}}{2R_{me}^2 M_i^3}, \tag{3.63}$$

and is plotted in Figure 3.12 for different values of R_{me} and c. When $M_i \ll R_{me}^{-1/2}$, $M_e \approx (1+c)^2 M_i$, whereas, when $M_i \gg R_{me}^{-1/2}$, $M_e \approx (1+c)/(M_i R_{me})$. There is a maximum reconnection rate, $M_e^* = (2/3\sqrt{3})^{1/2}(1+c)^{3/2}/R_{me}^{1/2}$ when $dM_e/dM_i = 0$, however this is unphysical in the sense that $L = \sqrt{2}L_e$ at M_e^*. The maximum *allowable* rate, M_e^{**}, is, therefore, produced when $L = L_e$ and is given by

$$M_e^{**} = \frac{(1+c)^{\frac{3}{2}}}{(2\sqrt{2}R_{me})^{\frac{1}{2}}}, \tag{3.64}$$

which is slightly less than M_e^* and is shown in Figure 3.13.

When $M_i \gg R_{me}^{-1/2}$, $L < L_e$ and the resulting scalings for the diffusion region dimensions are

$$\frac{L}{L_e} \approx \frac{R_{me}^{\frac{1}{2}} M_e}{(1+c)^{\frac{3}{2}}} \tag{3.65}$$

and

$$\frac{\ell}{L_e} \approx \frac{1}{R_{me}^{\frac{1}{2}}(1+c)^{\frac{1}{2}}}, \tag{3.66}$$

so that the sheet length increases with both M_e and R_{me}, as seen in Biskamp's experiments. At the maximum rate these scalings are $L/L_e = 1$ and $\ell/L_e \approx R_{me}^{-1/2}(1+c)^{-1/2}$.

In the past it has been assumed that a ${R_{me}}^{-1/2}$ scaling of the maximum reconnection rate implies that fast reconnection is not possible. However, it can be seen from (3.64) that this is not the case. Furthermore, Priest and Forbes (1992) have shown that reasonable agreement with numerical experiments on reconnection can be obtained by allowing c to vary with M_e and R_{me} in such a

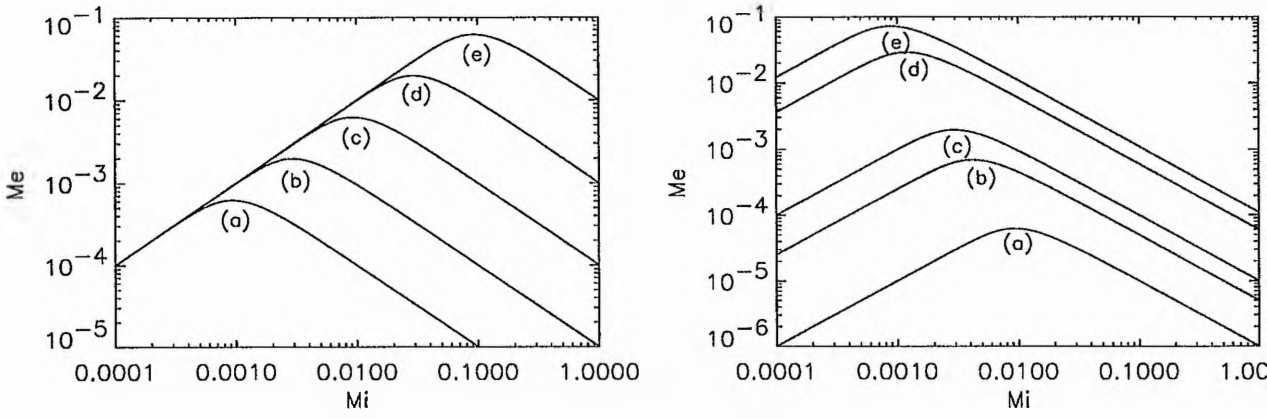

Figure 3.12: The rate of reconnection, M_e as a function of internal Alfvén Mach number, M_i for (i) $c = 0$ with R_{me} = (a) 10^6, (b) 10^5, (c) 10^4, (d) 10^3, (e) 10^2 and (ii) $R_{me} = 10^5$ with c = (a) -0.9, (b) -0.5, (c) 0, (d) 5, (e) 10.

way as to satisfy the particular boundary conditions that were adopted by the experimenters. Fast reconnection is defined to have a rate greater than the pure Sweet-Parker rate, $M_e = {R_{me}}^{-1/2}$, and therefore all the models with $c > 0$ have maximum rates which are fast. If one is restricted to potential reconnection with $c = 0$ (e.g. by insisting on negligible pressure gradients), the nonuniform analogy of Petschek reconnection, then one can only have a reconnection rate greater than a given value M_e if $R_{me} < M_e^{-2}$. If instead we allow $c > 0$ in the present model so that strong plasma pressure gradients and large (> 1) plasma β are present, reconnection faster than M_e is possible if $R_{me} < (1 + c)^3/M_e^2$. Thus rates of 0.1, for instance, at magnetic Reynolds numbers of, say, 10^5 are possible if $c > 10$ (Figure 3.12 (ii)). In other words, we conclude that fast flux pile-up reconnection at any given magnetic Reynolds number is possible by taking c sufficiently large.

3.6.2 Comments and Comparisons

With the successful marriage of analytical and numerical models, further understanding of the whole process of two-dimensional magnetic reconnection can be achieved. Here, we have sought to highlight the importance of pressure gradients in creating different reconnection regimes and also emphasise the crucial role that boundary conditions play in determining these regimes. The combination of analytical and numerical models in this chapter helps understanding of and comparison with previous models of both types. The two seminal papers, those of Priest and Forbes (1986) and Priest and Lee (1990) (from which the basic model is drawn) can be viewed in this light.

Compressive and expansive reconnection regimes previously found in the Priest-Forbes *Unified*

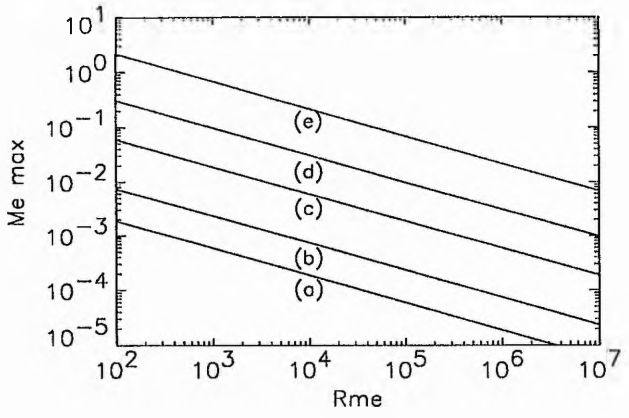

Figure 3.13: The maximum rate of reconnection, M_e^{**}, as a function of the external magnetic Reynolds number R_{me} for different values of current c: (a) $c = -0.9$, (b) $c = -0.5$, (c) $c = 0$, (d) $c = 2$, (e) $c = 10$.

Almost-Uniform model are also present in the *Nonuniform* model and we reproduce and extend the Priest-Lee results using, as they did, an analysis of the whole field and not relying on linearisation. Also of interest is the current spike observed in the numerical part of the analysis which was first seen in the numerical models of Biskamp(1986) and Lee and Fu (1986). These are again evident here and of particular interest in the non-potential case when the plasma exits the downstream boundary faster (compressive) or slower (expansive) than in the potential case, so the deceleration of the plasma changes significantly as c changes, and hence the size of the current spike. The current 'bump' seen in this model may also be significant in the physics of the outflow boundary conditions. Unlike the Priest-Lee model, we do not see the large kink in the magnetic field immediately downstream of the shock and this has been explained, but in other respects the numerical simulations are similar.

Chapter 4

Nonuniform Reconnection Models with Non-Singular Separatrix Jets

4.1 Chapter Summary

This chapter examines a different extension to the Priest-Lee *Nonuniform Reconnection Model* . By adding a uniform field in the x-direction, a cusp-point replaces the Y-point at the end of the current sheet, so that the flow is no longer singular everywhere on the separatrix. Section 1 briefly explains the singularity, whilst Section 2 presents an analytical non-singular solution about a double-cusp point. In Section 3, the adaptation of the Priest-Lee model is explored in detail, with the MHD characteristics and the diffusion region being analysed. The analytical model has a discontinuous x-component in the field on the x-axis, so that solutions which remove this below the separatrix must be derived numerically. These solutions are presented in Section 4. Section 5 considers the reconnection rate, which is determined by inflow conditions, and Section 6 draws conclusions.

4.2 Introduction

Most of the classical reconnection models have studied perturbations about a potential field (Petschek, 1964; Yeh and Axford, 1970, Soward and Priest, 1977; Priest and Forbes, 1986) with standing slow-mode shocks separating the inflow from the outflow. More recently, with the advent of more sophisticated numerical models, attention has switched to nonuniform, and in some cases non-potential, models (Biskamp, 1986; Forbes and Priest, 1986; Lee and Fu, 1986). These models have revealed new features including current spikes in the outflow and strong jets of plasma emitted away from the diffusion region along the separatrices. The jetting phenomenon can also be studied analyti-

cally (Soward and Priest, 1977; Priest and Lee, 1990) by investigating the solution to the flow as the separatrix is approached. A separatrix is a field line which passes through the neutral point. Constant values of the stream function delineate the streamlines, but it is found that the value of the stream function is discontinuous across the separatrix (Soward and Priest, 1977). In the case of a potential X-point the whole flow can be described analytically and becomes singular along the entire separatrix.

Priest and Lee (1990) have made substantial progress in setting up a *Nonuniform Reconnection Model* with potential inflows; they contain finite length current sheets and separatrix jets, but the flow becomes singular at the separatrices. Chapter 3 extends this work by including non-potential inflows, but separatrix jets are still present. Although the jet is an important feature, the presence of the singularity is unphysical. In this paper we seek to address the problem by considering a model with a modified neutral point at the end of the diffusion region so that the neutral point changes from being an X- or Y-point to being cusp-like in nature so that the field tends to zero inside the cusp but remains non-zero outside (see Chapter 2). This removes the singularity in the flow when the separatrix is approached from the inflow region. In order to model the cusp-point, a uniform x-field is added to the previous field containing an X-point or Y-point. An equal and opposite field is imposed in the lower half-plane leading to a discontinuous x-component of the field along the x-axis. This discontinuity is removed by solving the full MHD equations numerically below the separatrix.

4.3 Analytical X-Point and Double-Cusp Solutions

4.3.1 Incompressible Flow about a Potential X-Point

In considering the effects on the flow near the separatrix in a reconnection model, it is useful to look first at the solution to the incompressible flow around a potential X-point, which may be treated analytically. This illustrates the nature of the discontinuity along the separatrix and provides a comparison with a non-singular result which is also obtained for a double cusp-point. Starting with the potential X-point background field described by

$$\mathbf{B} = \frac{B_e}{L_e}(y\hat{\mathbf{x}} + x\hat{\mathbf{y}}), \tag{4.1}$$

where B_e is the field strength at $(0, L_e)$, we can impose the usual constraint on the field, namely

$$\nabla \cdot \mathbf{B} = 0, \tag{4.2}$$

to construct a flux function $A = A(x, y)\hat{\mathbf{z}}$ such that

$$\nabla \times \mathbf{A} = \mathbf{B}, \tag{4.3}$$

where constant values of A trace out field lines. For the potential X-point, the flux function is given by

$$A = \frac{B_e}{2L_e}(y^2 - x^2). \tag{4.4}$$

If the magnetic field, $\mathbf{B}(\mathrm{x}, \mathrm{y})$ is in a steady state, the electric field is curl-free, and so uniform, having the form

$$\mathbf{E} = E\hat{\mathbf{z}}. \tag{4.5}$$

The field is potential and thus Ohm's Law reduces to

$$\mathbf{E} + \mathbf{v} \times \mathbf{B} = \mathbf{0}, \tag{4.6}$$

where $\mathbf{v}$ describes the flow around the X-point. In most astrophysical cases, the flow speed $v \ll v_A$, so that the continuity equation reduces to

$$\nabla \cdot \mathbf{v} = \mathbf{0}, \tag{4.7}$$

with density, ρ, uniform. This is satisfied identically by writing the flow in terms of a stream function $\Psi(x, y)\hat{\mathbf{z}}$

$$\nabla \times \Psi = \mathbf{v} \tag{4.8}$$

Given (4.6) and (4.8) and a prescribed magnetic field, it is then possible to determine Ψ and therefore the flow fully.

To do so, (4.6) is recast as

$$\mathbf{B} \cdot \nabla \Psi = v_e B_e, \tag{4.9}$$

where v_e is the external flow speed. This in turn can be integrated to give

$$\Psi = v_e B_e \int \frac{ds}{B} = v_e B_e \int \frac{dx}{B_x}, \tag{4.10}$$

where ds is measured along each field line. Symmetry of the flow about the y-axis means that there is a streamline along it. We can arbitrarily give this streamline a value, say $\Psi = 0$, and use it as a boundary condition to integrate the projection of the field, dx/B_x, above the separatrix. Symmetry about $y = x$ (the separatrix) reveals that the stream function generated by integrating from the streamline, $\Psi = 0$, on the x-axis *below* the separatrix is identical to the function found above the separatrix, so that in the case of a potential X-point, the resulting stream function, $\Psi(x, y)$, is given by

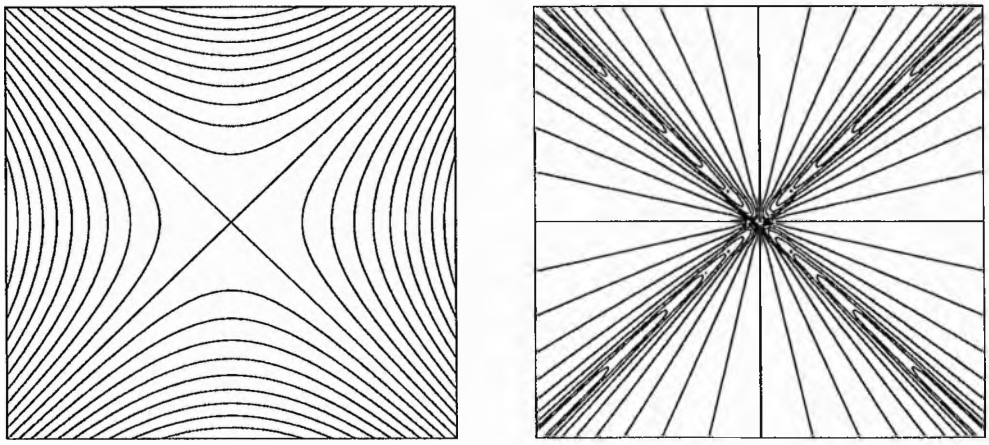

Figure 4.1: Potential X-point and corresponding incompressible flow showing jetting along the separatrices.

$$\Psi = \frac{v_e L_e}{2} \log_e \left| \frac{x+y}{x-y} \right|. \tag{4.11}$$

Equation (4.8) then yields velocity components

$$v_x = v_e L_e \frac{x}{(x^2-y^2)}, \quad v_y = v_e L_e \frac{y}{(x^2-y^2)}. \tag{4.12}$$

Clearly, there is a singularity in the flow and the stream function along the separatrix, $y = x$. This manifests itself as a strong jet of plasma in the vicinity of the separatrix. In reality non-ideal affects, such as diffusion, could take over and resolve the singularity but its presence is undesirable.

4.3.2 Non-Singular Stream Function about a Double-Cusp

There is a second way of removing the singularity, however. Instead of considering a potential X-point, a *modified* model can be constructed with an additional piecewise uniform B_x field. This field is positive in the upper half-plane, but equal and opposite in the lower half-plane. It transforms the neutral point from an X-point to a double cusp-point with the separatrices touching the x-axis. The flux function which describes this configuration is given by

$$A = (1+k)^{-1} \left[\frac{B_e}{2L_e}(y^2 - x^2) + B_e k|y| \right], \tag{4.13}$$

where k is a dimensionless positive constant and the factor $(1+k)^{-1}$ ensures that $B_x = B_e$ at $(0, L_e)$. (If k were to be negative then the separatrix would form a double cusp-point with the cusp touching

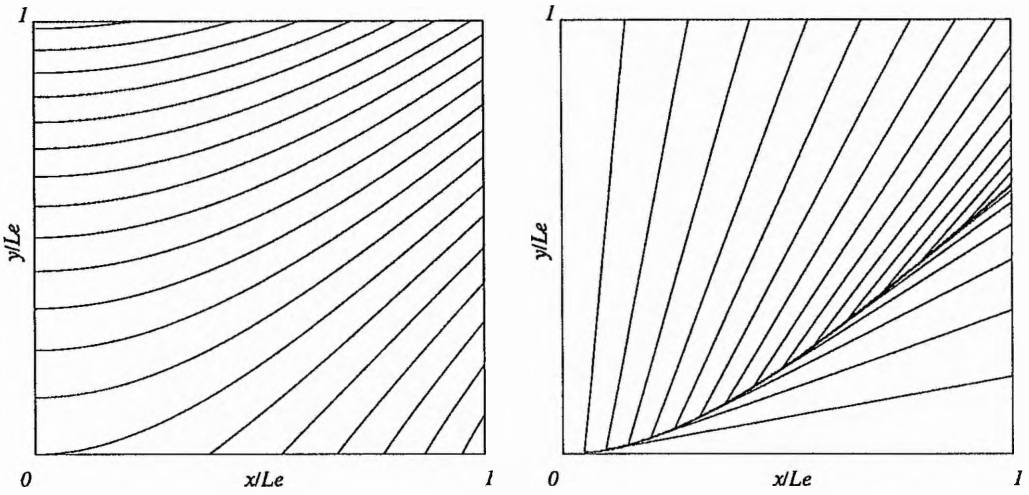

Figure 4.2: First quadrant of a double-cusp with corresponding analytical incompressible flow when $k = 0.5$.

the y-axis and not the x-axis.) The equation of the separatrix is simply given by the rectangular hyperbola

$$(y + kL_e)^2 - x^2 = k^2 L_e^2, \tag{4.14}$$

which marks the dividing line between the two solutions given below for the stream function.

When $y > 0$ the resulting field has components

$$B_x = \frac{1}{(1+k)} \frac{B_e}{L_e} (y + kL_e), \quad B_y = \frac{1}{(1+k)} \frac{B_e}{L_e} x. \tag{4.15}$$

This describes the field *above* the separatrix. The crucial difference between the X-point and double-cusp models is that there is a non-vanishing field component as the neutral point is approached from above. This will determine a non-singular flow above the separatrix, as we shall see.

Above and including the separatrix, the stream function can be calculated as before to give

$$\Psi = (1+k) \frac{v_e L_e}{2} \log_e \left| \frac{x + (y + kL_e)}{x - (y + kL_e)} \right|, \tag{4.16}$$

which has velocity components

$$v_x = v_e L_e (1+k) \frac{x}{(x^2 - (y + kL_e)^2)}, \quad v_y = v_e L_e (1+k) \frac{y + kL_e}{(x^2 - (y + kL_e)^2)}. \tag{4.17}$$

As the separatrix is approached from above, the stream function is non-singular and behaves like $\sinh^{-1}\xi$, where $\xi = x_s/(kL_e)$ and x_s is the x-coordinate of a point on the separatrix. The previous singular X-point result can be retrieved by setting $k = 0$.

Below the separatrix, the field is initially described by (4.15), whilst the initial stream function is found by integrating along the field lines from the x-axis with the same boundary condition as before, namely that $\Psi = 0$. This time the projection of the field in the y-direction is integrated so (4.10) becomes

$$\Psi = v_e B_e \int \frac{dy}{B_y}, \tag{4.18}$$

with integration again being along each field line. The stream function generated by this integral is different from (4.16), which would give a singularity on the line $y = x - kL_e$. However, the imposition of the boundary condition on the x-axis removes the singularity and the stream function below the separatrix becomes

$$\Psi = v_e L_e (1+k) \log_e \left| \frac{x + y + kL_e}{kL_e + \sqrt{(x^2 - y^2 - 2kL_e y)}} \right|. \tag{4.19}$$

Equations (4.16) and (4.19) imply that the stream function is continuous across the separatrix and remains finite along its entire length, so that there is no jump in the stream function corresponding to a separatrix jet. This is in contrast to the X-point solution which has a singular stream function along its separatrix. The velocity components are

$$v_x = v_e L_e (1+k) \left[\frac{y + kL_e}{kL_e S + S^2} + \frac{1}{R} \right], \quad v_y = v_e L_e (1+k) \left[\frac{x}{kL_e S + S^2} - \frac{1}{R} \right], \tag{4.20}$$

where $R = x + y + kL_e$ and $S = \sqrt{(x^2 - y^2 - 2kL_e y)}$. The streamlines are tangent to the separatrix, so that the flow is *aligned* with the field as the separatrix is approached from below. Clearly a field-aligned flow will give $\mathbf{v} \times \mathbf{B} = 0$ for finite velocity and field components. However, we see from (4.20) that the velocity components are both singular as the separatrix is approached from below since $S = 0$. The analytical flux and stream functions are plotted in Figure 4.2 and the full numerical solutions for two different values of k with the B_x discontinuity removed and numerical smoothing performed on the downstream side of the separatrix are shown in Figure 4.3.

The ratio of flow components in (4.20), v_y/v_x, remains finite, however, and the flow is deflected through an angle θ_s at the separatrix given by

$$\theta_s = \cos^{-1} \left(\frac{-2x_s (x_s^2 + k^2 L_e^2)^{\frac{1}{2}}}{2x_s^2 + k^2 L_e^2} \right). \tag{4.21}$$

At the origin θ_s is imposed to be $-\pi/2$ and as x_s increases, θ_s increases toward $-\pi$ at infinity. In the locality of the downstream side of the separatrix, non-ideal effects such as resistivity will tend to remove the singularity in the flow.

The fact that a singularity remains in the flow below the separatrix can be explained by the following analysis. Previously, the field in all analytical models tends to zero at the neutral point, which usually lies at the end of the current sheet. Consequently, $\mathbf{v} \times \mathbf{B} = -\mathbf{E}$ can only be maintained

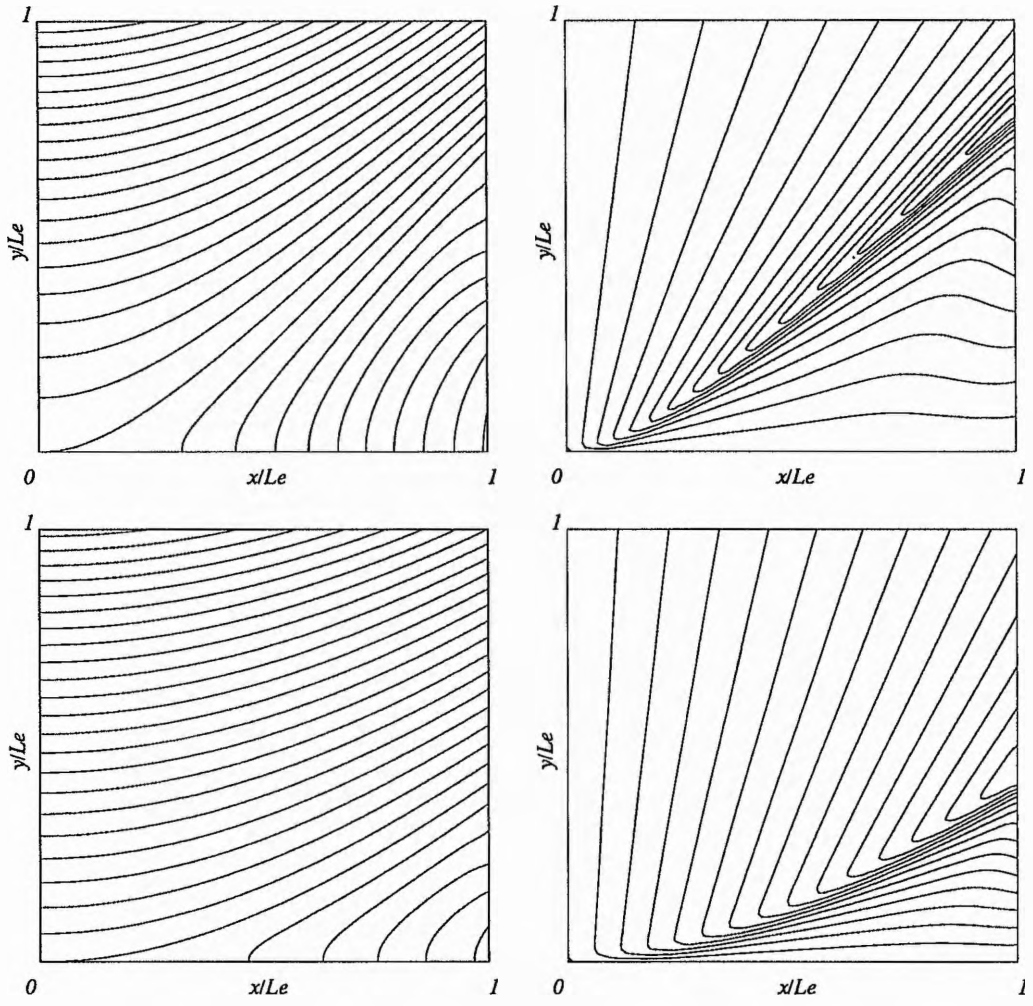

Figure 4.3: The full numerical solution for the magnetic field lines and streamlines for double-cusp models when (a) $k = 0.2$ and (b) $k = 0.5$.

if the velocity becomes singular at the neutral point. Immediately above the neutral point there is only an x-component of field so that

$$\mathbf{v} \times \mathbf{B} = -v_y B_x, \tag{4.22}$$

and v_y becomes becomes singular. Beyond the neutral point, i.e. below the separatrix, there is only a y-component of field so

$$\mathbf{v} \times \mathbf{B} = v_x B_y, \tag{4.23}$$

and v_x becomes singular at the neutral point. As a consequence of the singularities above and below the separatrix, the flow becomes aligned with the separatrix field line as it is approached from above or below. If the field and flow are aligned, $E = 0$ unless the flow becomes singular along the field line, hence the singularity along the entire separatrix.

In the analytical solution presented above, the field remains non-zero as the neutral point is

approached from above, so that (4.22) does not lead to a singularity, v_y remains finite and the flow does not align itself with the separatrix. This is also true in the *Cusp Current Sheet* configuration examined below. Below the separatrix, the y-component of the field *must* go to zero by the definition of a cusp-like neutral point in Chapter 2. Consequently, (4.23) always leads to a singularity when ideal MHD is being considered. The singularity can be resolved by allowing for a finite thickness at the end of the current sheet: imposing the classical outflow speed, namely $v_{out} = v_{Ai}$, we would, by (4.6) and (4.23), expect to have a y-component of the magnetic field given by

$$B_y = \frac{v_e B_e}{v_{Ai}}. \tag{4.24}$$

This means that both field components would be non-zero at the end of the current sheet, so there is no longer a neutral point located there but this analysis lies outside the scope of our current investigation.

Clearly the solution (4.15) is unrealistic as the x-axis is approached, since there is an infinite acceleration along the x-axis. Nevertheless, it is a useful analytical solution which sheds light on the nature of the separatrix flow and acts as a preliminary for the full numerical solutions of the next section, which removes this current sheet whilst preserving the overall structure.

4.4 Cusp Current Sheet Model

4.4.1 MHD Characteristics

Consider a potential model containing two Y-type neutral points at the ends of a current sheet. The field vanishes at the Y-points so that the flow tends to become singular locally if ideal MHD holds. The field near a Y-point has a strength proportional to the square root of the distance away from the point so that the integral (4.10) is *non*-singular, but the derivatives of the stream function (the velocity components) are. These points act as sources for discontinuities (shocks in the compressible case) coming off the ends of the current sheet. Even when a uniform B_x component is added to form cusps so that the flow becomes finite, there is still a discontinuity generated. The shocks exist physically because information cannot propagate upstream across the field lines away from the ends of the current sheet. This can be seen by looking at the MHD characteristics of the system.

If one considers the momentum equation,

$$\rho(\mathbf{v}\cdot\nabla)\mathbf{v} = -\nabla \mathrm{p} + \frac{1}{\mu}(\nabla\times\mathbf{B})\times\mathbf{B}, \tag{4.25}$$

and the electric field equation

$$\mathbf{E} + \mathbf{v}\times\mathbf{B} = \mathbf{0}, \tag{4.26}$$

then by taking the curl of (4.26) and looking at the sum and difference of these equations one can deduce that

$$(\mathbf{v}_-.\nabla)\mathbf{v}_+ = -\frac{1}{\rho}\left(\mathrm{p} + \frac{\mathrm{B}^2}{2\mu}\right) \tag{4.27}$$

and

$$(\mathbf{v}_+.\nabla)\mathbf{v}_- = -\frac{1}{\rho}\left(\mathrm{p} + \frac{\mathrm{B}^2}{2\mu}\right) \tag{4.28}$$

where $\mathbf{v}_+ = \mathbf{v} + \mathbf{v}_\mathbf{A}$, $\mathbf{v}_- = \mathbf{v} - \mathbf{v}_\mathbf{A}$ and $\mathbf{v}_\mathbf{A} = \mathbf{B}/\sqrt{\mu\rho}$ is the Alfvén velocity (Soward and Priest, 1977). If the total pressure is uniform, $(\mathbf{v}_+.\nabla)\mathbf{v}_- = (\mathbf{v}_-.\nabla)\mathbf{v}_+ = 0$ and we see that the quantity $\mathbf{v}_+$ is constant along the characteristics C_- and vice versa. If the total pressure varies, the pressure gradient acts as continuous sources for waves.

The characteristics C_+, which are the streamlines for $\mathbf{v}_+$, cannot propagate information into or out of the downstream region as the limiting characteristic coming from the end of the current sheet divides the two regions. This characteristic carries an Alfvenic discontinuity, with magnetic information unable to propagate across the field since the slow magnetoacoustic speed is zero across field lines. Only the characteristics C_-, which are the streamlines for $\mathbf{v}_-$, can cross the limiting C_+ characteristic coming off the end of the current sheet and carry information into and out of the downstream region.

If $\mathbf{v} \ll \mathbf{v}_\mathbf{A}$, which is the case for most circumstances in the solar atmosphere, the C_+ and C_- characteristics align themselves closer and closer to the field lines and the limiting C_+ characteristic tends toward the separatrix. This means, in general, that the C_- characteristics cross the discontinuity at shallower and shallower angles.

In addition, there is a mismatch in the stream function across the separatrix which can be evaluated at the end of the current sheet by a simple analysis. From (4.10), the value of the stream function at a point $(L, 0_+)$ just above the end of the current sheet is given by

$$\Psi_L = v_e B_e \int_0^L \frac{dx}{B_x(x)}, \tag{4.29}$$

with integration along the x-axis. If the density, ρ is normalised, we can see that this is simply the mass flux into the current sheet, because, by (4.26),

$$\rho v_y(x) = \frac{v_e B_e}{B_x(x)}, \tag{4.30}$$

with $v_y(x)$ being the profile of the velocity just above current sheet bringing plasma in. By contrast, the value of the stream function at a point $(L_+, 0)$ on the x-axis just beyond the end of the current sheet is *imposed* to be 0. This jump is maintained along the entire separatrix, as two field lines lying arbitrarily close, but on opposite sides of the separatrix, will cause the stream function to be increased by the same amount when the integration along them is carried out.

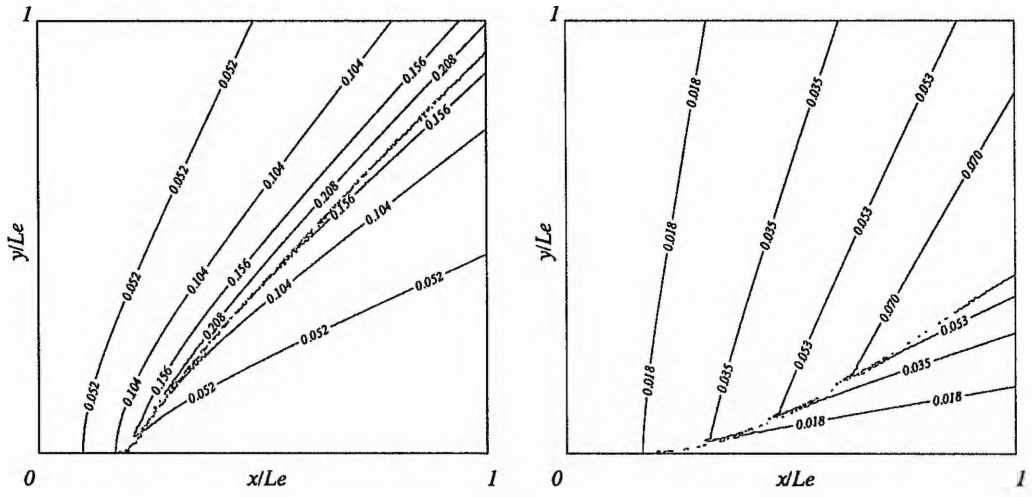

Figure 4.4: The streamlines for a Y-point and a cusp current sheet model when there is no diffusion or smoothing, with $k = 0.8$, when $L = 0.2L_e$ and $v_e = 0.1v_{Ae}$. The streamlines are seen to follow the separatrix for a distance equal to the current sheet length before joining the corresponding streamline below the separatrix.

If we consider the streamline along the y-axis, which has the value $\Psi = 0$, it must match with the streamline beyond the end of the separatrix along the x-axis by going along the current sheet, so it "jumps" a distance exactly the same length as the current sheet. Consequently, a streamline in the inflow joining the separatrix moves along it a distance exactly the same as the current sheet length before matching with the streamline with the same value below the separatrix. This can be seen in Figure 4.4 for both the Y-point and cusp-point models with the flow tending to become singular in the Y-pont model on both sides of the separatrix.

4.4.2 Basic Model

A potential field with a current sheet, which has two Y-points at the ends of the sheet, was used by Priest and Lee (1990) in their nonuniform reconnection model and is generated using complex variable theory. It is of the form

$$\frac{dA_0}{dZ} = B_y + iB_x = B_0 \left(\frac{Z^2}{L^2} - 1 \right)^{\frac{1}{2}}, \tag{4.31}$$

where $Z = x + iy$ and there is a cut in the complex plane along the real axis between $Z = \pm L$. By integrating and taking the real part, (4.31) yields a flux function

$$A_0 = -\frac{B_0}{2L} \left[xr - ys - L^2 \log \frac{\{(x+r)^2 + (y+s)^2\}^{\frac{1}{2}}}{L} \right], \tag{4.32}$$

where $r = \left[\frac{1}{2}\left((X^2+Y^2)^{\frac{1}{2}}+X\right)\right]^{\frac{1}{2}}$, $s = \left[\frac{1}{2}\left((X^2+Y^2)^{\frac{1}{2}}-X\right)\right]^{\frac{1}{2}}$, $X = x^2-y^2-L^2$ and $Y = 2xy$.

To this field we may add a flux function A_1 which generates a uniform positive B_x field when $y > 0$, namely

$$A_1 = B_e k y, \tag{4.33}$$

with k as in Section 4.3.2. The field is equal and opposite for $y < 0$ so that a cusp-point is created at the end of the current sheet and initially there is a jump in B_x across the x-axis.

Even more generally, pressure gradients can be introduced by imposing a constant-current field (see Chapter 3) generated by the flux function

$$A_2 = -\frac{B_e}{2L_e} c y^2, \tag{4.34}$$

where c is a dimensionless constant which can be positive or negative. Hence, the total flux function is $A = A_0 + A_1 + A_2$ and the total field is given by

$$B_x = B_0 \frac{s}{L} + B_e k - B_e \frac{cy}{L_e}, \quad B_y = B_0 \frac{r}{L}, \tag{4.35}$$

with r and s as above.

The field strength at the external point $(0, L_e)$ is fixed at B_e, so, by evaluating (4.35) at this point we see that B_0 is related to the fixed external field strength by

$$B_0 = \frac{(1+c-k)}{(L_e^2/L^2+1)^{\frac{1}{2}}} B_e, \tag{4.36}$$

with the ratio B_0/L in (4.32) tending to $B_e(1+c-k)/L_e$ as L tends to zero. Clearly, B_0 must be the same sign as B_e so that $1 + c > k$.

By evaluating the field at $(0, 0_+)$ just above the current sheet, we find the ratio of inflow to external field strength to be

$$B_i = \left(\frac{(1+c-k)}{(L_e^2/L^2+1)^{\frac{1}{2}}} + k\right) B_e. \tag{4.37}$$

This ratio is important in determining the rate at which the reconnection proceeds. As $L \to 0$ the ratio tends to k, whereas as $L \to L_e$ it tends to $(1+c-k)/\sqrt{2} + k$. First we shall consider the diffusion region which lies along the x-axis between $x = \pm L$.

4.4.3 Diffusion Region Analysis

In the limit when diffusion is neglected in the external region, the diffusion region can be considered as a sheet current. It exists mathematically because there is a cut in the complex plane between $z \pm L$ in the function (4.31). Physically, the field produced by this configuration has a discontinuous B_x

component across the x-axis between $x = -L$ and $x = +L$, so that, although the field is current-free or potential everywhere away from the axis, there is a current given by

$$j(x) = -\frac{1}{\mu}\left[B_x(x)\right]_-^+, \tag{4.38}$$

where $+$ and $-$ indicate points just above and below the x-axis and the brackets denote the difference in the values. As the field below the axis is equal and opposite, the size of the current is simply proportional to twice the size of the field above the axis. When the field is given by (4.25)

$$j(x) = -\frac{2B_0}{\mu L}\left(L^2 - x^2\right)^{\frac{1}{2}} \tag{4.39}$$

with B_0 given by (4.36). This means the current disappears at the ends of the current sheet. By adding the uniform B_x field, there is a jump along the *whole* length of the x-axis in the initial field (4.35). This discontinuity will be removed numerically for $|x| > L$, but remains for $|x| < L$, so the new line current is

$$j(x) = -\frac{2}{\mu}\left[\frac{B_0}{L}\left(L^2 - x^2\right)^{\frac{1}{2}} - B_e k\right]. \tag{4.40}$$

Now neither the current nor the field disappear at the ends of the current sheet.

By considering ideal MHD, just above the current sheet, we see that

$$v_y(x) = \frac{v_e B_e}{B_x(x)}. \tag{4.41}$$

In the original model, the velocity becomes singular as $x \longrightarrow L$, whereas, with the uniform B_x field added, v_y remains finite and $v_y = v_e/k$ at $x = L$.

In reality the sheet has a finite width in which diffusion of the magnetic field can take place and the field slips through the plasma; hence the term diffusion region. If it is assumed that there is a balance between outward diffusion and inward advection, then as the origin is approached

$$v_i = \frac{\eta}{\ell}, \tag{4.42}$$

where v_i is the inflow speed at the diffusion region, ℓ is the width of the diffusion region and η is the diffusivity. Along the remainder of its length the diffusion region width as a function of x is

$$\ell(x) = \frac{\eta}{v_y(x)} = \frac{\eta B_x}{v_e B_e} = \frac{\eta}{v_e B_e}\left[\frac{B_0}{L}\left(L^2 - x^2\right)^{\frac{1}{2}} - B_e k\right]. \tag{4.43}$$

In the Priest-Lee model, the width vanished at L. In contrast, the width remains finite in this model at L where it takes the value $\eta k/v_e$.

In the sheet itself, the flow will be approximately one-dimensional. By considering mass continuity between the mass entering and leaving the diffusion region, the velocity of the plasma in the region, v_x, is given by

$$\ell(x)v_x(x) = \int_0^x v_y(x)\,dx = \int_0^x \frac{v_e B_e}{B_x(x)}\,dx, \tag{4.44}$$

so

$$v_x(x) = \frac{v_e B_e}{\ell(x)} \int_0^x \frac{dx}{B_x(x)}. \tag{4.45}$$

Once again, we find that the singular flow found in the Priest-Lee models is not present here at $x = L$.

4.5 Numerical Solutions

As stated in Section 4.2.1, below the C_+ characteristic coming off the end of the current sheet marks the position of an Alfvénic discontinuity. Above this characteristic, the magnetic field and flow will be preserved, whilst below it the initial field and flow will be used as the initial conditions for the numerical solution. The system solves the MHD equations downstream of the characteristic subject to new outflow boundary conditions. In solving these equations, the discontinuity in the B_x component is removed by applying an altered boundary condition on the x-axis. As the code progresses, the additional boundary condition is removed and the field and flow allowed to adopt a steady state over many Alfvén times.

The shock relations across the discontinuity are those stated in Section 3.5. We are able to impose a new boundary condition on the outflow boundary and choose the one used in Chapter 3, namely a uniform v_x. The numerical scheme solves for the quantities A', Ψ', j' and ω', which are the dimensionless versions of A, Ψ, j and ω and are non-dimensionalised with respect to B_e, v_{Ae} and L_e. On the x-axis there are symmetry conditions for the stream function and vorticity, ω. Also we impose $\partial A/\partial y = 0$ on the x-axis by initially setting the value of the dimensionless flux function, A', to be the same *on* the axis as it is one grid point up from it. Normally, a centred-differencing scheme, such as the one used here, sets the values either side of a grid point to be equal in order for the first derivative of a quantity to be zero at the grid point, but the initial field with the discontinuity has this property inherent across grid points on the x-axis, so the discontinuity will not be removed unless the modified boundary condition is adopted. After some small number of time steps, this altered boundary condition is relaxed and the field evolves with a zero x-component along the x-axis for $x > L$. The outflow boundary condition becomes a linear function of Ψ', the dimensionless stream function. The code allows the quantities to develop in response to the new boundary conditions by adopting time-dependence for the flux function and vorticity. There will be steady states once the time derivatives fall to zero. (In practice the code terminates once the time derivatives are smaller than a certain tolerance level.) The full set of dimensionless MHD equations used is given below with the prime superscripts dispensed with for convenience.

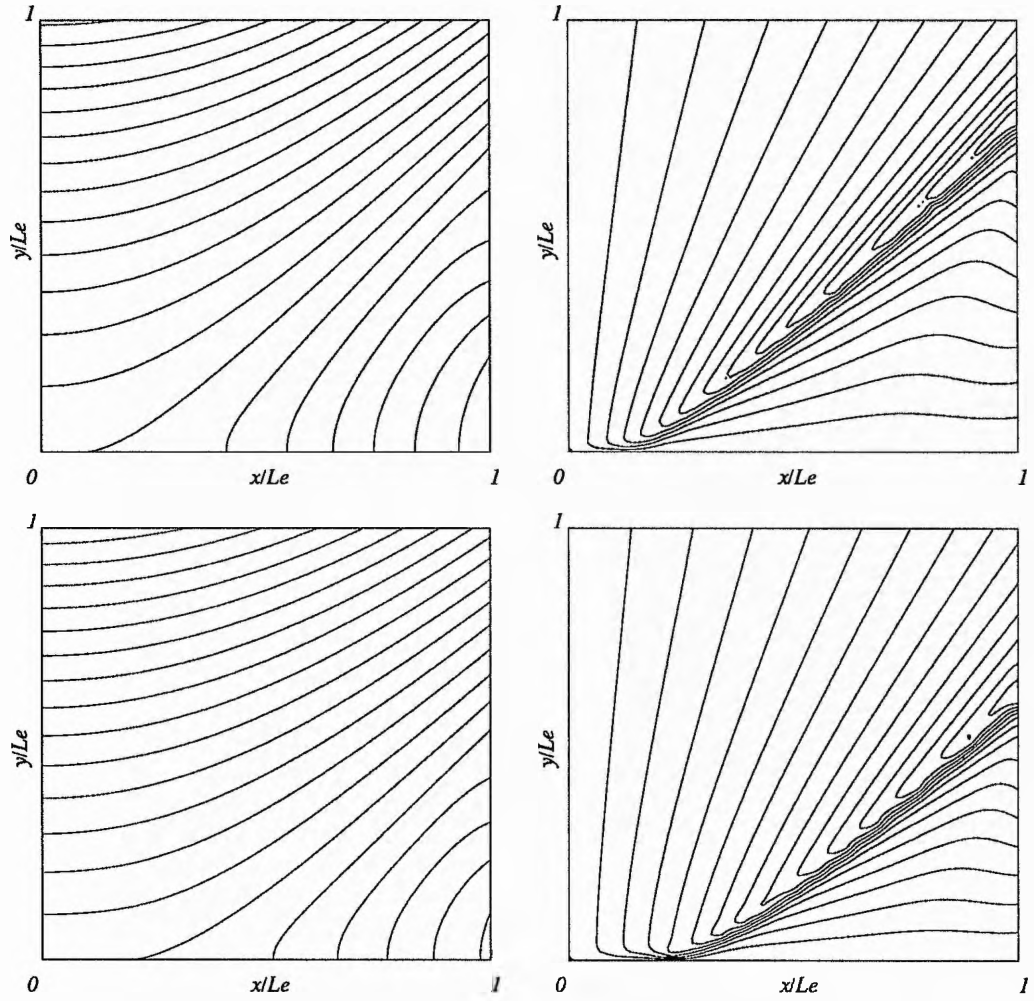

Figure 4.5: Magnetic field lines and streamlines for cusp models when (a) $L = 0.1L_e$ and $k = 0.2$ and (b) $L = 0.2L_e$ and $k = 0.3$.

$$\frac{\partial A}{\partial t} = -\frac{\partial \Psi}{\partial y}\frac{\partial A}{\partial x} + \frac{\partial \Psi}{\partial x}\frac{\partial A}{\partial y} - M_e + R_{me}^{-1}\nabla^2 A \tag{4.47}$$

$$\frac{\partial \omega}{\partial t} = -\frac{\partial \Psi}{\partial y}\frac{\partial \omega}{\partial x} + \frac{\partial \Psi}{\partial x}\frac{\partial \omega}{\partial y} + \frac{\partial A}{\partial y}\frac{\partial j}{\partial x} - \frac{\partial A}{\partial x}\frac{\partial j}{\partial y} + \frac{M_e}{R_e}\nabla^2\omega \tag{4.48}$$

$$\nabla^2\Psi = -\omega \tag{4.49}$$

$$j = -\nabla^2 A \tag{4.50}$$

with the two-dimensional Laplacian operator $\nabla^2 = \partial^2/\partial x^2 + \partial^2/\partial y^2$. These equations form a closed system with (4.49) solving for Ψ away from the outflow boundary using a simple relaxation method. M_e is the external Alfvén Mach number, $R_{me} = v_{Ae}L_e/\tilde{\eta}$ the external magnetic Reynolds number and $R_e = v_e L_e/\tilde{\nu}$ the viscous Reynolds number. The constants μ and ρ are absorbed into the dimensionless variables. The full set of equations is considered so that regions where flow

becomes significant are solved consistently. Indeed, we see analytically from (4.12) and (4.20) that the flow along the axes grows as r^{-1} as the neutral point is approached, so that the flow term in the momentum equation is of the same size as the magnetic terms when $r \approx M_e^{1/2} L_e$.

The imposed boundary condition at the outflow means that the flow is stronger on the x-axis but weaker toward the discontinuity. In the outflow region, the new steady solutions show how the field responds at the boundary; weakening at $(L_e, 0)$ but strengthening further up the outflow boundary. There is also the possibility of a secondary weak shock propagating from the corner on the outflow just below the separatrix where the discontinuity crosses the outflow boundary. This manifests itself as a 'kink' in the flow as the boundary is approached. Nearer the end of the current sheet, the field and flow are less affected. The results of several simulations for non-zero current sheet lengths are shown in Figures 4.5.

4.6 Reconnection Rate and Scaling

In Chapter 3 we saw how the reconnection rate is significantly higher when the effects of an expansive pressure gradient are included in the inflow. In the model presented here the relationships which determine the reconnection rate are crucially altered because the field strength is non-zero as the neutral point is approached even when the diffusion region length falls to zero. The pressure gradients which affected the reconnection rate in the Chapter 3 analysis and can be included in this model will not be considered in the reconnection rate. Rather, the parameter, k, which determines the field strength at the end of the diffusion region will be the sole imposed variable, so we are considering a model which is potential in the inflow region.

The reconnection rate is determined by the relationship between the field strength externally, B_e, and the field strength at the inflow to the current sheet, B_i. By flux conservation, this relationship can be recast in terms of the inflow and external Alfvén Mach numbers, M_i and M_e, as

$$\frac{B_i}{B_e} = \left(\frac{M_e}{M_i}\right)^{\frac{1}{2}}. \tag{4.50}$$

M_e is the rate at which the flux is allowed to be introduced into the inflow region and hence a measure of the overall reconnection rate.

As in the previous analysis, indeed for all steady-state models, we have the Sweet-Parker scalings for the diffusion region length and width, namely

$$\frac{L}{L_e} = \frac{1}{R_{me} M_e^{\frac{1}{2}} M_i^{\frac{3}{2}}} \tag{4.51}$$

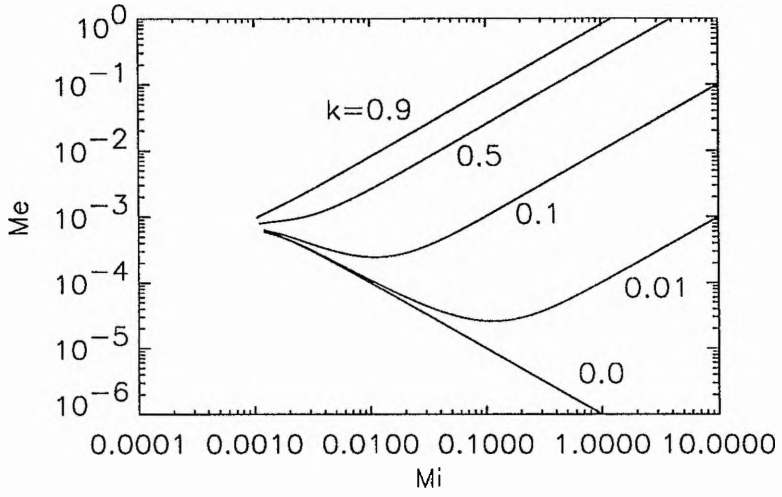

Figure 4.6: The rate of reconnection, M_e as a function of inflow Alfvén Mach number, M_i for different values of parameter k when $R_{me} = 10^6$.

and

$$\frac{\ell}{L_e} = \frac{1}{R_{me} M_e^{\frac{1}{2}} M_i^{\frac{1}{2}}} \tag{4.52}$$

where L_e is the external scale length.

In order to progress we must find $M_i(M_e, R_{me})$ to obtain an overall reconnection rate in terms of R_{me} and k alone. In the potential cusp model, the key relationship between the diffusion region inflow and the external region is given by

$$\frac{B_i}{B_e} = \left(\frac{(1-k)}{(L_e^2/L^2 + 1)^{\frac{1}{2}}} + k \right). \tag{4.53}$$

Using (4.50) and (4.51), B_i and L can be eliminated yielding

$$\frac{M_e}{M_i} = \left(\frac{(1-k)}{(R_{me}^2 M_e M_i^3 + 1)^{\frac{1}{2}}} + k \right)^2, \tag{4.54}$$

which can be rearranged into a quartic in M_e. This is solved numerically, the roots of the quartic providing the relationships between M_i, M_e and R_{me}. Only those roots which yield current sheet lengths satisfying $L < L_e$ are considered. These can be substituted into (4.51) and (4.52) to obtain scaling laws for the length and width of the diffusion region. Relationships between M_e and M_i, ℓ and L are plotted in Figures 4.6 and 4.7.

If $M_i \gg R_{me}^{-1/2}$, the diffusion region length is very short ($L \ll L_e$) and we see that the first term on the right-hand side of (4.53) is not significant compared with the second for most values of k. If

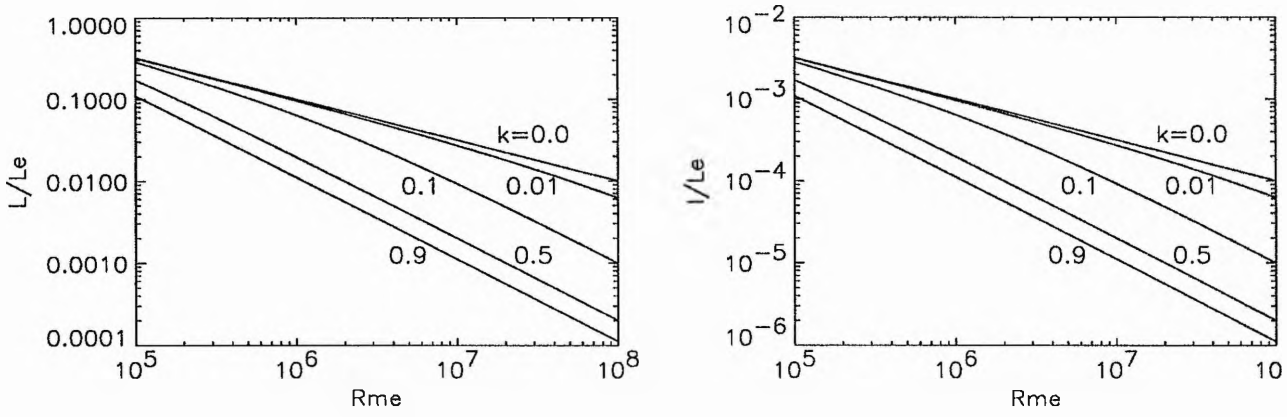

Figure 4.7: The length and width of the diffusion region as a function of the external magnetic Reynolds number $R_{m\epsilon}$ = for different values of k.

we neglect the first term we find the simple relation, from (4.54),

$$M_\epsilon \approx k^2 M_i. \tag{4.55}$$

In other words, as the inflow speed increases, so does the reconnection rate and the current sheet length gets shorter and shorter. Consequently, there is no upper limit on the maximum reconnection rate, $M_e^\star$, and it is independent of $R_{m\epsilon}$. In fact this relationship applies even when $M_i \approx R_{me}^{-1/2}$ if $k > 0.5$, say. This is in total contrast to the normal Petschek relationship. In the previous Y-point analysis the maximum reconnection rate is reached when $L = L_e$ and is proportional to $R_{me}^{-1/2}$.

The resulting scalings for the dimensions of the diffusion region are

$$\frac{L}{L_e} \approx \frac{k^3}{R_{me} M_e^2} \tag{4.56}$$

and

$$\frac{\ell}{L_e} \approx \frac{k}{R_{me} M_e}, \tag{4.57}$$

so that the diffusion region becomes shorter and narrower as the reconnection rate increases.

If k is small, typically less than 0.1, the first term in (4.53) is larger than the second when M_i is small enough and the scaling is close to that for the potential case ($k = 0$), so

$$M_e \approx \frac{(1-k)}{M_i R_{me}}, \tag{4.58}$$

with resultant scalings

$$\frac{L}{L_e} \approx \frac{1}{R_{me}^{\frac{1}{2}} M_e} \tag{4.59}$$

and

$$\frac{\ell}{L_e} \approx \frac{1}{R_{me}^{\frac{1}{2}}}, \tag{4.60}$$

The scaling given by (4.55) still applies once the second term in (4.53) is larger than the first. This occurs once $L < kL_e$. There are no solutions below the $k = 0$ solution because this corresponds to $k < 0$.

If $M_i \ll R_{me}^{-1/2}$, the diffusion region length is very long ($L \gg L_e$) and (4.54) reduces to $M_e \approx M_i$, which is the same as the $k = 0$ solution, but $L > L_e$ is outside the range of the model.

4.7 Conclusions

From the analytical solution involving the double-cusp point it is possible to have a non-singular flow as the separatrix is approached from the inflow region. The flow is also non-singular in the inflow region for the cusp current sheet configuration. This is a significant advance over previous models. The essential difference in the analysis presented here is that the x-component of the field does not vanish at the ends of the current sheet. The singularity in the flow below the separatrix is still present, however. This is due to the vanishing y-component of the field at the end of the current sheet which will always be the case if there is a cusp-like neutral point; however it would be resolved by including a non-zero current sheet thickness.

In the reconnection model new scalings and reconnection rates are found which are unlike previous results. The reconnection rate can be arbitrarily large and is totally independent of the external magnetic Reynolds number. Again, these results are due to the fact that the field strength does not disappear anywhere along the current sheet. In practice, as M_e^* gets close to unity the assumption about incompressibility breaks down so the analysis is no longer valid in this limit.

Chapter 5

Conclusions

In this thesis, the study of magnetic reconnection has been brought together with analysis of magnetic neutral points. We have seen how neutral points can be generalised and observed how the restrictions imposed by seeking magnetic equilibria and steady states determine the behaviour of the magnetic field in the vicinity of neutral points. We have also seen the way in which definitions derived in two-dimensions can be applied to three-dimensional structures.

The nonuniform reconnection models that have been studied have highlighted the crucial rôle played by boundary conditions in determining the rate of reconnection. The models have also been able to help explain features not present in uniform reconnection and reproduced different regimes of reconnection found previously in the Priest-Forbes *Almost-Uniform* model by introducing significant pressure gradients into the inflow region. Following on from the Priest-Lee model, numerical simulations find the current spikes observed by them and show how the field downstream of the shock is affected by the imposition of new boundary conditions. The reconnection rate is found to be greatly enhanced if we allow a highly expansive inflow.

We also see here the strong jets of plasma along the separatrix found in many previous models. The problem of singular flow along the separatrix is addressed in the second reconnection model. The analytical solution about a double-cusp point removes the singularity in the flow as the separatrix is approached from above, a feature which has not been seen before. This means it is not necessary to perform numerical smoothing above the separatrix in the numerical simulations. The non-vanishing field at the end of the current sheet also gives rise to a quite different relationship between the external and inflow fields and consequently a reconnection rate is determined which is independent of the magnetic Reynolds number. This results in a much higher reconnection rate not previously found, with the current sheet shrinking as the reconnection rate increases in contrast to the first model in which the current sheet grew with the reconnection rate. The downstream region is also

solved numerically so that the discontinuous field component along the x-axis is removed.

In future it would be of interest to see if the results produced in this thesis can be reproduced in other models, in particular in full numerical simulations. As yet, a consistent analytical matching between the diffusion region, where the actual reconnection takes place, and the inflow region has not been achieved. This seems a natural extension to the work presented here and elsewhere. Specifically, a consistent way of including the flow along the separatrix so that it is non-singular along the entire separatrix and matches with the inflow might be sought. This thesis stands as a guide toward these goals.

References

Biskamp, D., *Z. Naturforsch,* **37a,** 840 (1982).

Biskamp, D., *Phys. Lett.,* **105A,** 124 (1984).

Biskamp, D., *Phys. Fluids,* **29,** 1520 (1986).

Chapman, W. and Ferraro, V.C.A., *Terrestrial Magnetism and Atmospheric Electricity* **36,** 77 (1931).

Chapman, S and Kendall, P.C., *Proc. Roy. Soc. Lond.* **A 271,** 435 (1963).

Dungey, J.W., *Phil. Mag.* **44,** 727 (1953).

Forbes, T.G., *Astrophys. J.* **305,** 553 (1986).

Forbes, T.G., *Solar Phys.,* **117,** 97 (1988).

Forbes, T.G., *J. Geophys. Res.,* **95,** 11919 (1990).

Forbes, T.G. *et al. Astrophys. J.***356,** 720 (1989).

Forbes, T.G. and Malherbe, J.M., In:*The Lower Atmosphere of Solar Flares* (Ed. D F Neidig), 443 (1986).

Forbes, T.G. and Priest, E.R., *Solar Phys.,* **81,** 303 (1982a).

Forbes, T.G. and Priest, E.R., *Planetary Space Sci.,* **30,** 1183 (1982b).

Forbes, T.G. and Priest, E.R., *Solar Phys.,* **84,** 169 (1983a).

Forbes, T.G. and Priest, E.R., *J. Geophys. Res.,***88,** 863 (1983b).

Forbes, T.G. and Priest, E.R., *Solar Phys.,* **88,** 211 (1983c).

Forbes, T.G. and Priest, E.R., *Solar Phys.,* **94,** 315 (1984a)

Forbes, T.G. and Priest, E.R., In: *Solar Terrestrial Physics: Present and Future* (Ed. D M Butler, K Papadapoulos) **NASA Ref. Pub. 1120,** I.35 (1984b).

Forbes, T.G. and Priest, E.R., *Rev. Geophys.,* **25,** 1583 (1987).

Forbes, T.G. and Speiser, T.W., *J. Plasma Phys.,* **21,** 107 (1979).

Furth, H.P. *et al., Phys. Fluids* **6,** 459 (1963).

Giovanelli, R.G., *Mon. Not. R. Astr. Soc.* **107,** 338 (1947).

Green, R.M., *IAU Symp.,* **22,** 398 (1965).

Imshennik, V.S. and Syrovatsky, S.I., *Sov. Phys. JETP,* **25,** 656 (1967).

Jardine, M. and Priest, E.R., *Geophys. Astrophys. Fluid Dynam.,* **42,** 163 (1988).

Lau, Y-T. and Finn, J.M., *Astrophys. J.* **350,** 672 (1990).

Lee, L.C. and Fu, Z.F., *J. Geophys. Res.,* **91,** 6807 (1986).

Linardatos, D., *J. Fluid Mech.,* **246,** 569 (1993).

Malherbe, J.M. and Priest, E.R., *Astron. Astrophys.* **123,** 80 (1983).

Parker, E.N., *J. Geophys. Res.,* **62,** 509 (1957).

Petschek, H.E., *AAS-NASA Symp. on Phys. of Solar Flares,* **NASA SP-50,** 425 (1964).

Pneuman, G.W. and Kopp, R.A., *Solar Phys.* **18,** 258 (1970).

Priest, E.R., *Solar Magnetohydrodynamics,* D. Reidel Publ. Co., Dortrecht, Holland (1982).

Priest, E.R., *Rev. Prog. Phys.* **48,** 955 (1985).

Priest, E.R. and Cowley, S.W.H., *Plasma Phys.* **14,** 271 (1975).

Priest, E.R. and Forbes, T.G., *J. Geophys. Res.,* **91,** 5579 (1986).

Priest, E.R. and Forbes, T.G., *J. Geophys. Res.,* **97,** 1521 (1992).

Priest, E.R. and Forbes, T.G., *J. Geophys. Res.,* **97,** 16757 (1992).

Priest, E.R. and Lee, L.C., *J. Plasma Phys.,* **44,** 337 (1990).

Priest, E.R. and Raadu, M.A., *Solar Phys.,* **43,** 177 (1975).

Priest, E.R. and Sonnerup, B.U.O., *Geophys. J. R. Astron. Soc.,* **41** 405 (1975).

Scholer, M., *J. Geophys. Res.,* **94,** 5805 (1989).

Sonnerup, B.U.O., *J. Plasma Phys.,* **4,** 161 (1970).

Sonnerup, B.U.O., In:*Solar System Plasma Physics,* Vol III, (Ed. L.T. Lanzerotti, C.F. Kennel, and E.N. Parker), 46, North-Holland, Amsterdam (1979).

Sonnerup, B.U.O. and Priest, E.R., *J. Plasma Phys.,* **14,** 283 (1975).

Soward, A.M. and Priest, E.R., *Philos. Trans. R. Soc. London, Ser.A,* **284,** 369 (1977).

Soward, A.M. and Priest, E.R., *J. Plasma Phys.,* **35,** 333 (1986).

Sturrock, P.A. and Smith, S.M., *Solar Phys.* **5,** 87 (1968).

Sweet, P.A., *IAU Symp.* **6,** 123 (1958).

Syrovatsky, S.I., *Sov. Phys. JETP,* **33,** 933 (1971).

Tur T.J. and Priest, E.R., *Sol. Phys.* **48,** 89 (1976).

Vasyliunas, V.M., *Rev. Geophys. Space Phys.* **13,** 303 (1975).

Vekstein, G.E. and Priest, E.R.,*Astrophys. J.* **384,** 333 (1992).

Vekstein, G.E. and Priest, E.R., (1993) (in press).

Yeh, T., *Astrophys. J.* **207,** 837 (1976).